POLITECNICO
MILANO 1863

SCUOLA DI INGEGNERIA INDUSTRIALE
E DELL'INFORMAZIONE

3D Printable polymer-leather composites for industrial waste recovery and circular economy

Master's thesis in

Materials Engineering and Nanotechnology – Ingegneria dei Materiali e delle Nanotecnologie

Author: **Davide Negri**

Student ID: 995929
Advisor: Marinella Lei
Co-advisor: Luca Guida
Academic Year: 2022-2023

Abstract

Leather is an important material for the field of fashion, with an ever-increasing demand. However, the management of industrial and post-consumer waste is still an environmental issue.

Additive manufacturing (AM) encompasses a range of innovative techniques that enable the versatile processing of a wide variety of materials. This technology facilitates the creation of intricate forms with minimal or restricted manufacturing effort, and it also permits the incorporation of diverse materials within a single object.

The aim of this project is to give leather a second life, through the use of 3d printing.

Two main paths have been identified: the printing of a flexible material and the printing of a rigid material. Leather was evaluated as reinforcing filler, and different formulations were analysed. Composite materials were processed through the Direct Ink Writing (DIW) technology.

Environmental impacts were analysed through Life Cycle Assessment (LCA) to compare a traditional leather industry process and recycled leather process with the help of AM.

Further research is to be done in the future, mainly aimed at identifying specific functions for both materials.

Key-words: leather; additive manufacturing; Direct Ink Writing; Life Cycle Assessment

Abstract in italiano

La pelle è un materiale importante per il settore della moda, con una domanda in costante aumento. Tuttavia, la gestione dei rifiuti industriali e post-consumo è ancora un problema ambientale.

La manifattura additiva (AM) comprende una serie di tecniche innovative che consentono la lavorazione versatile di un'ampia varietà di materiali. Questa tecnologia facilita la creazione di forme intricate con uno sforzo di produzione minimo o limitato, e permette anche l'incorporazione di diversi materiali in un singolo oggetto.

L'obiettivo di questo progetto è dare una seconda vita alla pelle, attraverso l'uso della stampa 3D.

Sono stati individuati due percorsi principali: la stampa di un materiale flessibile e la stampa di un materiale rigido. La pelle è stata valutata come riempitivo di rinforzo e sono state analizzate diverse formulazioni. I materiali compositi sono stati elaborati attraverso la tecnologia Direct Ink Writing (DIW).

L'impatto ambientale è stato analizzato attraverso il Life Cycle Assessment (LCA) per confrontare il processo tradizionale dell'industria della pelle e quello della pelle riciclata con l'aiuto dell'AM.

In futuro saranno condotte ulteriori ricerche, volte soprattutto a identificare funzioni specifiche per entrambi i materiali.

Parole chiave: cuoio; manifattura additiva; Direct Ink Writing; Life Cycle Assessment

Contents

1 Additive Manufacturing

International Organization for Standardization (ISO) / American Society for Testing and Materials (ASTM) 52900:2021 defined additive manufacturing (AM), or more commonly known 3D printing (3DP), as the "process of joining materials to make parts from 3D model data, usually layer upon layer, as opposed to subtractive manufacturing and formative manufacturing methodologies" [1].

The same standard divide AM processes in 7 methods, as in :

- binder jetting;
- directed energy deposition;
- material extrusion;
- material jetting;
- powder bed fusion;
- sheet lamination;
- vat photopolymerization.

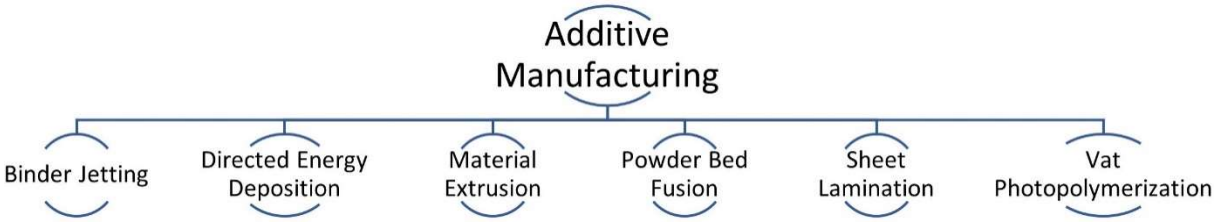

Figure 1: Additive Manufacturing methods.

The general approach of AM, common to all seven methods, involves the progressive addition of material, using different techniques, on a collection platform. The material can be supplied in solid form or in liquid form. A computer-generated path guides the 3D printing of the object, which, layer by layer, comes to completion. The final mechanical characteristics of the object, strongly depend on parameters and printing choices, such as position of the part on the printing plate, percentage and pattern of the fill, number and thickness of the outer perimeters. Different are the capabilities of AM technologies [2]:

- design flexibility, thanks to the layer by layer building that allows the creation of highly complex shapes [3]. AM methods offer design freedom by imposing fewer constraints than subtractive or casting processes. This allows precise

material placement, optimizing structures for efficiency and reduced mass through digital production.

- Cost of geometric complexity: the complexity doesn't come with any extra costs, as it doesn't require additional tools, fixture changes, increased operator skills, or additional time for fabrication. In AM, designers can explore complex shapes without worrying about added expenses, making it a highly attractive option for intricate designs.
- Dimensional accuracy in additive manufacturing (AM) measures how closely the final product aligns with the digital model. While AM initially served prototyping, it now achieves tight tolerances, nearing industrial standards to meet growing demands for finished parts.
- Need for assemblage: Additive Manufacturing enables intricate shapes that would require assembly traditionally. It also allows "single-part assemblies" with integrated mechanisms, printed as one piece with temporary support material. However, post-processing, including support removal, may introduce slight geometric inaccuracies.
- Time and cost efficiency in production run: conventional processes like injection molding excel in time and cost efficiency for mass production [4], despite their high initial setup costs. In contrast, additive manufacturing (AM) processes are slower in fabricating components but shine when it comes to low part quantities because they don't require costly startup tooling [5]. Additive manufacturing's on-demand, localized production minimizes inventory costs and reduces supply chain expenses. It generates minimal material waste, notably in powder bed fusion technologies, leading to a low "buy-to-fly" ratio. When combined with efficient designs, it can be economically advantageous for various applications.

Despite the benefits of AM, the technology is not without drawbacks that need to be investigated and developed. While specific challenges may be more prominent in certain additive manufacturing methods or materials, there are a few challenges that are universal and apply to almost all AM methods. These shared challenges are significant and relevant across the entire spectrum of additive manufacturing techniques.

- Build speed: additive manufacturing remains slower when compared to mass production methods like injection molding. However, this slower pace has been acceptable in many applications, particularly those in customized manufacturing, where the flexibility of AM processes outweighs the speed limitations. [6], [7]
- Mechanical properties and anisotropy: Anisotropic behavior is a significant challenge in additive manufacturing (AM), stemming from the layer-by-layer

printing process, which results in varying material microstructures within layers and at layer boundaries, leading to different mechanical behavior in vertical and horizontal orientations. Anisotropy affects various materials, including metals, ceramics, and polymers, posing challenges but also offering advantages for specialized applications like anisotropic wettability. Research is ongoing to enhance AM product mechanical properties, with a focus on composite materials. [2], [6], [8]

- Resolution: Additive manufacturing faces an inherent trade-off between layer resolution and overall object size. Higher resolution improves surface quality but prolongs printing time [2]. Spatial resolution, influenced by AM method and material, impacts object quality [6]. Layer-by-layer manufacturing creates stair-step surfaces, often requiring post-processing. Each AM method has unique resolution challenges [6], [8].
- Multi-material parts: Incorporating multiple materials within a single printed object is challenging due to various material differences and potential issues like contamination and slow transfer in multi-material AM (MMAM) [6]. Heterogeneous objects can be categorized into two types: distinct material sections in heterogeneous solid models and gradient transitions between materials in functional graded models, offering unique possibilities compared to homogenous parts. [7]
- Surface finish: they are essentials in same cases after printing to address various issues like support removal, refining features and enhancing surface quality. Stair-stepping effect is typical of printed parts due to the layered construction, mainly on curved and inclined surfaces [7]. Various methods are adopted to overcome these problems, as sanding, melting and acetone finishing, causing extra time, money and waste. Support generation is fundamental for prominent parts, increasing the problems just described. Careful support material removal is essential post-printing, ensuring the intended design remains intact and burrs or residue are effectively removed [9].

1.1. History

1980 is remembered as the birth of the 3DP. Hideo Kodama files the first 3DP patent application, describing a photopolymer rapid prototyping system that uses UV light to harden the material; but the idea is never commercialized. Three years later, Charles Hull invents the first stereolithography (SLA) machine, belonging to Vat Photopolymerization. In 1987 the first selective laser sintering was developed by Carl Deckard; and in 1989 Scott and Lisa Crump patented the first fused deposition modelling (FDM), nowadays the most diffused 3D printer in the world. [10]

During the years, 3DP has acquired the interest of many academics and people, thanks to its versatility, cheapness and potentiality. In fact, it is present in several fields, as bio-fabrication [11]–[14], electronics [15]–[18], personal products [19], [20], construction [21], aerospace [22]. After the first commercial instruments were introduced, the number of scientific and technological publications increased year after year, to confirm the immense potential of this process. But only in in recent years we have witnessed to the explosion of the 3DP. We have passed from 3 documents in 2000, to 188 in 2010, to 10864 in 2022 (via Scopus) [23], as shown in Figure 2.

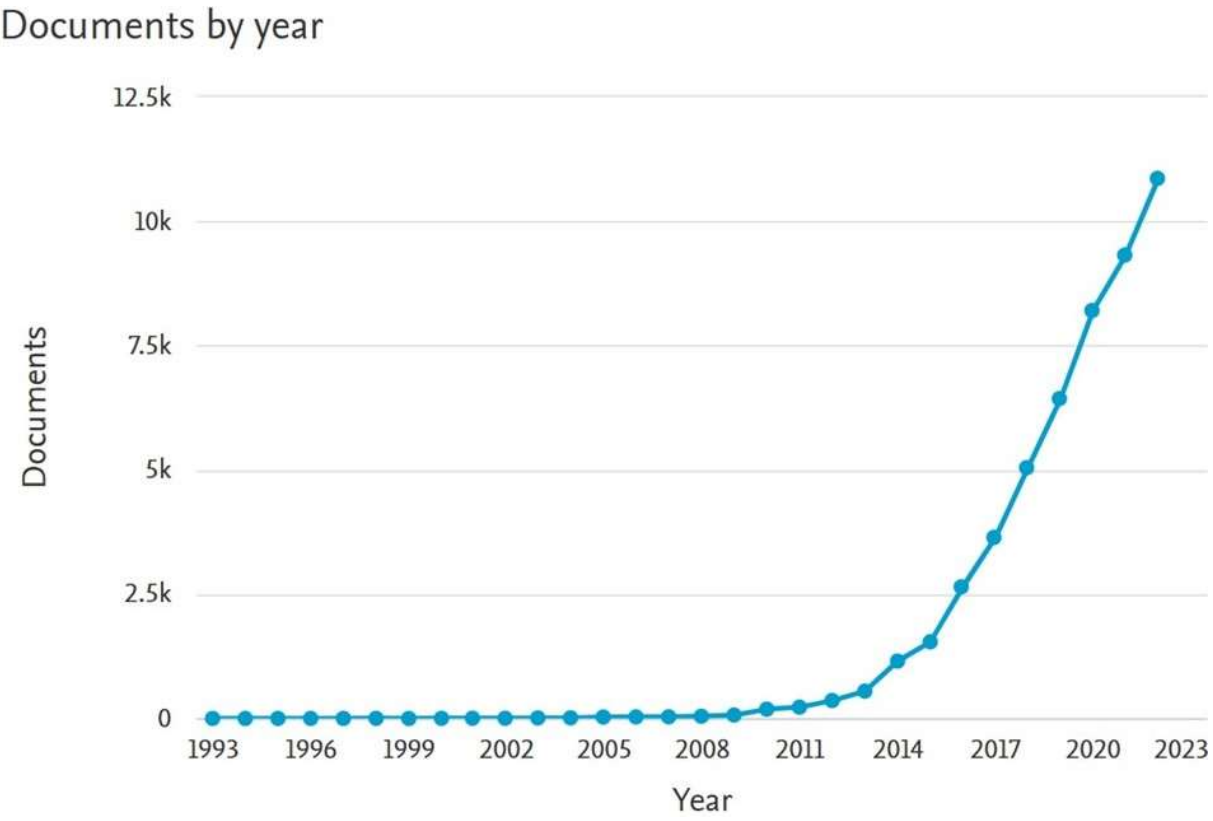

Figure 2: Scientific growth on 3D printing.

It wasn't only a publication impact, but also economic. [6]

1.2. Economic impact

In recent years, the additive manufacturing market has experienced substantial growth, surpassing 5 billion USD worldwide in 2015. This growth attracted major players in the manufacturing industry. AM can produce parts from metals, polymers, and ceramics, with material sales exceeding 900 million USD in 2016. Figure 3 resumes the datas. Interestingly, photopolymers remain the dominant material class, with sales of 350 million USD, primarily used for molding and prototyping. AM metals generated 127 million USD in sales, while polymer powders for laser sintering amounted to 225 million USD. Polymers are the most widely used materials in AM. [6]

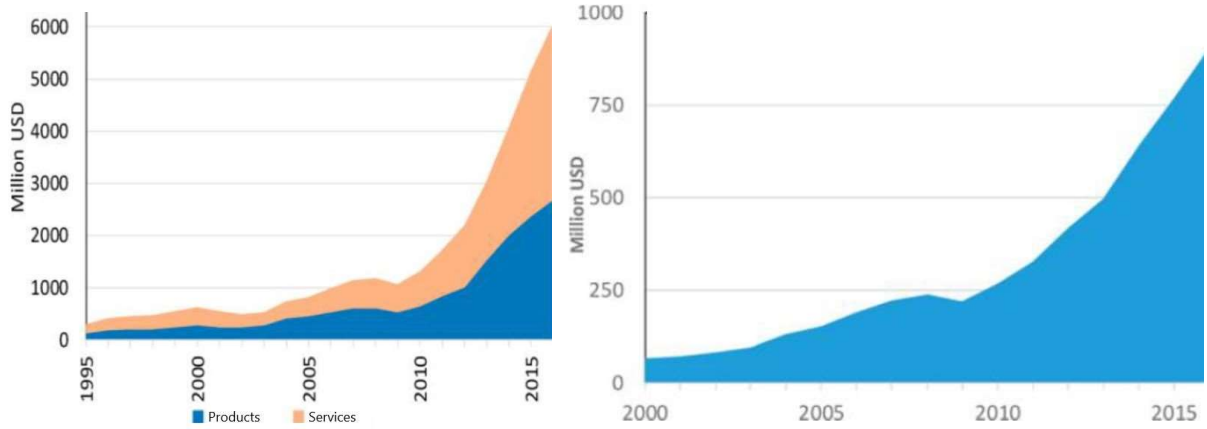

(a) Products and services growth.

(b) Material market growth for 3DP.

Figure 3: Market growth on 3D printing.

1.3. Typical AM Process

All AM products start from a computer drawing and finish with the use of them in some application or more simply as design object. There are different steps to follow [6], [24]:

CAD: it's a software model that describes the geometry of the piece and gives as output a 3D solid representation.

STL conversion: to simplify the geometry of the model and reduce the input data for the machine.

G-code conversion: it's a slicing, that is the process of breaking down a 3D model into a finite number of horizontal layers which can be printed one layer at a time, the STL file and plan the working path. In this step machine parameters are set up too, as the print speed, layer height, volume flow, infill and shell thickness, fill density etc.

Printing: automated step. A monitoring of the machine is recommended to ensure no errors take place.

Removal: when the print is complete, the part is removed from the plate paying attention to avoid machine or object damaging.

Post-processing: optional step. It increases the quality or properties of the piece.

1.4. Classification of AM processes

Based on ASTM Standards, we have 7 classes of processes that differ for printing methods and parameters and materials suitable to be processed. [2], [6], [25], [26]

1.4.1. Binder Jetting (BJ)

In this category, powder particles are joined together due to a liquid bonding agent. All is selectively deposited to fuse powder materials [2], [25]. Same advantages are free of support, design freedom, large build volume [25]. Different materials can be used: metals, ceramics, polymers, sand [2], [25]. A representative scheme is shown in Figure 4.

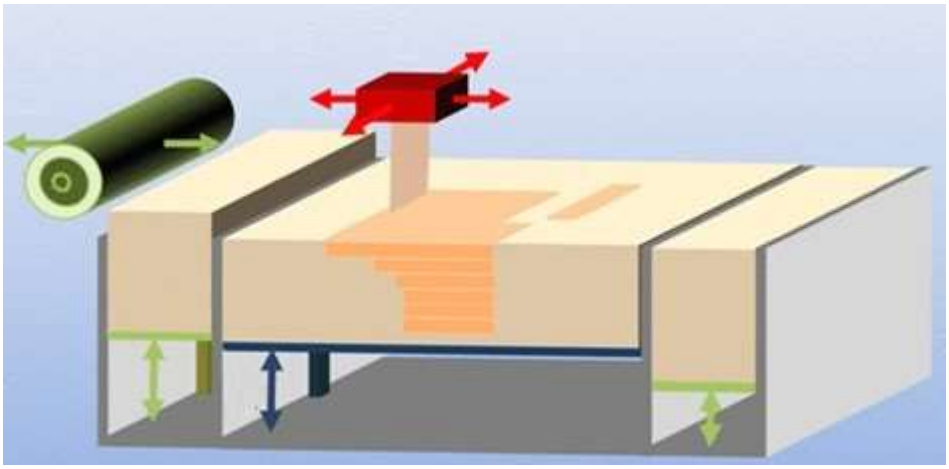

Figure 4: Binder Jetting scheme.

1.4.2. Direct Energy Deposition (DED)

Directed Energy Deposition (DED) employs a metal feedstock. This material is fed through the 3D printer's extruder, where it encounters an intense heat source, such as a laser, electron beam, or plasma. This heat source melts the metal, and the molten material is precisely deposited. Deposition and fusion happen at the same time. The process continues layer by layer, with the baseplate lowering or the extruder raising, after each layer to enable the construction of the next [2], [6], [25]. It's used only with metal particles or wires [2], [6], [25] and is applicable to repair of damaged parts [2]. Figure 5 represents a typical DED setup.

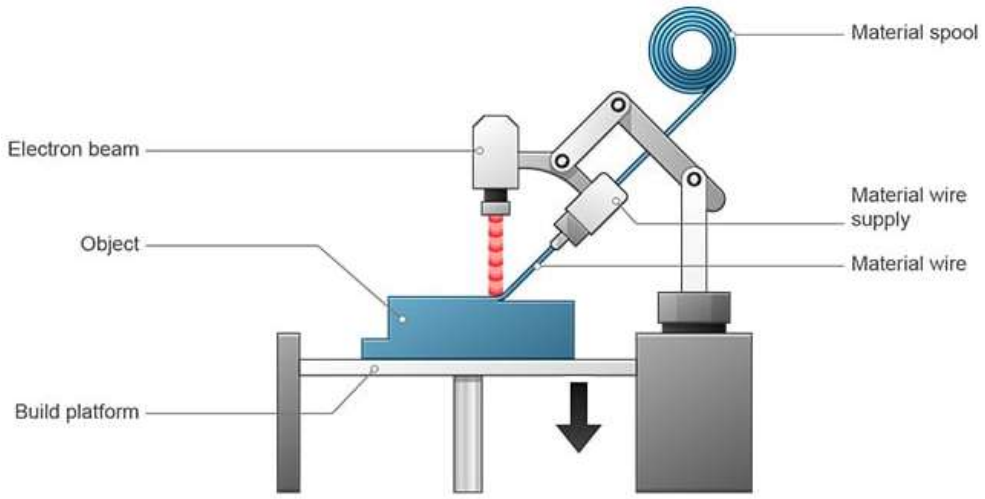

Figure 5: Direct Energy Deposition scheme.

1.4.3. Material Extrusion (ME)

Material is molten and extruded through a nozzle and deposited onto the build platform layer after layer. The molten material hardens when it comes into contact with the substrate and previous layer [2], [6], [25]. Thanks to the inexpensive and flexibility extrusion systems, different methods have been developed [2]. The combination of materials that can be used in this method is enormous: polymers, ceramics, metals, cement, or waste materials, to reduce the environmental impact, and so on; different are also the form of the material like filament, road, slurry or pellet [2], [25]. Material Extrusion scheme is refigured to follow in Figure 6.

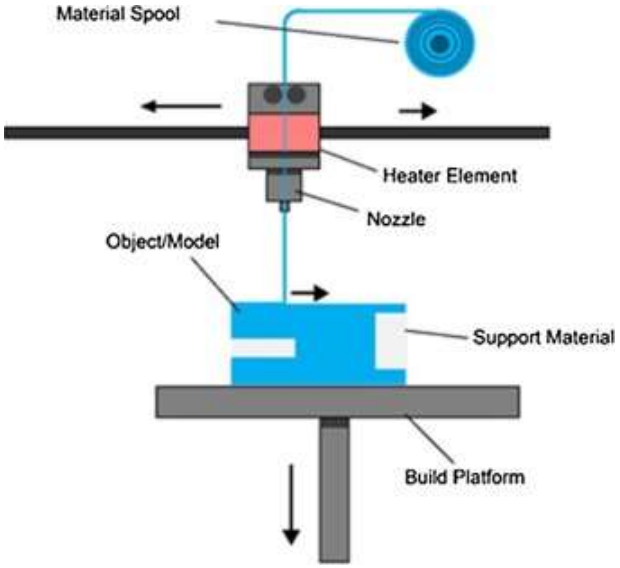

Figure 6: Material Extrusion scheme.

Two technologies, namely Fusion Deposition Modeling (FDM) and Direct Ink Writing (DIW) are the most diffused in this printing method. They will be described in detail. Over time, these technologies have become widely adopted and increasingly accessible to individuals without professional expertise, largely due to the availability of affordable commercial machines.

1.4.3.1. FDM

Fused Deposition Modeling (FDM) is the most diffused 3D printing method that employs a continuous thermoplastic polymer filament to create a material layers. The filament is heated at the nozzle, becoming semi-liquid, and is extruded onto the platform or previous layers, solidifying at room temperature. Key processing parameters affecting mechanical properties are layer thickness, filament width, orientation, and air gap [27]. Mechanical weakness often results from inter-layer distortion [28]. FDM's advantages include cost-effectiveness, speed, and simplicity, yet it's marred by weak mechanical properties, visible layering, and limited thermoplastic material options. Incorporating fiber-reinforced composites enhances mechanical properties but presents challenges like fiber orientation and void formation. FDM's

suitability for polymer composites relies on thermoplastic filaments and is limited by difficulties in reinforcement dispersion and void removal [29], [30].

1.4.3.2. DIW

Direct Ink Writing (DIW) stands out as a highly versatile additive manufacturing technique capable of shaping a wide range of materials as ceramics [31], metals [32], polymers [33] and composites [34]. Formulation of ink material is the key of its success, because it needs to be high viscoelastic before extrusion, effectively shear-thin when passing through narrow nozzles, and regains its viscoelastic properties upon deposition [35]. Adapting functional or composite materials remain challenges for this process, due to difficulties in ink designing with the needed characteristics [36]. In addition, organic solvents or water content in the ink, coupled with low solid contents, can lead to issues as micropores or dimensional changes in printed objects [37][37]. As a result, despite its potential, DIW technology has mostly found use in research labs for small-scale production, limiting its practical application in industry. [38]

1.4.4. Material Jetting (MJ)

It's a selective deposition of liquid droplets from the fluid channel onto the substrate [2], [6], [25]. The phase changing, from the liquid to the solid one, of the jetted droplets is caused by heating or photocuring. The liquid resin is heated to achieve the optimal viscosity for printing, then the printhead travels over the build platform and hundreds of tiny droplets of photopolymer are jetted/deposited to the desired locations. Material is cured by UV light, it solidifies, and the process is repeated for the other layers. In the last years this approach has spread in different fields, from semiconductors [39] to suspensions of ceramics [40]–[42] or metals [43]. The main limitation of this method is the viscosity, that can cause printability issue. It's necessary to have a liquid material with a viscosity compatible with the limited viscosity window of the technique [2]. Figure 7 shows the technology.

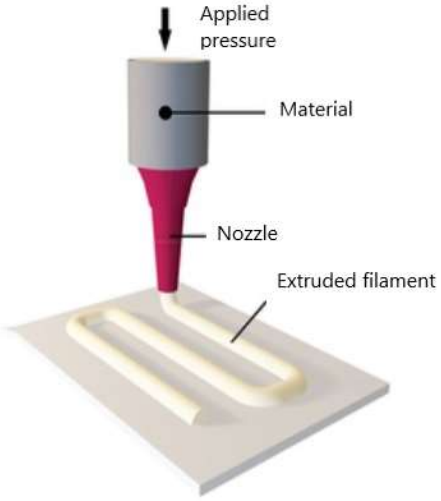

Figure 7: Material Jetting scheme.

1.4.5. Powder Bed Fusion (PBF)

A thermal source, like a laser, is used to selectively induce partial or full melting of the powder particles [2], [6], [25]. A rolling mechanism spreads the new layer of material and, again, there is the fusion [2], [25]. Sometimes there is no melting of the material but sintering, resulting in a porous structure of the resulting product. Sintering is a softening mechanism due to the lower temperature than the fusion one, as the binding mechanism. Metals are the typical materials used in this method [25]. In Figure 8 the mechanism is schematized.

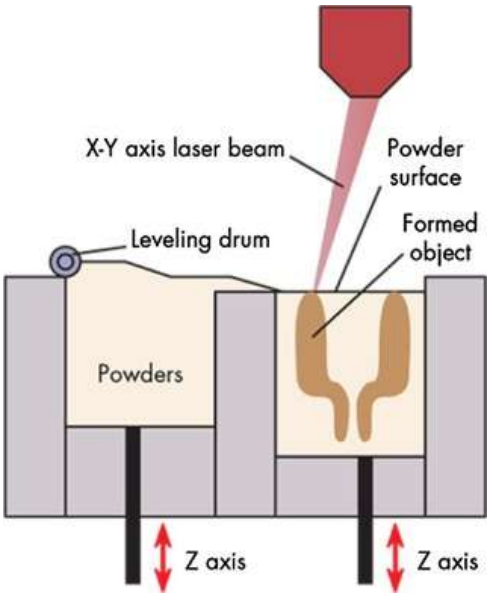

Figure 8: Powder Bed Fusion scheme.

1.4.6. Sheet Lamination (SL)

Material sheets are either cut by laser (laminated object manufacturing LOM) or combined by ultrasounds (ultrasonic additive manufacturing) [25]. LOM consists of superpositioning several layers of material composed of foil to manufacture an object. The operator cut each foil to shape with a knife or laser to fit to the object's cross-section. Advantages are low internal tension and fragility, cheapness, high surface quality [2]. Metal, paper and plastic sheets can be worked with this technique [25]. Figure 9 represents the technology.

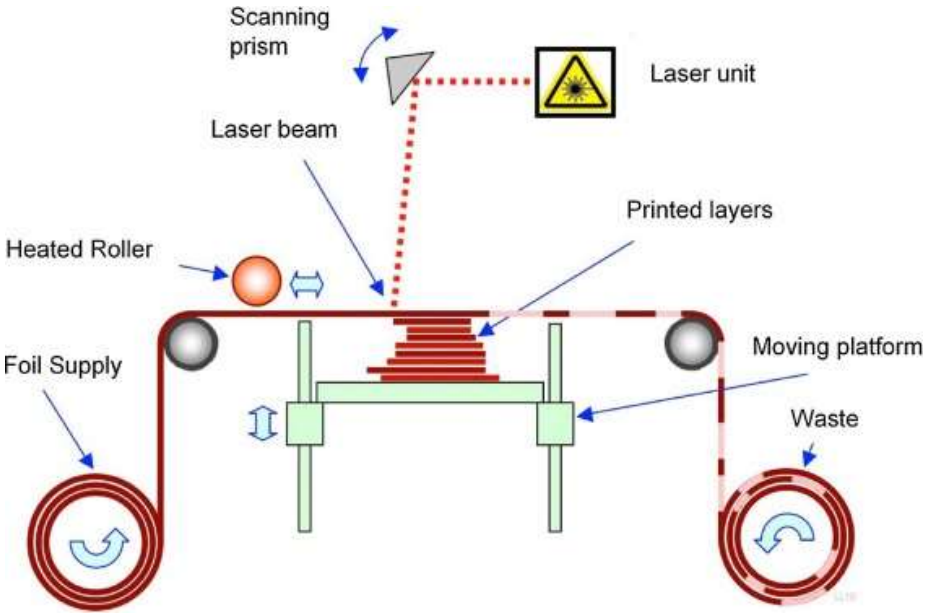

Figure 9: Sheet Lamination scheme.

1.4.7. Vat Photopolymerization (VP)

A liquid photopolymer is selectively cured in a vat by a laser [6]. Photopolymerization is a chemical process of linking small monomers into chain-like polymers [25]. Most of materials used in this system are curable in UV range [2], [25]. Same disadvantages can be processing errors due to overcuring, scanned line shape, high costs [2]. This method is similar to material jetting, which uses lower working temperatures. Only photopolymers are used in this method [2], [25], so a challenge for the future could be the investigation of new materials or combination of them. In the following Figure 10, a scheme of the process is shown.

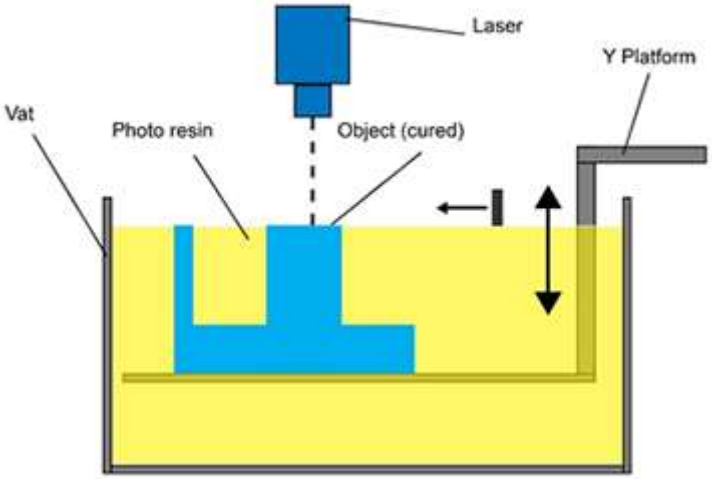

Figure 10: Vat Photopolymerization scheme.

1.5. Materials

1.5.1. Polymers and composites

Thanks to their versatility and easy processability, polymers are the most used 3DP materials [8], [30]. There are two main families of polymers: thermoplastic and thermosetting [44].

As regard the first, in AM, they are found in form of filaments and processed mainly with FDM, where the filament reaches the melting point and can be easily printed onto the platform. PLA and ABS are the most diffused materials in this field; the first is eco-friendly but with low mechanical properties, the second has good properties but with unpleasant odour and styrene release during the print. [8]

Thermosetting polymers are mainly resins that, due to an energetic input like UV or heat, meet curing and become solid. Printing methods for these materials are many, from SLA to DIW or SLS. In this class, properties depend on different parameters as intensity of the light, presence of impurities that degrade chains, presence of additives that help the photopolymerization. [8]

In the last years, to compensate to the low mechanical properties of the printed polymers, the use and study of composite materials has caught on. The introduction of fillers, particles or fibres has different advantages: as just said the increment of mechanical properties [8], [25], [30], the improvement of environmental footprint through the matrix material reduction, or eventually a second life for filler wastes. Nanocomposites represent an interesting subclass thanks their particular properties as very good strength and lightweight, good thermal conductivity, better fire performances, depending on the specific composite that functionalizes the polymer matrix. They offer new opportunities to the 3D industry because they own uncommon characteristic than traditional materials [8].

Challenges for these categories are the investigation of more suitable materials and the development of more specific application for appropriate composites. [8], [30]

1.5.2. Metals and alloys

Metals in AM is a field in continuous expansion. Nowadays, application of interest of these materials are biomedical [45], aerospace [22], automotive [46], research [47].

The process of 3DP of metals is the following powders or wires are melt using a laser or electron beam as energy source and deposited layer by layer forming a solid piece. Powder bed fusion (PBF) and direct energy deposition (DED) are the most used printing technique; direct metal writing, diode-based process, cold spraying, friction stir welding and binder jetting are less diffuse due to and need to be developed. [8]

The most common metals in AM are stainless steel, tool steel, titanium and its alloys, nickel alloys, aluminum alloys, cobalt alloys and magnesium alloys. Al alloys are the most used thank to low cost, high performances and workability.

The challenges for next years are: increase the number of materials, in particular high-entropy alloys, magnetic alloys, high-strength alloys, functionally graded alloys and bulk metallic glasses; develop new printing technologies and improve those already existing. [8]

1.5.3. Ceramics

Ceramics alone are not suitable for 3DP due to the incapacity of powders to fuse together for the high melting points. This is the most important challenge about these materials, so they are mixed with polymers in liquid (resins) or solid (filaments) phase to be able to be printed and sintered. Nowadays, 3DP is able to produce porous or pore-free parts, the second one through the use of a colloidal process, that is the process for consolidating particles with a high density and homogeneous microstructure by controlling the interparticle interaction in a suspension [25]. The capacity to control the porosity is what makes AM interesting for the processing of this class of materials [8].

Stereolithography, inkjet, powder bed fusion and paste extrusion are the most used methods. Due to the probability to have a thermal shock of the piece, from melting point to room temperature, selective laser gelation (SLG) was introduced. It combines sintering and sol-gel technique for ceramic-matrix composites. For ceramics with high melting point, a binder with a low one is used. First of all the binder, activated by a laser, gives a shape, then the green is sintered at higher temperature. But this method doesn't guarantee the same properties as the cast one. The main parameter that affects them is particle size distribution, that impacts on flowability, density and shrinkage of 3D sample. Direct ceramics stereolithography (CSL) adopts a similar printing method where ceramic fillers are dispersed inside a binder and then the green is cured. But in this case the particle size distribution is not predominant factor for the printing. The last technique provides the use of a filament or ceramic paste extruded by a nozzle. In this method the rheology of the material is fundamental. [8]

1.5.4. Biomaterials

At the moment, it's the field of greatest interest. The keyword in this case is "biocompatibility", because we are speaking about materials used for human body (functional tissue and organs). "Bioprinting is a collection of additive manufacturing (AM) technologies, whose aim is to fabricate parts imitating real tissue and organ functionalities by combining both living and non-living materials in a specific three-dimensional (3D) spatial organization structure" [48]. The number of materials in this field is very limited (natural polymers, sodium alginate, chitosan, acrylates-based polymers, hydrogels), and this is the main challenge for researchers. [25]

Hydrogels are a "non-fluid colloidal networks or polymer networks (usually) that are expanded throughout their whole volume by water", as shown in Figure 11 [49]. They are the most used materials as they are rich in water, that is necessary for the living tissues growth.

Biocompatibility and other concerns for medical applications: the use of tomographic images to create patient-specific objects make the AM very promising in personalized medicine field. Surgical planning, prosthetics, dentistry and tissue engineering are the major interested [50]–[55]. The main limitation is the cytotoxicity of same materials as acrylates [56], [57]. PLA instead has a good human compatibility but limited mechanical properties [58]. One of the main goal for the research is the incorporation and growth of living cells, limited by temperature and process control issues. [6]

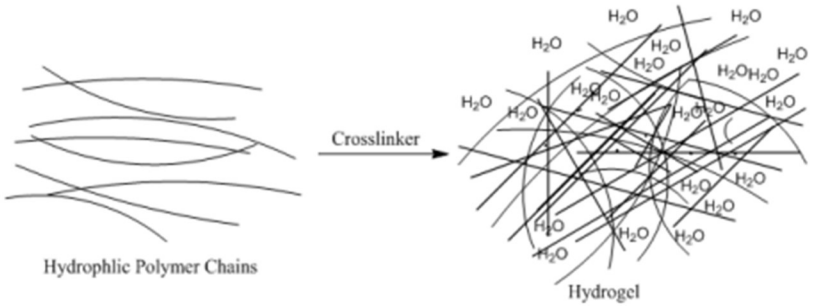

Figure 11: Hydrogel formation by crosslinking process from hydrophilic polymer chains.

Unlike other materials (metals, ceramics, polymers), hydrogels don't require the use of catalysers, solvents or high temperature incompatible with live environments. They can be processed in mild conditions and simulate extracellular matrix.

Fundamentals are the physicochemical properties of the ink, which is the material that must be printed in the DIW method, to have a good printability and guarantee cellular viability. The most important parameters are rheology and crosslinking mechanism. [59]

From a rheological perspective, ideal ink materials for 3D printing should exhibit shear-thinning behavior. As shear rate increases, viscosity decreases due to disruption of fluid interactions or ordering of macromolecules in the flow direction. This relationship is described by a power-law model **Equation 1**:

$$\eta = K\,\dot{\gamma}^{n-1} \qquad \mathbf{1}$$

where η is viscosity, K is the flow consistency index, $\dot{\gamma}$ is shear rate, and n is the power-law parameter. For shear-thinning materials, n ranges from 0 to 1, with 1 indicating Newtonian behavior and values greater than 1 indicating shear-thickening behaviour. Furthermore, the presence of a yield stress, that stabilizes the ink, is fundamental. When the shear stress is above it, the material flows through the nozzle; when it's deposited on the substrate, and so the pressure is removed, the yield stress gives the sufficient stability to the ink to have a defined geometry. Rheology is determined

mainly by the polymer concentration and molecular weight, the higher the better for stability of the printed structure, but cellular life pays the consequences. The same issue is observed in nozzle zone, where the stresses are higher and can induce the cellular death (smaller the nozzle, worse for cells). [60], [61]

A clear behavior representation is shown in Figure 12.

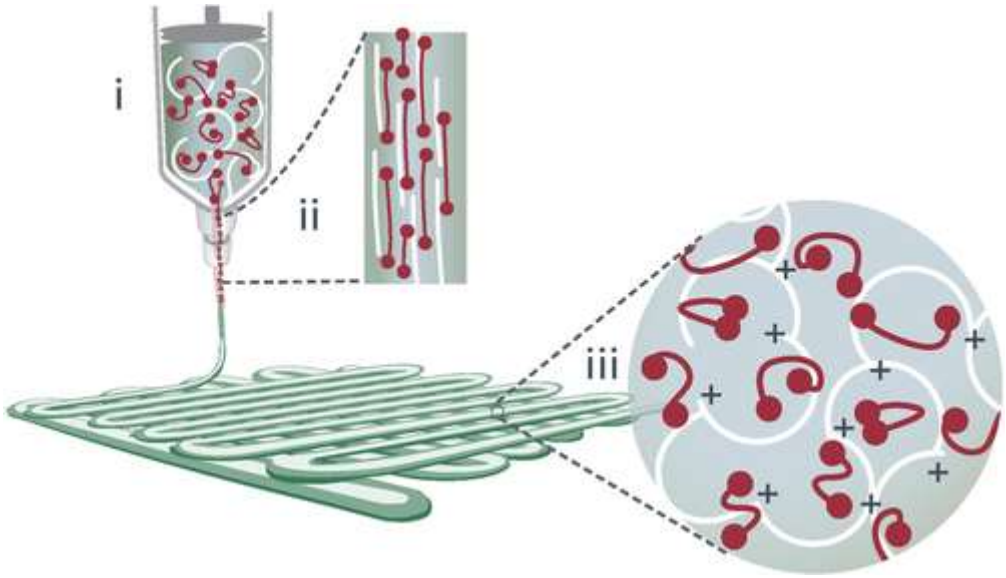

Figure 12: 3D printing reproduction and simulation of ink behavior at different stages.

Solubility parameter, temperature, shear rate and other specific parameters influence on the ink rheology.

Crosslinking mechanisms are divided in physical and chemical processes. The first category is represented by ionic, stereocomplex and thermal mechanisms. They present reversible interactions, constant viscosity during the printing and very good compatibility with biological systems; disadvantages are the necessity of post-processing crosslinking and mechanically weak constructs [59]. As regard the ionic mechanism, it is fundamental in biofabrication, mainly with biopolymers like alginate, a water-soluble polysaccharide. Alginate gels rapidly when comes into contact with di/trivalent cations as Ca^{2+}, making it suitable for cell entrapment in tissue engineering and drug release [62], [63]. Also hydrogels using electrostatic interactions between oppositely charged particles have emerged, forming quickly when mixing and turning fluid with specific shear stress conditions. They have potential in drug delivery and bioprinting applications [64].

Stereocomplex formation regards hydrogels created by coupling a specific oligomer to water-soluble polymers. Hydrogels are crosslinked by stereocomplexes of opposite chirality, with controlled drug or protein release and cell entrapment as potential fields of application. [65]–[67]

For the last class of physical crosslinking, hydrogels change their physical state from liquid, at room temperature for the formulation with bioactive substances or cells, to gel, at body temperature post-administration. [68], [69]

Chemical crosslinking mechanisms exploits the formation of covalent bonds to create hydrogels by linking low molecular weight monomers or polymeric building blocks. These methods can be adjusted for hydrogels with good handling properties and high mechanical strength. Usually, low-viscosity solutions with gel precursors, as monomers or initiators, are mixed, increasing the viscosity through crosslinking until the formation of the 3D polymer network. However, fundamental is the control of crosslinking kinetics. [59]

There are two main groups of hydrogels: natural and synthetic. The most common natural hydrogels are based on biological materials such as alginate, gelatin, collagen, chitosan, fibrin, hyaluronic acid. For synthetic one the most used are poly(ethylene glycol) (PEG) and pluronic. [59]

1.5.5. Concrete

The use of this material in AM was developed in construction industries. The technology exploited is contour crafting. Like inkjet printing, it extrudes the concrete paste at high pressure from a nozzle with attached a trowel-like tool to give a smooth finish. The printability is determined by the fresh concrete properties. To avoid the collapse of the layers, a studied design and suitable equipment are to be used. The introduction of fibers increases mechanical properties of the structure and nanoparticles can improve chemical properties or the behavior when exposed to atmosphere. Another important challenge is the durability of 3D printed structures, due to the rapid evaporation of the water that increases the shrinkage rate and risk of cracking. [8]

New materials are investigated nowadays and in the future due to the increasing complexity and multi-functionality of the products (biomaterials, nanomaterials, smart materials, concrete, metals, ceramics…). Also the necessity to have lasting, high mechanical properties and ecofriendly materials is a main field for the research. Along with materials, 3D printers are an interesting development field, due to same important limitations that afflict them as built speed, anisotropy, resolution, multi-material printing and the need of supports.

2 DIW

Direct Ink Writing (DIW) is a material extrusion technique in which a liquid ink, contained in a cartridge, is extruded through a nozzle onto a substrate, and, via external stimuli as UV light or temperature, crosslinks becoming a solid material. It has established as great potential and versatile 3DP method thanks to the wide range of materials, the low cost of the system, the possibility to print multimaterials [60] (simultaneously or not [70]). Challenges remain in adapting functional or composite materials due to ink design complexities [36]. It was born to create complex ceramic pieces, and only then was investigated in laboratories to exploit in small scale fabrications [2]. The application fields are wide too: soft robotics [71], [72], biomedical implants [73]–[75], stretchable electronics [76]–[78], smart composites [79]–[81], energy storage [82], food printing [83] and so on.

There are three main extrusions, in Figure 13, for the deposition of material: pneumatic, mechanical piston, screw extrusion. The first one is controlled by the air pressure; the second by the motion of the piston and the last by the rotation of the screw [70]. Piston-driven deposition offers more precise control over ink flow than pneumatic one, while screw-based systems excel with high-viscosity materials. However, the latter can generate excessive pressure at the nozzle, potentially harming embedded cells in bioprinting cases. Custom screw designs are necessary. [59]

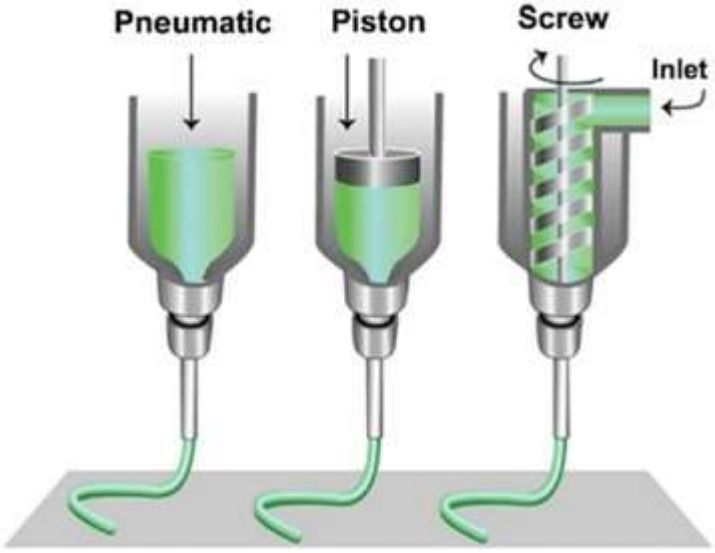

Figure 13: Three main extrusion in DIW technology.

2.1. Ink rheology

To guarantee the adequate printability and to form self-supporting extruded layers, the ink must have a specific rheology. The printer must extrude a continuous filament and the layers' shape must be preserved after the deposition. [60]

From a rheological point of view, shear-thinning behavior at different flow rates is required. This is a non-Newtonian behavior in which the viscosity decreases when shear rate increases [60]; this phenomenon is due to the disruption of interactions inside the fluid or the ordering of macromolecules in the flow direction from an initial disorder state at rest [61]. The viscosity is linked to the shear stress with a power-law model Eq. 1 [60], [61]:

$$\eta = K\,\dot{\gamma}^{n-1} \qquad 1$$

where η, K, $\dot{\gamma}$ and n are respectively the viscosity, the flow consistency index, the shear rate and the power-law parameter. For shear-thinning fluid or pseudoplastic, n is a value between 0 and 1; 1 for Newtonian and greater than 1 for shear-thickening or dilatant [60], [61]. Figure 14 summarizes different material behaviors. A suitable ink for the 3D printing must have a yield stress that guarantees the stability and continuity of the ink flow under pressure [60].

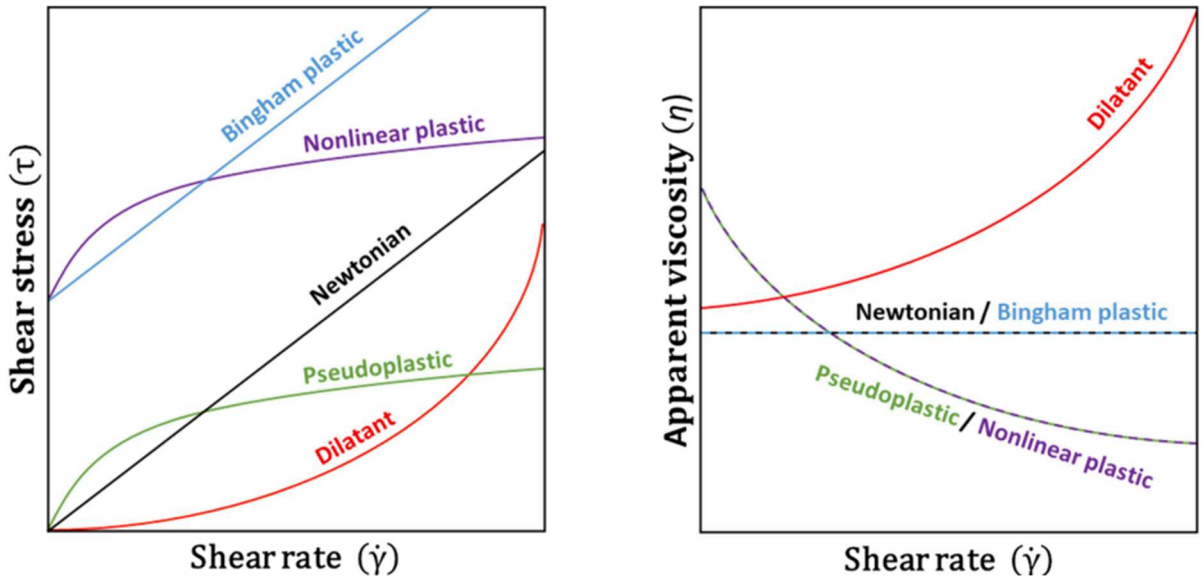

Figure 14: Shear stress and apparent viscosity as a function of shear rate for different material types.

Also materials with a different rheological behavior can be processed, but in this case an immediate solidification upon the exit from the nozzle is necessary. Such solidification can be due, for example, to photopolymerization or gelation [70]. When considering materials with these properties, Herschel-Bulkley model, Eq. 2, is taken into account:

$$\tau = \eta\dot{\gamma} = \tau_y + K\dot{\gamma}^n \qquad 2$$

where τ_y is the yield point of the ink and τ the shear stress [60], [70], [84], [85]. Above the yield point τ_y, the ink starts to flow with a stable and continuous flow. If the shear stress is lower than the yield point, the material shows a solid-like behaviour [70].

As regards the viscosity, it can exhibit a dependence at a constant shear rate with the shearing time and materials, consequently, classified in Newtonian, thixotropic or rheopectic. For the first class of fluids, the viscosity is independent from the shear rate and shearing time. For the second class, when we applied a constant shear stress, viscosity decreases with time due to the progressive breakage of internal attractive interactions. Rheopectic materials show the opposite behavior: increasing the time of application of the shear stress, viscosity increases, caused by the shear-induced microstructural consolidation of the materials. [61]

The rapid transition from shear-thinning to solid-like behavior upon removal of external stimuli is fundamental to give the suitable stability and shape retention to the printed structure [60]. This is linked to the complex modulus G^*, that derives from oscillatory test and gauges a material's resistance to deformation. It splits into two parameters: G' and G'', respectively the storage modulus, derived from $G^* \cdot \cos(\delta)$, where δ the phase angle, that represents the elastic behaviour of the material associated to the elastic stretching of the internal bonds; and the loss modulus, derived from $G^* \cdot \sin(\delta)$, that represents the viscous one associated to the internal friction [61].

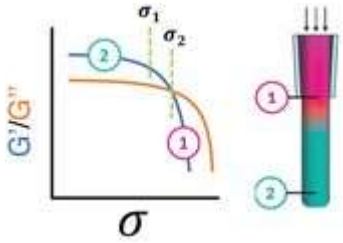

Figure 15: Simulation of ink behavior during extrusion from the nozzle.

Figure 15 is the ideal rheological response of a DIW ink [60]. In region 1, the material has a shear stress above the yielding point, so it yields and can flow through the nozzle and its behavior is liquid-like. In this zone G'' must be higher than G'. On the platform, in region 2, when the stress is removed, the ink becomes a viscoelastic solid. This allows the structure to sustain its own weight and so to carry out the whole printing process. Opposite to the previous situation, G' must be higher than G'' and the ink is solid-like [60], [61], [70], [84]. If G' remain constant over low shear stress, there is a linear viscoelastic region (LVR) [60].

2.2. APPLICATIONS

In recent years, the demand for multi-materials is continuously increasing in additive manufacturing. Originally, AM stood out in producing complex component that required minimal or no post- assembly. As it expanded to functional and complete devices alongside structural parts, the term "complex" extended beyond geometry. Functional components often involve various materials and components. This is noticeable in how additive manufacturing is being applied to different fields as recycling economy, electronic and biomedical.

2.2.1. Recycling economy

Human actions, in particular the continuous growth of fossil-based materials, such as synthetic polymers, have risen to significant environmental concerns. Due to the multimaterials nature of fiber reinforced polymers (FRP), a class of engineering materials, a recycling challenge has been placed. Compared to thermoplastic polymers, FRP have a limit of recyclability [86]. Estimates suggest that the worldwide annual carbon-FRP waste production could potentially reach 20ktons by the year 2025 [87].

Nowadays the end-of-life of composite materials is represented by the linear economy model of “take, make, and dispose”, with their disposal to the landfilling [88]. Due to this unsustainable process, words is moving toward circular economy model, in which various recycling methods have been investigated to recover high-value materials from composites, such as mechanical grinding, pyrolysis, and solvolysis [89]. However, challenges in term of scale-up, maintenance cost, and energy demand affect this circular model [90].

Carbon [91], [92] and glass [91], [93] fibers, because of their excellent mechanical properties, are used in 3D printing with thermosetting polymers to fabricate complex and lightweight composites [94]. Nevertheless, due to their high cost of recycling, they present an important challenge in post-use. Recently, additive manufacturing has emerged as a new frontier with the potential to address the recycling and reprocessing of composite materials. This innovative approach allows the reutilization of recycled FRP through UV-assisted 3D printing with thermosetting polymers, such as epoxy or acrylate resins, demonstrating a promising cost-effective method for recycling and manufacturing high-performance composite components, and contributing to a more sustainable future [91]–[93].

2.2.2. Electronic

In the field of modern electronics, especially in that of flexible electronics, DIW has emerged as a transformative technology with a great potential thanks to its ability to direct deposit electronic modules, including energy storage devices, onto flexible substrate. [95]

Mechanical rigidity, flexibility, and robust adhesion to substrate are essential for printed structures while maintaining high electrical conductivity. DIW is therefore the best choice for the fabrication of wearable and flexible strain [96] and tactile sensors [97]. The ability to create micro and nanoporous structures [98], design flexibility, and the use of conductive nanofillers are features that only DIW can give. Human motion detection and human-machine interface sensors are fields in which DIW technology produced lightweight and portable strain sensors [84].

DIW's simplicity, cost-effectiveness, and digital pattering capabilities position it as a viable alternative to traditional lithographic processes for circuit fabrication, with the use of metallic and conductive nanoparticles, as well as liquid metals, to transmit electrical signals between elements. Planar, 3D or reconfigurable interconnections [99] can be patterned on different substrates, showing the potentiality of DIW technology in circuit design in various fields as solar cells [100], LEDs [99], transistors [76], and antennas [101]. To further highlight its versality in electronic applications, it has been utilized for crafting radiofrequency devices for wireless networks [102] and flexible nanogenerators [103] to power electronic devices and 3D photonic crystals [104].

2.2.3. Biomedicine

DIW has emerged as a versatile technology with a remarkably impact for biomedical and tissue engineering fields. Thanks to its capacity to 3D print a wide range of materials in practically any shape and size, the application in which it has spread also involve the creation of artificial organs and bio-implants [105], [106], microvascular networks [107], scaffold for bone repair and replacement [108], [109], tissue regeneration constructs [110], [111], and advanced biomedical devices [112].

Mechanical robustness, biocompatibility, and seamless integration that DIW brings to printed scaffolds, affirm the magnitude of this technology. DIW-printed hydrogels exhibit considerable mechanical properties and foster cell attachment under physiological conditions, guaranteeing a cell viability over 93% [105]. The possibility of using polymers [113], metals [114], and ceramics [115] to fabricate 3D scaffolds, ensure mechanical properties similar to those of human bones and cartilage with elevated biocompatibility [108].

The precise deposition capabilities, encompassing cells and bioactive compounds are the pivotal feature of DIW technique. This precision unlocks new paths for the development of patient-specific wearable devices, intelligent biomedical implants, health monitoring solutions, and cutting-edge regenerative biomedicine. Thanks to room temperature extrusion, it guarantees the viability of soft materials as biopolymers [116], cells [117], and bacteria [118], rendering them ideal for constructing tissues tailored to patients and specific organs.

In conclusion, DIW offers an innovative and versatile approach in biomedical applications and tissue engineering, with the possibility to create intricate, functional, and biocompatible structures. [60], [70]

3 Life Cycle Assessment

Life Cycle Assessment (LCA) is a comprehensive method for evaluating the environmental impacts of products throughout their entire life cycle. It takes into account not only the emissions but also the depleted resources. Key guidelines and frameworks for LCA include ISO 14040 and 14044, along with resources like the International Reference Life Cycle Data System (ILCD) Handbook [119] from the Joint Research Center (JRC), which aids LCA practitioners in their decision-making.

LCA assesses a wide range of products, encompassing both goods and services. A full life cycle assessment considers every step from resource extraction to the product's End of Life (EoL). However, LCA studies can also focus on specific phases. For example, "cradle to gate" studies focus on a product from the extraction (the cradle) to its exit from the factory (the gate), where manufacturing occurs. When the analysis extends to End of Life management, talk about "cradle to grave". Conversely, other studies are focused on the End of Life stage, which can be viewed as a "gate to cradle" analysis, where materials enter the system as post-consumer waste requiring treatment. "Cradle to cradle" is the last approach based on the circular economy idea.

In the realm of LCA, the term "system" or "product system", denotes a collection of activities and processes chosen for modelling because they represent crucial stages in the product's life cycle. Each of these activities, characterized by inputs and outputs, is known as a "unit process", and they exchange matter and/or energy through "flows", which in turn can be categorized as "product flows" when exchanges occur within the system or with the broader technosphere, encompassing all human activities outside the modelled system. Alternatively, "elementary flows" describe exchanges strictly with the environmental emission. "Waste flows" is another category, that need to be connected with waste management until processes.

There are four main staps within LCA structure [119], [120]:

- Goal and Scope definition

  The Goal should explain six main aspects according to the ILCD Handbook:

  1. *Intended Application*: a study having the objective of guiding decisions by conducting an information comparison;
  2. *Limitations connected with the study* from selected assumptions and techniques;

3. *Reason for carrying out the study and the Decision Context*;
4. *Target Audience*;
5. Whether the *study is meant to be disclosed with public*;
6. *Commissioner of the study* and other actors (if present).

In the process of defining the Scope, the system to be modeled is explored in greater depth. It is necessary to establish the Functional Unit, which is a way to measure the function of the system produced by answering questions such as: *what? how much? how well? for how long?*. When making comparisons between systems, it is essential that each has the same functional unit (ideal to answer the questions in the same way). The Reference Flow is the flow within the system that implements the functional unit and against which all other inputs/outputs of the system will be evaluated. Systems usually have multiple functions, which means that they can perform more than one main function, while the others are referred to as "co-products." As explained in the ILCD Handbook, when defining Goal and Scope, it is critical to define the "decision context." This determines the main methodologies to be used during the development of life cycle inventories. In particular, it determines whether the study will refer to an attributional or consequential approach and whether it will adopt allocation or substitution to address multifunctional systems. In conclusion, specific boundaries separate the various systems from the rest of the technosphere, the selection of which requires justification, as the burdens of all external activities are excluded from the subsequent steps. in addition, some system activities can be excluded based on the "cut-off criteria," which identifies a predetermined threshold in terms of relative environmental impacts, below which a process can be considered negligible. Moreover, already in the definition of the Scope, it is necessary to include the methods to be applied in both the LCIA phase (described below) and the interpretation phase.

- Life Cycle Inventory (LCI)

  This step refers to the collection of data and the concrete creation of the model, including the definition of all unit processes along with their input and output flows, which include both product and elemental flows, building the inventory. the previous step defines how all these operations are to be performed. Data are collected for two aspects: for the foreground system, where it is necessary to obtain a data set that is as representative as possible of the specific life cycle activities being modeled; for the background system, where databases are relied upon for data collection (such as EcoInvent).

- Life Cycle Impact Assessment (LCIA)

  Once the inventory has been created, all elementary inputs/outputs, with their own units of measurement, must be linked to environmental impacts in the

LCIA phase. To do this, Impact Assessment Methods, developed after extensive experimentation, are entrusted to LCA practitioners. In the classification stage, each elemental stream is analysed to identify which environmental issues it might contribute to. The various issues affecting human health and/or ecosystems are divided into Impact Categories. The categories evaluated can vary among the different methods available and, more importantly, can be evaluated through different Characterization Factors. The latter concept refers to the characterization phase within the LCIA, in which each flow inventory is converted into a contribution to the outcome of an impact category, as measured by a single Impact Category Indicator (essentially a unit of measurement that can quantify a given environmental problem). This conversion, in fact, is done through characterization factors. It is also important to note that impact categories can belong to two types: intermediate or endpoints. Endpoint impact categories aim to directly measure natural environmental, human health or resource impacts by identifying the main problem of interest. On the other hand, midpoint impact categories measure the intermediate variables of the environmental process between the LCI results and the category endpoints. Finally, an optional procedure during the LCIA phase is normalization, which seeks to recalculate an indicator result based on reference data, such as annual emissions per capita. the goal is to obtain an expression of impact in terms of People Equivalent (PE), for greater understanding and comparability of results.

- Interpretation phase

  The final stage of the LCA procedure, in which the results obtained from the previous stages are summarized, interpreted and discussed and then conclusions and recommendations are drawn. Several steps must also be followed in this final stage:

  - Completeness check

    The inventory is checked to determine the degree of completeness and whether the exclusion criteria defined in the scope have been met. The impact assessment carried out must also be checked in the same way.

  - Consistency check

    The choices and assumptions made during the study are checked. In particular, it is important to ensure that they are representative of the defined purpose and scope.

  - Sensitivity Check

    It is the most important stage in which the robustness of the study is assessed and recommendations are made. First, an order of importance (influence on outcomes) and quality (reliability of the source) must be

assigned to the data. A Perturbation Analysis quantifies importance, in which Sensitivity Ratios (SRs) are assigned to parameters. SRs represent the ratio of the change caused in an impact category outcome to the change in the selected parameter responsible for that change Eq. 3:

$$SR = \frac{\Delta Impact\ Category\ Result}{\Delta Parameter} \quad 3$$

A Scenario Analysis can also be performed, which consists of varying certain assumptions and modeling choices to test the robustness of the results. Finally, through an Uncertainty Analysis, probability distributions can be defined for key model parameters and the effect of these uncertainties on the study conclusions can be evaluated through a Monte Carlo analysis.

- Identification of significant issues

  This last step involves analysing the contribution in order to identify which major life cycle processes most affect the final results. it is also essential to compare the results obtained with the literature for consistency.

- Conclusions

  The conclusions should be iterative and assess whether the objectives and the scope of the study have obtained answers. It is important to re-emphasize the study's limitations. Any future recommendations should be cautious and disclosed along with the time frame to which they apply.

The main impact categories considered in the project, and their indicators, are briefly explained below [121]:

- Climate change

  The chosen parameter for characterizing the midpoint in relation to climate change is the Global Warming Potential (GWP). This metric measures the cumulative rise in infrared radiative forcing caused by a greenhouse gas (GHG) and is expressed in kilograms of carbon dioxide equivalents (kg CO2-eq).

- Ozone depletion potential

  Ozone-depleting potential (ODP) is denoted in kilograms of chlorofluorocarbon-11 (CFC-11) equivalents. ODPs represent the cumulative reduction in stratospheric ozone concentration over an infinite time horizon.

- Human toxicity

  The midpoint characterization factor for human toxicity is expressed in kilograms of 1,4-dichlorobenzene-equivalents (1,4DCB-eq). Separate human-

toxicological effect factors were derived for carcinogenic and non-carcinogenic effects, reflecting lifetime disease incidence variations due to substance intake.

- Particulate matter formation

  In assessing the midpoint characterization factors for the formation of fine particulate matter, the focus was on the human population's intake of $PM_{2.5}$. These factors, termed particulate matter formation potentials (PMFP), are quantified in kilograms of primary $PM_{2.5}$-equivalents. Predictions of the alteration in ambient $PM_{2.5}$ concentration subsequent to the release of precursors (NH_3, NO_x, SO_2, and primary $PM_{2.5}$) were made using emission-concentration sensitivity matrices.

- Ionizing radiation

  The point at which the characterization factor at the midpoint level was determined is where the combined dose arising from the release of a radionuclide is assessed. The midpoint characterization factor, known as ionizing radiation potential (IRP), is expressed in terms of Cobalt-60 equivalents (kBq U235 eq) concerning air.

- Acidification

  In determining the midpoint characterization factors for acidifying emissions, the study considered the fate of pollutants in both the atmosphere and the soil. Acidification potentials (AP) were quantified in kilograms of sulfur dioxide (SO_2)-equivalents. It quantifies the changes in acid deposition resulting from alterations in air emissions of nitrogen oxides (NO_x), ammonia (NH_3), and sulfur dioxide (SO_2).

- Freshwater eutrophication

  These factors, known as freshwater eutrophication potentials (FEP), are quantified in kilograms of phosphorus (P) to freshwater-equivalents. Regarding emissions to agricultural soils, it was assumed that approximately 10% of all phosphorus is typically transported from agricultural soil to surface waters.

- Marine eutrophication

  Kg 1,4-dichlorobenzene-equivalents (1,4DCB-eq) is the characterisation factor. Regard the emissions to marine zones.

- Freshwater ecotoxicity

  Kg 1,4-dichlorobenzene-equivalents (1,4DCB-eq) is the characterisation factor.

- Land use

  The midpoint characterization factors, expressed in square meters per year of annual crop equivalents ($m^2 \cdot yr$ annual crop equivalents), denote the proportional impact on species loss associated with particular land use types.

These land use types include annual crops, permanent crops, mosaic agriculture, forestry, urban land, and pasture.

- Water resource depletion

  The midpoint characterization factor represents the ratio of water consumed to water extracted, measured in cubic meters (m^3) per cubic meter of water extracted.

4 Circular economy

The concept of the circular economy (CE) was initially introduced by Pearce and Turner in 1990 [122]. It envisions an economy where waste is transformed into resources through either technological or natural feedback mechanisms, ensuring that the stock of resources remains constant or increases over time. More recent definitions emphasize achieving this by maximizing the utility and value of products, components, and materials, reducing waste and pollution, and regenerating natural systems. CE strategies aim to move away from the linear "take-make-dispose" model and focus on preserving natural, manufactured, human, and social assets. While economic prosperity is often highlighted as the primary objective of CE, its positive impact on environmental quality is also significant [123].

LCA's methodological advancements enable the analysis of product systems and their interactions through an interdisciplinary approach [124]. For instance, guidelines such as the Guidelines on Social LCA (S-LCA) and the concept of Life Cycle Sustainability Assessment (LCSA) broaden the scope of assessment to include social and economic impacts. LCSA evaluates all negative and positive environmental, social, and economic impacts throughout a product's life cycle. LCA and LCSA are highly valuable tools for assessing CE strategies. They help in evaluating and comparing different CE options and their environmental performance, supporting the transition toward more sustainable consumption and production patterns. Additionally, the shift to a circular economy can affect international trade and lead to structural changes in the economy, impacting primary and secondary resource trade flows. [125]

In summary, LCA and LCSA offer systematic approaches to integrate the impacts of primary resources and value chain components into CE analyses. They allow us to assess whether the environmental benefits of CE strategies can be realized and identify critical processes and aspects that require effective management.

The provided text discusses various strategies for achieving Circular Economy (CE) goals, which aim to reduce waste, promote sustainability, and optimize resource utilization. These strategies include reducing waste, using renewable energies, reuse, remanufacturing, recycling, product waste energy recovery, disposal, and transforming waste into energy. Each strategy is briefly described, and some sub-strategies related to these approaches are highlighted.

Design for reducing wastes is a crucial aspect of sustainable product development, focusing on minimizing waste throughout a product's life cycle. Several methods

contribute to this strategy, including structural optimization, fluid dynamic optimization, and dematerialization. Structural optimization involves reducing mass through rearrangement, fluid dynamic optimization aims to decrease fluid usage, and dematerialization eliminates unnecessary components.

Design for using renewable energies emphasizes incorporating renewable energy sources to enhance product functionality. This involves identifying suitable sources compatible with operational requirements, such as solar energy, and considering factors like hourly sunlight availability.

Design for reuse is rooted in Circular Economy principles, encouraging prolonged product use. Structural improvement, adaptability, and on-site reuse are key considerations, promoting durability and flexibility in product design.

Design for remanufacturing involves refurbishing products after initial use, promoting sustainability through resource efficiency and technology selection. This strategy aligns with Circular Economy goals by extending the life of products.

Design for recycling identifies and incorporates recyclable materials into products, focusing on facilitating recycling and disassembly operations. Two modalities include ecosystem restoration, contributing to environmental regeneration, and technical recycling, reproducing constituent materials for reuse.

Design for energy recovery aims to reduce wasted energy by introducing dedicated devices for recovery within or outside the product. Examples include heat exchangers and Kinetic Energy Recovery Systems, contributing to more efficient energy use.

Design for disposal using biodegradable materials focuses on reducing environmental impacts associated with disposal. This involves strategies like reducing material quantity and incorporating biodegradable materials, such as bio-based polymers, to facilitate environmentally friendly disposal.

Design for recovering energy from waste maximizes energy recovery during product decomposition, minimizing pollutant emissions. This strategy involves analyzing product characteristics to select appropriate disposal technologies and modifying product structures to enhance disassembly for improved energy recovery.

In summary, these design strategies align with Circular Economy principles, emphasizing reuse, recycling, energy recovery, and responsible disposal. Implementing these strategies supports sustainable practices, contributing to resource conservation and reduced environmental impact throughout the entire product life cycle. Businesses and industries adopting these approaches can play a vital role in promoting environmental sustainability. [126]

5 Leather

5.1. History

The origin of leather, a remarkable and innovative material, is attributed to the ancient practices of early humans striving for survival. In Paleolithic period primates relied on hunting for sustenance. Neolithic era marked a shift from hunting to animal husbandry for food production. During this time, leather made its first appearance with the production of clothing, footwear, and rudimentary shelters from animal skins and hides, ensuring no part of the animal went to waste.

The ancient human noticed that raw animal hides putrefied when exposed to moisture but became stiff and coarse when dried. This posed difficulties in utilizing them for creating comfortable clothing. To overcome this, they tested different methods as soften the fur and make the skins more pliable. To prolong the durability of hides, they applied greasy substances. Technique such as brain tanning and smoking the treated hides over wood fires were developed to improve and preserve hides flexibility.

Tanning concept, that is essential in the leather production, has developed over time. Bark and leaf infusions from plants like mimosa and chestnut were the first treatments adopted. Alum-based tanning, known as “aluta”, and the use of chromium salts came into practice at later stages. [127]

This knowledge was closely guarded and passed down through generations. Leatherworking skills have made great strides forward in civilizations as Egypt, China, Babylon, and India. In Europe, leather crafting expanded during Greek and Roman periods, with techniques involving gall nuts, bark, and sumac. After the decline of the Roman Empire, the art of tanning diminished in Europe. Moors, in Spain, reintroduced it, leading to the resurgence of artistic leatherwork, in particular Cordovan leather [127]. Scenes of people dressing tiger skins have been found by archaeologists in a 4000-years-old stone carving in Berlin [128].

5.2. Economy

Leather is a highly refined manifestation of animal hides and skins. It represents an important example of circularity since it derives from waste from food chain. Despite

the prevalence of modern materials, such as plastic, metals, and synthetics, leather continues to make room thanks to its great quality and aesthetic appeal. Leather and leather-based products are among the most traded commodities worldwide. The international trade reached annual values exceeding 80 billion USD [127]. In 2019, global import and export statistics for raw hides, skins, and leather were respectively valued at 20,351,371 and 19,535,920 thousand USD [129]. In 2022, the worldwide market for leather products was assessed at USD 440.64 billion in term of size, with Europe occupying USD 166.22 billion. Projections suggest that leather market will expand from $468.49 billion in 2023 to reach $738.61 billion in 2030, as shown in Figure 16. [130]

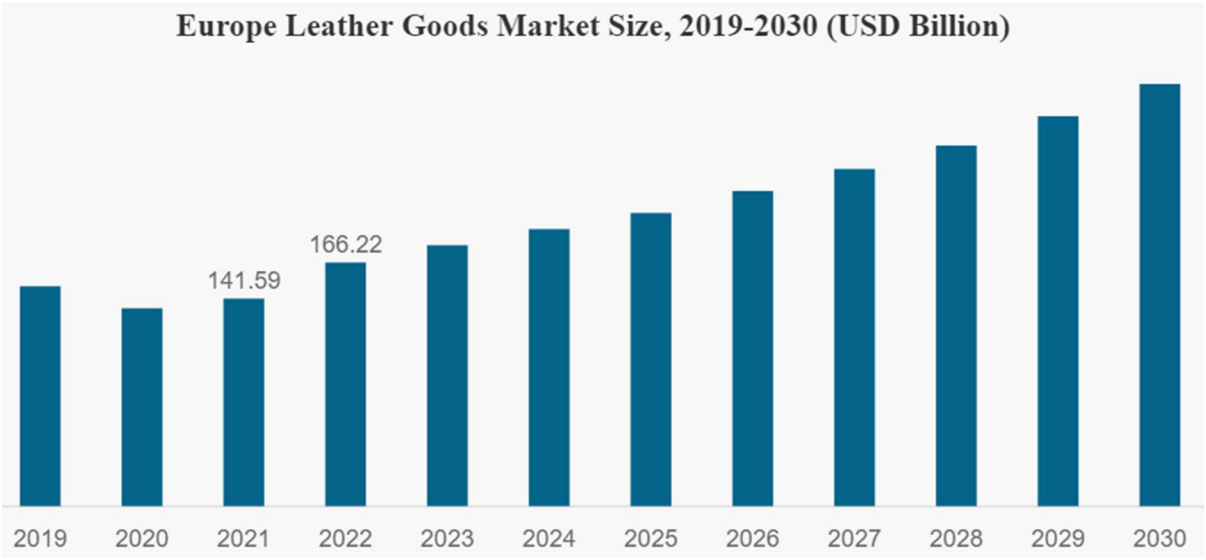

Figure 16: Growth of the European leather market expected in the coming years.

The worldwide production capability is roughly 15 Mt of leather annually [131]. During the processing of leather, numerous wastes are produced. It is estimated that for each Mt of processed leather, the wastes are: 4.3-6.5 kg of split and offcuts; 100 kg of shavings; 2-6 kg of leather dust; 50 kg of fleshing waste; 3.5 kg of hair and birse [132].

5.3. Composition

Leather is a natural material derived from animal skins. Even after the tanning process, the leather retains its distinctive multi-layered structure. Usually the leather production uses cattle hides, pigskins, goatskins, and sheepskins as raw material, but, rarely, fish and reptile skins are used too.

Three different layers compose the skin, Figure 17 [133]:

- Epidermis: it represents the outermost thin layer composed mainly by keratin. The primary function is the protection. Its thickness depends on the animal hair coat development, with a range between 1%, in densely-haired animals, and 5%, in sparsely-haired animals. Typically, the epidermis layer is removed for the leather production.
- The whole corium: it represents the bulk of the skin and strongly influences the final characteristic of the processed leather. It can be further divided into two structures: grain layer and corium major layer. The first is a thin layer composed by non-collagenous substances, like fat cells, sebaceous glands, sweat glands, elastin fibers, muscle tissue, and hair follicles, that are partially or completely removed during the production. Corium layer is also composed by collagen fibers, and differs from the grain one in thickness and collagen fiber interweaving, with the latter thinner and denser [134]. The proportion of the grain layer can differ significantly, mainly depending on age and species. This natural variation in the grain layer proportion contributes to the uniqueness of the qualities and characteristics of different types of animal skins [135]. The final result of the leather is a material mainly composed of tightly interwoven collagen I fibers and fiber bundles in a network.

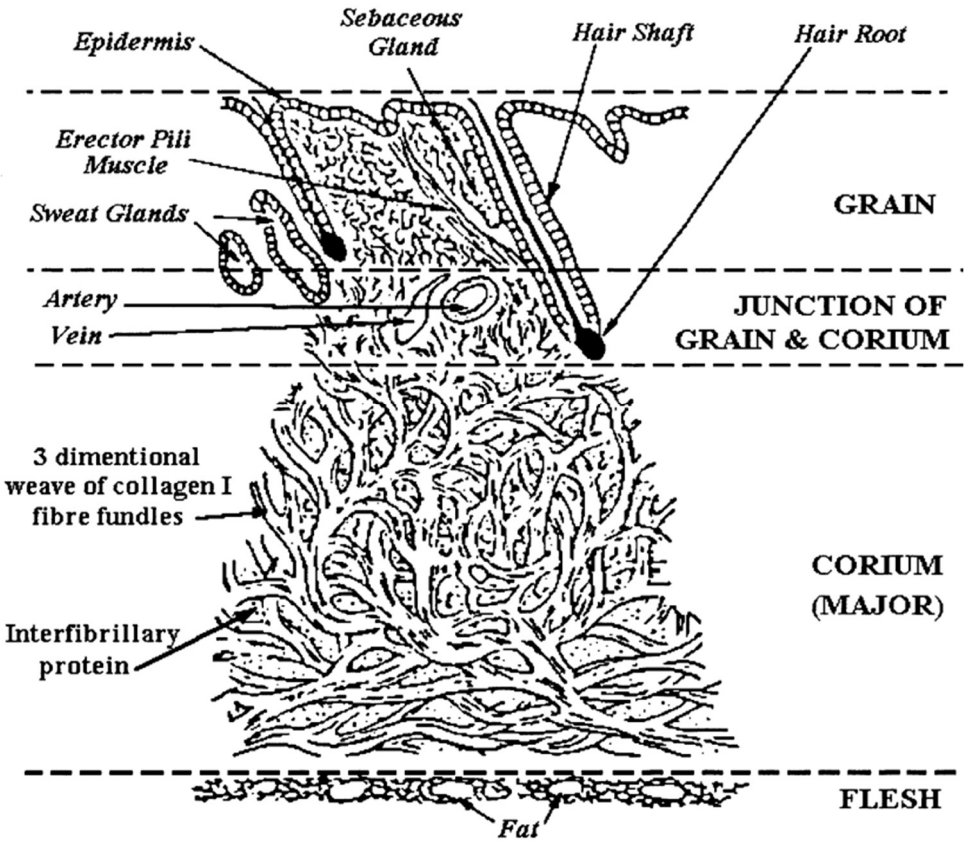

Figure 17: Cross section of the cattle hide.

Fibers and fiber bundles are the mainly constituents of core structural units of leather, forming a 3D network. Fibers are divided in different structures.

The primary component of the leather is collagen, a fibrous biopolymer made up of amino acid residues with distinct structures (R in the chemical formula), leading to different collagen types. In vertebrates, collagen types known are at least 19 [136]. Type I is the most present in leather. Also type III and V are contained in the material, but in small amounts [137].

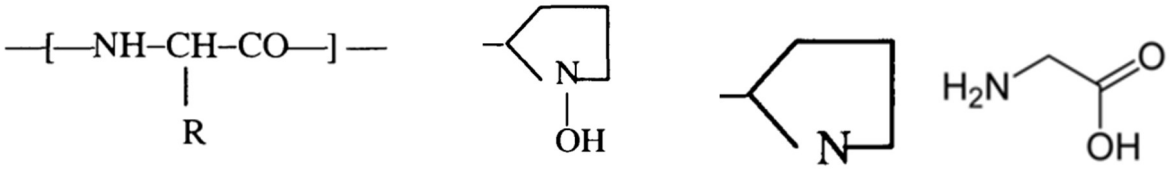

(a) Amino acid. (b) Hydroxyproline. (c) Proline. (d) Glycine (Gly).

Figure 18: Chemical formula of different collagen components.

Type I collagen molecules follow a repeating Gly-X-Y pattern, where Gly is glycine, the simplest stable amino acid, X and Y represent different amino acids arranged in a variable but not entirely random manner. X and Y positions are abundant in proline and hydroxyproline, making up approximately 12.2% and 9.4%, respectively, in type I collagen from cattle hide [137]. Chemical formulas of these elements are represented in Figure 18. The presence of five-membered rings in three amino acids plays a crucial role in the 3D conformation of collagen chains, which give the typical helical structure instead of the linear one.

Three collagen molecules intertwine to form a tropocollagen molecule, a right-handed triple helix, that pack together to other tropocollagen molecules in a “quarter stagger” arrangement, resulting in a periodicity of the order of dozens of nanometers [138]. These tropocollagen assemblies collectively form fibrils, containing approximately 7000 collagen molecules. Further examination reveals fibrils within fibers, which, in turn, constitute fiber bundles. The latter can reach sizes of up to 0.1 mm in diameter and indefinite length. A summary of the composition of leather is done in Figure 19.

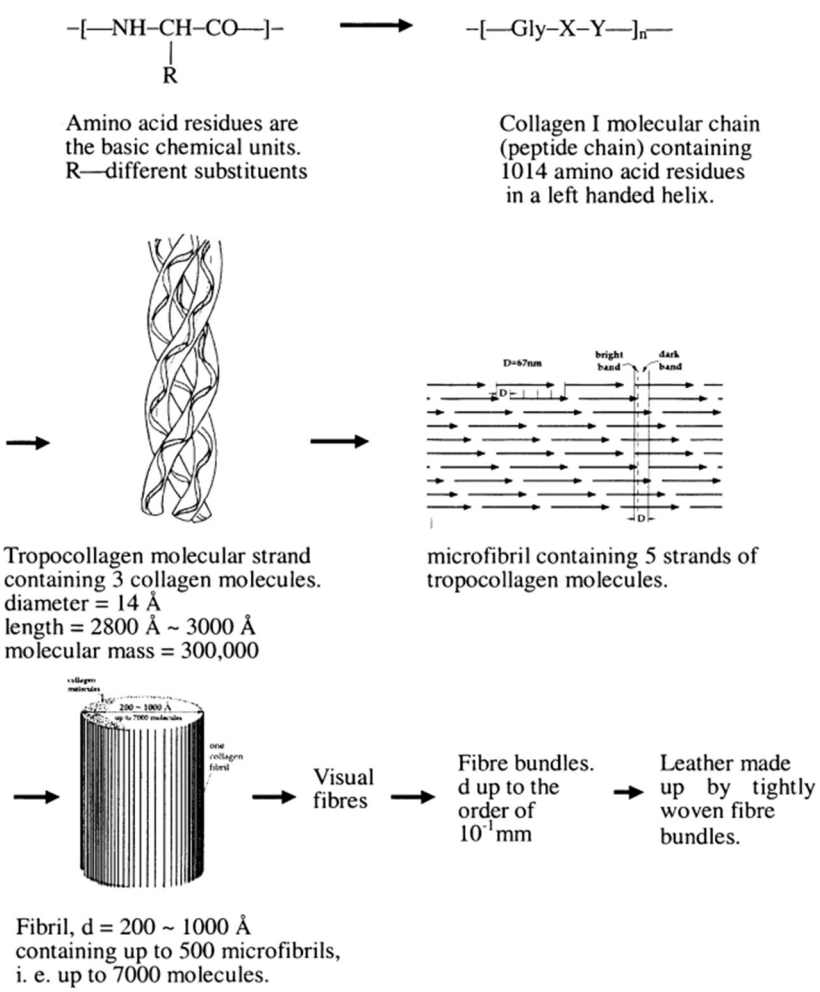

Figure 19: Summary of leather composition.

Summarizing, leather, crafted from animal skins, maintains its natural multi-layered structure, even through intensive tanning processes. Collagen, the core component, forms intricate molecular arrangements, including tropocollagen molecules, fibrils, and fiber bundles, contributing to the unique properties that make the leather wanted in different fields. [133]

5.4. Production

Leather production process provides four different steps, each serving a different purpose [127]:

1. Pretanning or beamhouse process:

   In the initial stage of leather production, raw hides or skins are prepared to prevent bacterial damage and putrefaction. Controlling parameters like temperature, pH, humidity, and contaminants is crucial. The curing process is used to delay degradation until leather production begins.

2. Tanning:

   Prepared hides or skins undergo tanning, which consists of chemical treatment to transform them into durable leather. Tanning agents are used to stabilize collagen fibers and improve its strength and resistance to decay.

3. Dyeing, retanning, fat liquoring:

   Leather is subjected to processes such as dyeing, retanning, and fat liquoring. In this step color is imparted to the leather, properties are enhanced, and softness and flexibility are provided to the material.

4. Leather finishing:

   This is the last step. It involves different finishing treatments to give the desired appearance and characteristics to the leather. Polishing, embossing, and applying protective coatings to improve durability and aesthetics are included in the process.

The first stage of beamhouse process is soaking, in which the animal skins go through a thorough soak with water and additives. The goal of this step is the elimination of any excess salt, dirt, dung, and blood, while also restoring the skins' suitable water content. In some countries, the solid portion of the salt is removed by mechanical or manual process, before adding water. This is useful to reduce chloride concentrations in the wastewater. [127]

Liming represents the second step. The soaked skins are immersed in a solution containing sulphide and alkali to break down the hair structure at its weakest point, the hair root, by reducing cystine sulphur-sulphur linkages, an important component of keratin. This facilitates the removal of hair and also eliminates unwanted substances such as non-structured proteins, fats, and hyaluronic acid. Collagen undergoes chemical modifications and swells, resulting in a more open structure, and altering the properties of the skin protein.

Fleshing step aims to eliminate any remaining flesh and subcutaneous tissue through a mechanical process.

Deliming-bathing step is the following one, in which a controlled enzymatic digestion further opens up the skin structure, ensuring the removal of any residual epidermis or unwanted materials. [139]

Picking stage is the next one. It is necessary to prepare the skins for the subsequent tanning process. It involves a chemical treatment based on acids, usually formic and sulphuric acid. Sodium chloride is added to the solution to prevent the pelt from

dangerous acid swelling due to the strong pH reduction below the isoelectric point. [140]

In the tanning process, the skin is chemically stabilized and transformed into a material that resists to putrefaction. Different chemistries can be employed for this transformation, but the most used tanning agent in the leather industry is the chromium (III) basic sulphate. Despite the numerous scientific research, the exact chemistry of tanning reactions still remains somewhat unclear [139]. For many years, the dominant theory in tanning elucidates the reinforcement of collagen by creating crosslinks within its triple helix structure [141]. However, it seems that altering the outer layer of water molecules surrounding the molecules in question also plays a significant role in this transformation [142]. All types of tanning processes lead to an improvement in the collagen's resistance to external factors as temperature and moisture, with the degree of improvement mainly determined by the specific tanning agent used. [139]

After the tanning step, hides are treated with alkali and undergo dyeing. In this process retanning and the application of fatty substances are involved to prevent the fibers from sticking together, resulting in softer leather.

The excess of water is removed by drying, and the appearance of the leather is enhanced through surface finishing, in which a variety of acrylic, polyurethane, and other synthetic polymers, combined with natural substances (oil, waxes, caseins, albumins, cellulose esters, and more) are used to form films. The utilization of these materials and methods in tandem ensures the creation of lively and enduring finishes. [139]

5.5. Properties

Growing environmental concerns have sparked increased interest in natural materials. Extensive research has explored substances like spider silk, plant fibers, and leather due to their broad applications. Leather's unique microstructure complicates its behavior, primarily responding to tension while resisting compression poorly. Numerous natural factors (animal race, age, sex, tanning type, etc.), environmental conditions (temperature, relative humidity) [143], and production processes (liming, tanning, fatliquoring, etc.) influence its behavior, offering opportunities for tailored applications. Leather research has evolved, focusing on chemical treatments and laminates, with limited exploration of microstructure-mechanical property links [144]–[146]. This presents untapped challenges in mechanics.

Few scientific papers can be found in the literature that deal specifically with the mechanical properties of leather. Zheng Li et al. [147] analyses the properties of two natural cow leather with vegetable tanning and dried in air, one cut in longitudinal direction (parallel to the backbone of the animal) and one in transverse direction (perpendicular to the backbone). Tensile test at different sample orientation, tensile test at different relative humidity levels, and creep test at different sample orientation were performed. In the first one, the results of the two different types of leather are similar, has shown in Figure 20. Longitudinal sample shows a Young's modulus of 94 MPa and the transversal one 100 MPa.

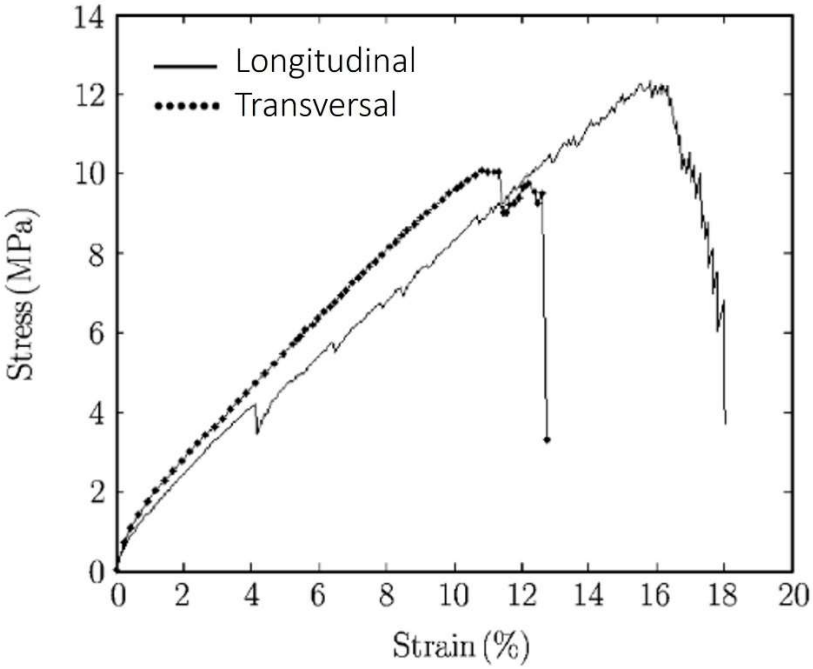

Figure 20: Tensile test on transversal and longitudinal samples.

In relative humidity test, two different tensile tests were conducted on transverse samples at a constant temperature of 21°C, with humidity conditions set at 20% and 60% respectively. Figure 21 shows that in high humidity test no beak appeared and the behaviour is not clearly linear. A higher relative humidity level increased the strain at break and decreases the young's modulus, acting as a plasticizer. The dry sample failed due to formation of cracks, which has not been observed in the 60% humidity sample. Therefore, also the stress at break is higher in the latter condition.

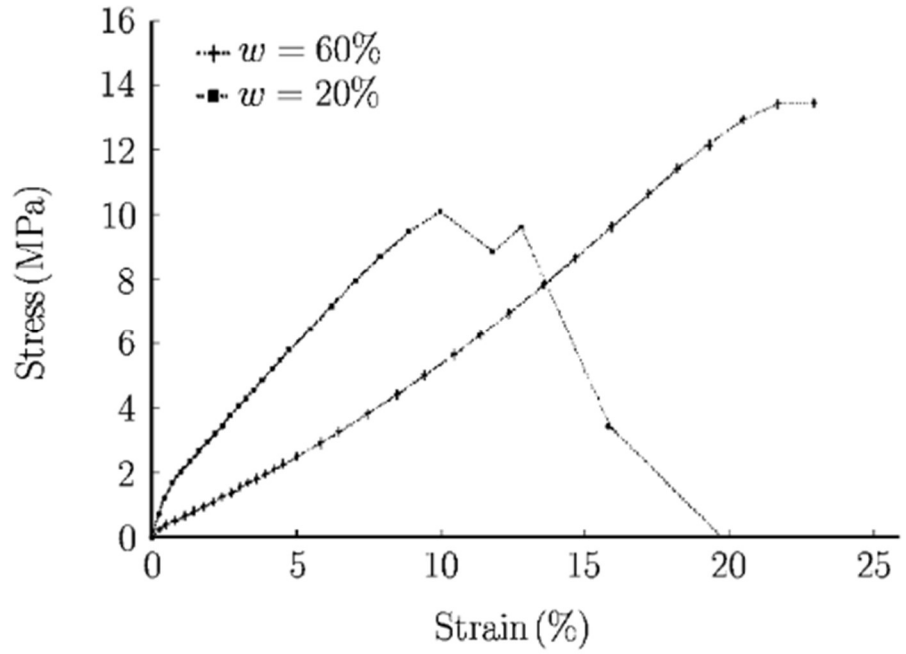

Figure 21: Relative humidity test on transversal sample at 20% and 60% of humidity.

For the creep test, the longitudinal and transversal samples are investigated at room temperature and 50% of relative humidity. Fibers have viscoelastic behaviour until elongation reaches a maximum. In Figure 22 can be seen that both samples show creep. The transversal one has a faster creep; the longitudinal one, consistent with what was observed in simple tensile tests, breaks at higher deformation.

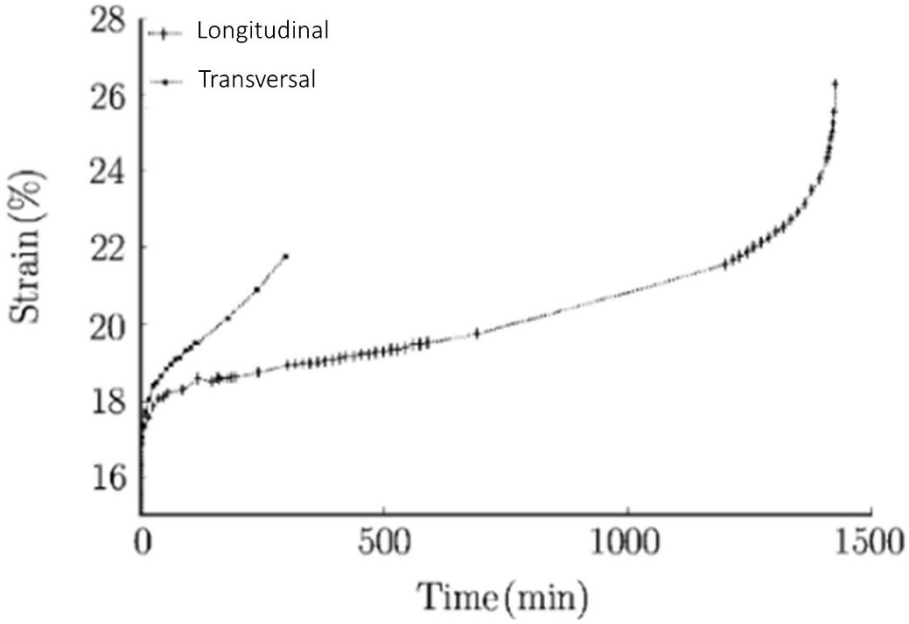

Figure 22: Creep test on transversal and longitudinal samples.

Leather's microstructure comprises randomly woven, tanned collagen fibers with a compact grain on the surface and a corium of tanned collagen fibers. It's heterogeneous

and anisotropic. Leather becomes weaker in low moisture conditions and displays a nonlinear stress-strain relationship at approximately 60% relative humidity. Furthermore, creep tests indicate viscoelastic flow in leather.

C. Liu et al. [148] have reported differences in mechanical properties between chrome-tanned leather and chrome free leather. The commercial samples were placed at room temperature with 65% relative humidity for a week before tests. Cyclic tensile test on Cr-tanned and Cr-free samples, stress relaxation test on Cr-tanned and Cr-free samples, and stress relaxation test at different fatliquoring conditions were performed. Figure 23 illustrates the stress-strain curves for both chrome-tanned and chrome-free leather over five cycles, starting from 0% of strain, until 20% strain, and then back to 0%. Chrome-tanned leather shows a better resilience (63%) than the chrome-free leather (48%). To calculate the result, first, find the average of the "zero strain" values; then, subtract the percentage of strain from this average value. Finally, divide the result by the percentage of strain. Also the peak stress is different.

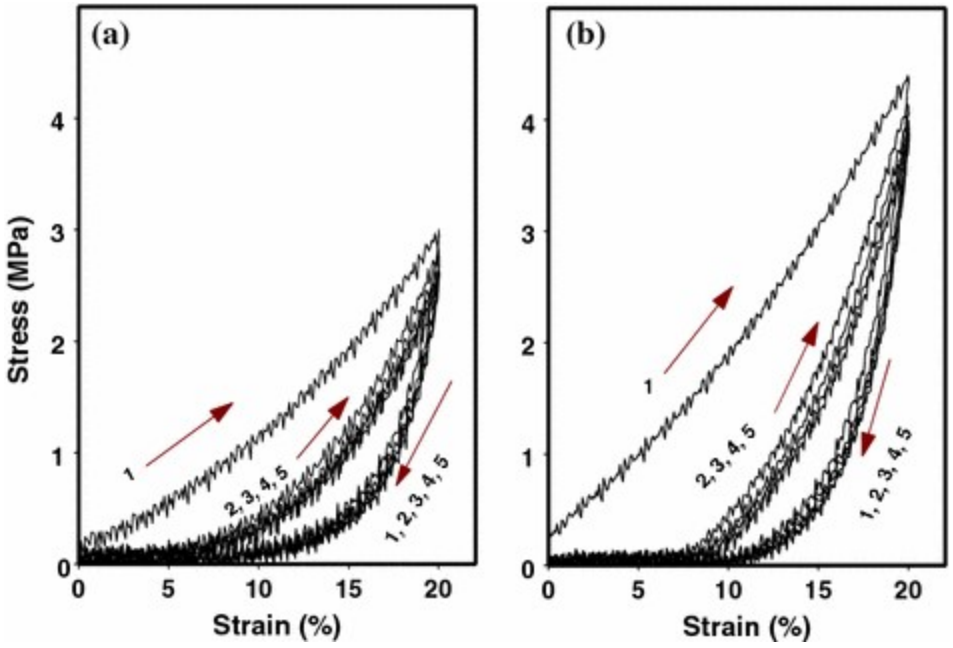

Figure 23: Tensile test on (a) chrome-tanned leather and (b) chrome-free leather.

In stress relaxation experiments, samples have been axially elongated by 20% and the stress has been measured during time. Curves' behaviour is very similar to each other; the only difference is the value of the curves. Chrome-free leather starts at 4.5 MPa and chrome-tanned leather at 2.7 MPa, meaning that the first one is stiffer. Figure 24 illustrates the test.

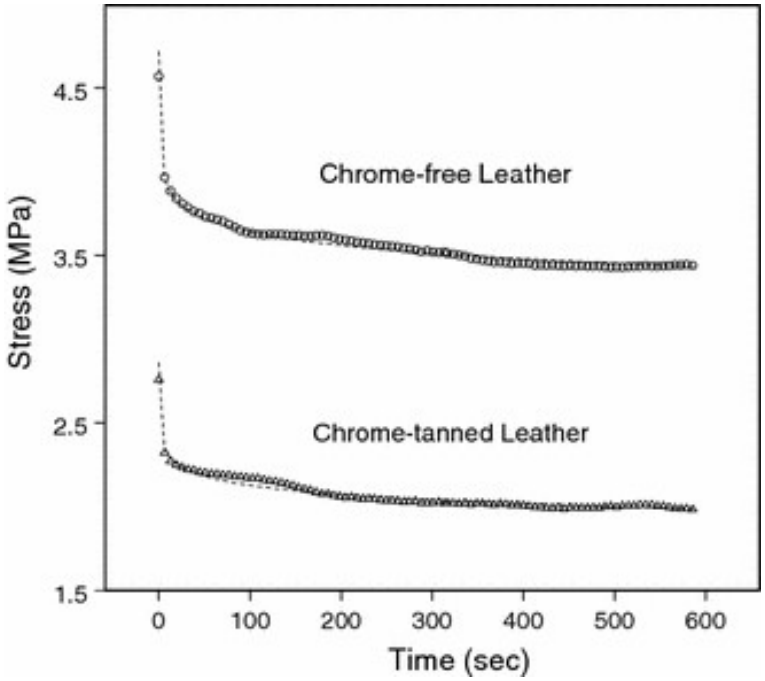

Figure 24: Stress relaxation test on chrome and chrome-free leather.

Fatliquoring is a process that reduces the initial strain energy or Young's modulus in the leather by lubricating its fibers. This effect is evident in the leather's lower Young's modulus and reduced initial strain energy [149]. Fatliquoring enhances leather's pliability and softness, in particular after the drying process. Figure 25 shows the effect of different contents of fatliquor on the stress relaxation tests, with same input and output of the previous test. Increasing the fatliquor content, the stress decreases.

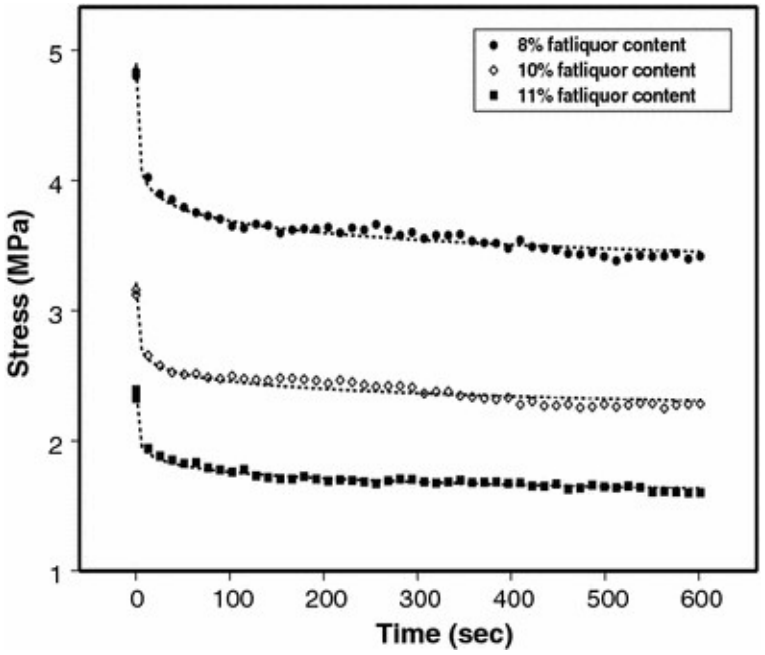

Figure 25: Stress relaxation of different % of fatliquor content.

In conclusion, chrome-free leather exhibits lower structural stability compared to chrome-tanned leather, with more easily converted potential energy into heat during deformation. Stress relaxations tests reveal that chrome-free leather is relatively stiffer. Fatliquor content significantly influences leather's viscoelastic properties, with higher fatliquor levels enhancing lubrication.

5.6. Alternatives

Nowadays, the best alternative to leather is polyurethane (PU). It's used to produce synthetic leather, coating a base fabric. Typically, this involves crafting a textile from synthetic fibers. [150]

PU is a polymer compound consisting of both hard and soft segments with a urethane bond (-NHCOO), Figure 26, in its molecular structure [151]. Soft segments, with lower T_g, act as reversible elastomeric phases, while hard segments, with higher T_g, behave as a rigid unit with shape memory [152]. By carefully designing these segments, it's possible to create polyurethanes with tailored mechanical properties, including flexibility, strength, and transition temperature, making them versatile materials for various applications [153]. Its properties depend on the monomer type and processing method, influencing perceived properties like tactile feel and appearance, as well as functional characteristics as moisture permeability and water resistance [150].

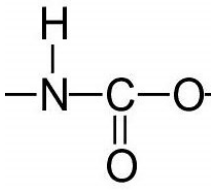

Figure 26: Urethane bond.

PUs are synthesized using a two-step prepolymer method, with adjustments made to the hard-segment/soft-segment ratio. The chemical reaction occurs between polyols, that represent the soft-segments, diisocyanates, that represents the hard-segments, and chain extenders. Figure 27 shows the reaction with PTMG (poly(oxytetramethylene) glycol) as soft-segment, MDI (4,4'-methylenediphenyl diisocyanate) or TDI (toluene 2,4-diisocyanate) as hard-segment, and BD (1,4-butanediol) as chain extender. [153]

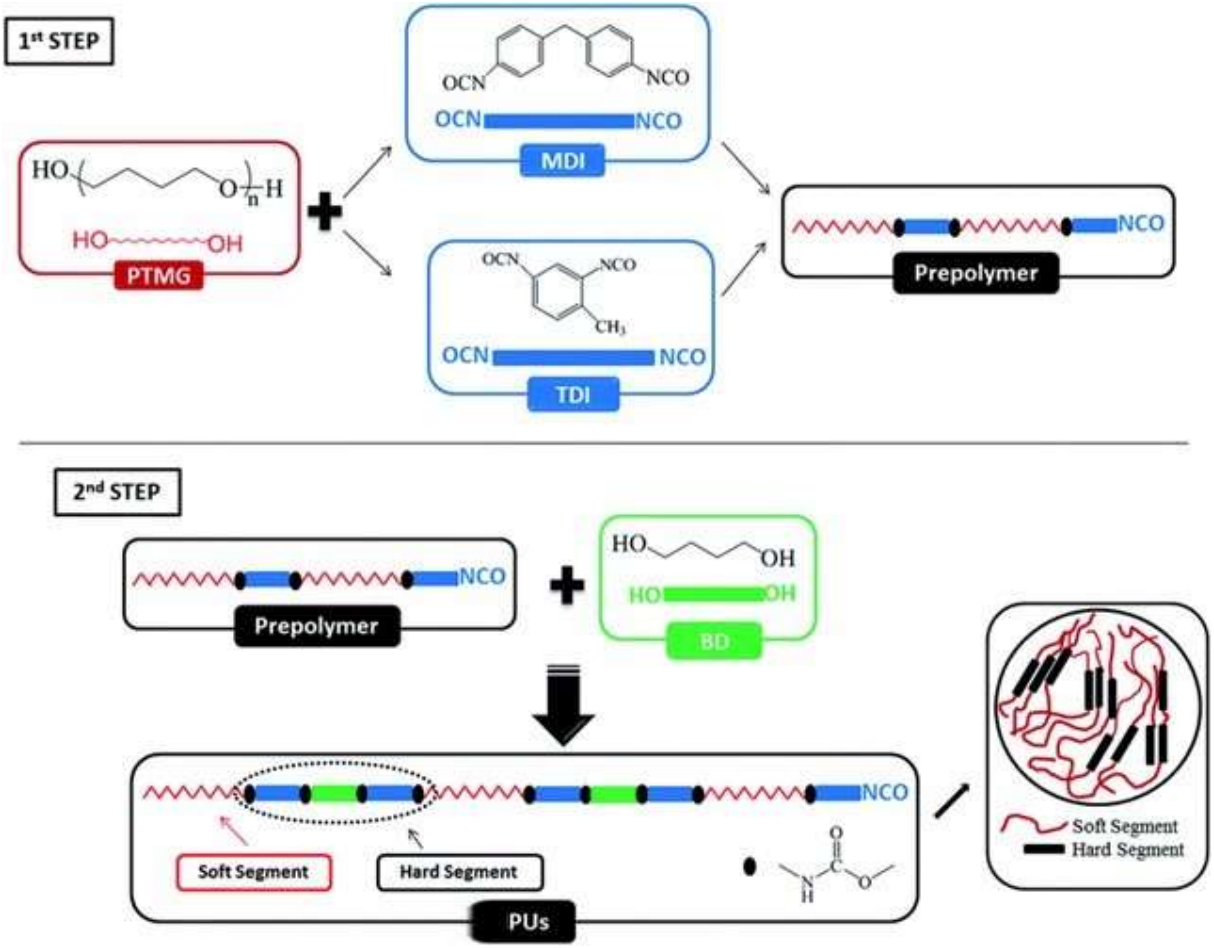

Figure 27: Two-step synthesis scheme for PUs.

Basing on diisocyanates type [154] and stoichiometric amounts of polyol/diisocyanate/chain extender [153], different materials' properties are obtained, including T_g, stress and strain at break, Young's modulus, toughness, etc.

D.K. Lee et al. [154] analyses the mechanical and thermal behaviour of PU based on different diisocyanates. MDI and T80 represent the most used synthetic leathers, which T80 is toluene diisocyanate containing 80% 2,4-isomer and 20% 2,6-isomer. As regard the T_g, it can change between -72°C (in case of isophorone diisocyanate (IPDI), hydrogenated 4,4'-diphenylmethane diisocyanate (HMDI), and 1,6-hexane diisocyanate (HDI)) to -69°C (in case of MDI) for PU without chain extender. Under mechanical aspect, important variation can be observed: 17.5÷49.3 MPa for Young's Modulus (T80 and MDI respectively); 9.5÷42.9 MPa for tensile strength (IPDI and MDI); 200÷1480 % for elongation at break (HDI and TDI). The previous datas are referred to PU with high-segments content of 40% w/w. Instead, M. Sáenz-Pérez et al. [153] investigated the different behaviour of MDI and TDI by varying the hard-segments and chain extenders contents.

It can be seen that, due to the remarkable versatility of processing and, consequently, of mechanical and thermal properties, PUs are suitable for various fields of application. Moreover, it is possible to use completely different materials for the same field, as in the case of synthetic leather.

5.7. Environmental impact

Leather has held a pivotal role in humanity's early history. However, over the past century, mounting environmental issues have come to the forefront, initially centred around water pollution in the twentieth century and later evolving into a broader global perspective in recent decades. Stringent environmental regulations in Europe, coupled with rising labour costs, prompted a shift in leather production from industrialized nations to developing ones, such as Latin America, India, and China. This rapid expansion in these regions gave rise to various environmental challenges, primarily impacting agriculture and access to clean water. Consequently, questions arose regarding the sustainability of the leather industry. [155]

To address these concerns, the global leather industry has undertaken widespread innovation and initiatives to tackle the environmental issues stemming from its production processes. This includes efforts to reduce water consumption, improve wastewater treatment, enhance solid-waste recovery, and minimize the use of certain chemicals like chromium and sodium sulphide. [131]

Nevertheless, contemporary society and markets now demand a more comprehensive approach that encompasses the entire leather value chain. Traceability has become a paramount concern, ensuring the absence of child labour and sourcing hides from animal-friendly farms, among other considerations. Additionally, there is a growing emphasis on embracing a circular economy, where resources are used in a sustainable manner, promoting long-term environmental viability.

In defining the goal and scope of an LCA study, it is essential to clarify the study's purpose. This involves illustrating the study's boundaries and extent. As depicted in Figure 28, when conducting an LCA for leather production 'from cradle to gate', it is imperative to encompass all upstream activities, including farming and animal slaughtering. This should be coupled with the core processes occurring at the tannery itself, as well as the transportation activities required to move materials between these stages. Furthermore, the assessment should encompass the environmental impacts stemming from chemical production, energy consumption, and water usage within our system. Additionally, it should account for the consequences associated with waste generation and wastewater treatment processes. [156]

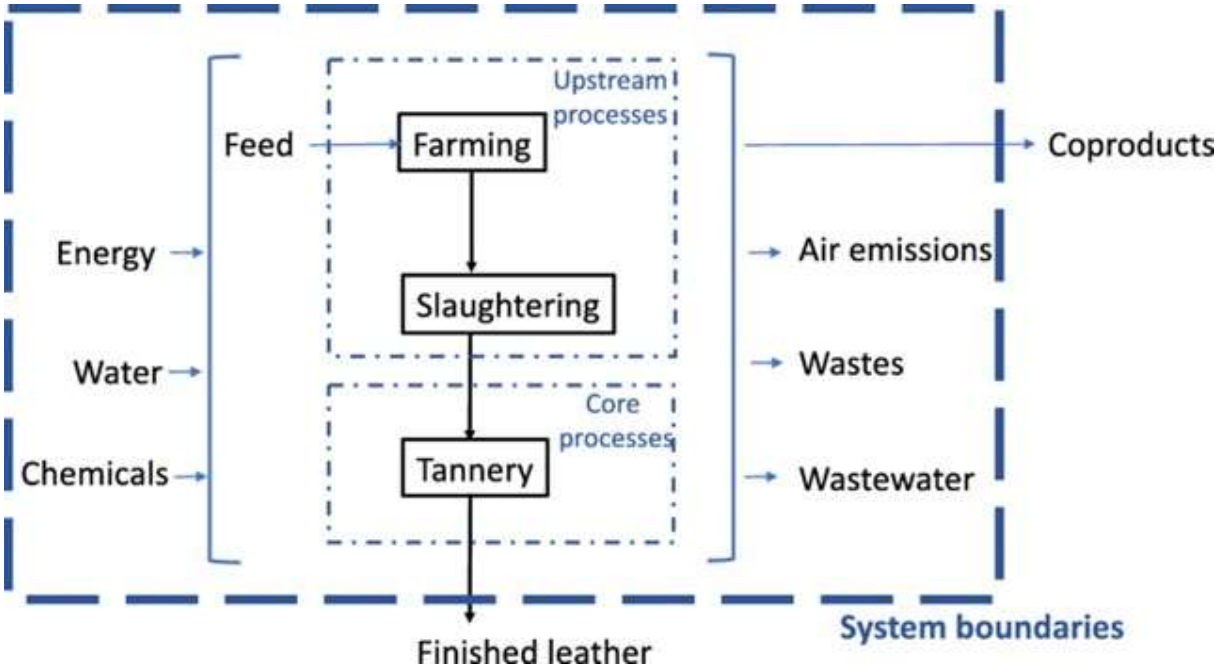

Figure 28: LCA study for leather production 'from cradle to gate'.

The leather industry is notorious for its significant environmental impact and resource-intensive practices. To produce just 0.25 Mg of leather, it consumes a staggering 1 Mg of raw materials and requires between 15,000 to 120,000 m^3 of water. This process results in the generation of 15–50 Mg of wastewater and 400–700 kg of solid waste [131], accompanied by emissions of odours, greenhouse gases such as CO_2, H_2S, NH_3, and volatile organic compounds like amines, aldehydes, and hydrocarbons. The quantity of chemicals released depends on the treatment methods and technology employed in tanneries [157]. The global leather industry has an estimated annual production capacity of approximately 15 million tons, highlighting the magnitude of the issue [131].

The tanning industry generates a diverse array of waste materials that differ in physical state and composition. These variations correspond to different risks associated with their management and necessitate distinct processing and utilization methods. Solid waste arising from both tanned and untanned hides and skins can be further categorized into numerous subgroups. In contrast, liquid waste, often in the form of wastewater, is produced in significantly larger quantities. Figure 29 illustrates the various types of waste produced by the tanning process and provides examples of how these wastes can be repurposed.

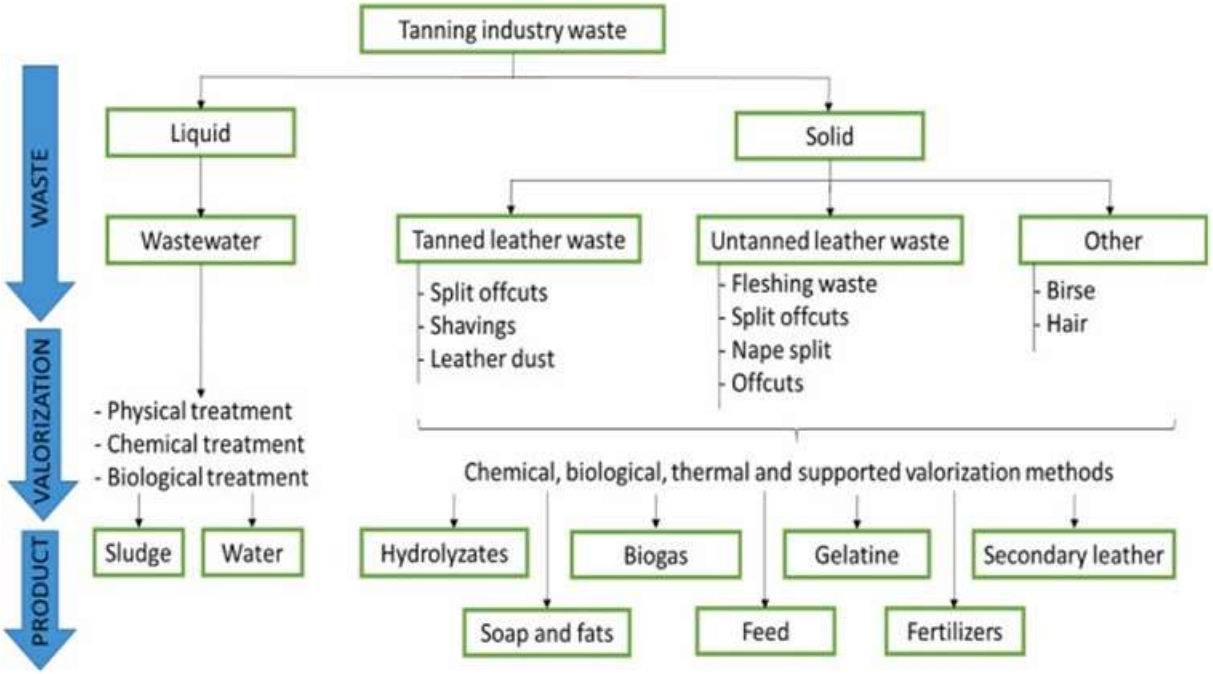

Figure 29: Tanning process wastes and their valorization.

For detailed insights into the characteristics of specific tannery wastes, along with a breakdown of valuable and potentially hazardous components, please refer to Table 1. [132]

Table 1: Tannery wastes.

Waste	Definition	Production
Wastewater and effluents	Liquid wastes from leather pretreatment and treatment	10-12 m^3 per 1 Mg of processed skin
Tannery sludge	Solid waste form wastewater and effluents treatment	8.4-12.1 kg per 1 m^3 of treated wastewater
Split and offcuts	Unusable solid waste from leather processing (shaping, cutting)	4.3-6.5 kg per 1 Mg of processed leather
Shavings	Solid waste from the trimming and leather shaping process	100 kg per 1 Mg of processed leather
Leather dust	Micro-fined powder of collagenous fibrils being dangerous solid waste generated via leather buffing (carcinogenic properties)	2-6 kg per 1 Mg of processed leather
Fleshing waste	Skin-residue waste from hides' tanning process, originated by the removal of the tissue adhered to the animal hide	50 kg per 1 Mg of processed skin
Hair and birse	Solid waste generated at hair pulping process	3.5 kg per 1 Mg of processed skin

Historically, tanneries have primarily relied on landfilling and partial disposal for waste management, mainly due to economic considerations. However, there is growing recognition that tannery waste represents a valuable and renewable resource that could contribute significantly to sustainable development. Implementing a Circular Economy strategy and harnessing the potential of leather waste can result in cost savings for waste management and emission control. This waste contains significant amounts of protein, fat, and water [157], making it a resource for hydrolysis to obtain collagen or gelatine for the pharmaceutical and cosmetic industries [158], as well as for extracting fats, producing biofuels [159], and creating various valuable products like activated carbon [160], sound-absorbing biopolymers [161], surfactants [162], and organic fertilizers [163]. Chromium, commonly used in leather tanning, poses a severe contamination risk, especially due to its mutagenic and carcinogenic potential. Treatment methods involving organic chelates or mineral acids can be used to recover chromium, and tannery waste can be thermally treated to recover chromium as Cr_2O_3 for use in steel production [164].

6 Aim of this work

Leather industry originates huge amounts of wastes and has a heavy environmental impact.

The aim of this work is to apply principles of circular economy to leather industry. To do so, leather industrial waste will be recovered and used as a filler in polymer-leather composite materials that can, in principle, be reintroduced into fashion market.

Figure 30 shows the path that has been foreseen for leather scraps.

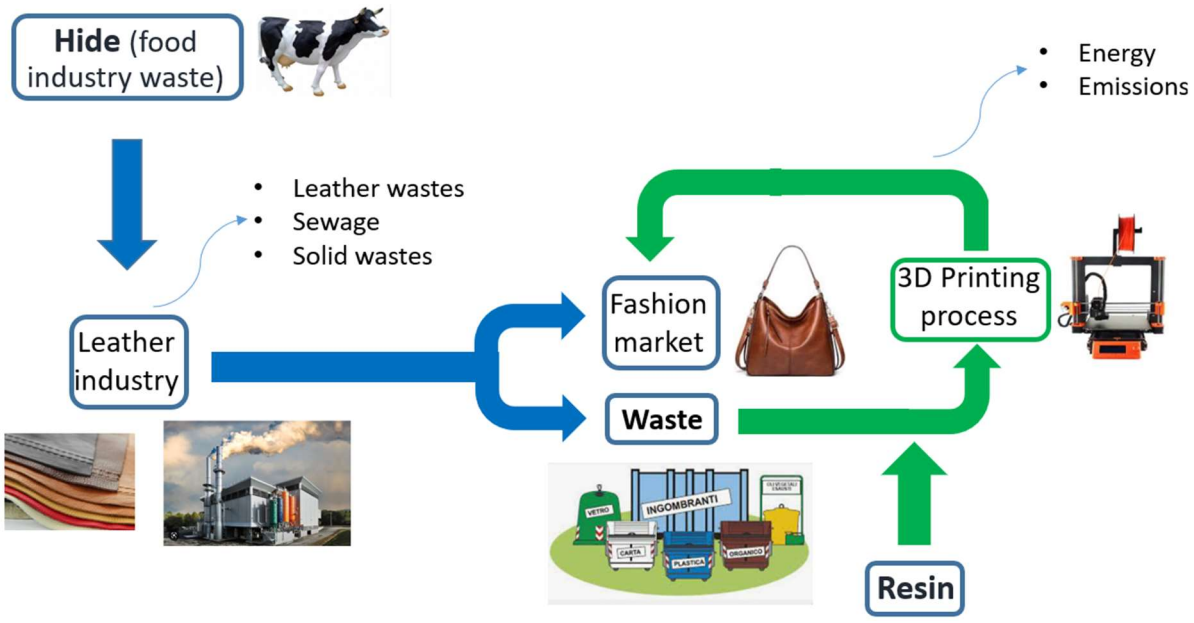

Figure 30: Graphical scheme of linear industrial leather production (blue) and circular 3D Printing with leather waste production (green).

Additive manufacturing, and in particular Direct Ink Writing, has been selected as promising technology for this scope. Indeed, such technology allows to process a wide variety of materials in liquid form with minimum material waste and energy consumption.

Using this approach, crosslinkable materials can be formulated: they can be 3D-Printed in a liquid form and then crosslinked to obtain the final properties.

Prior to actual experimentation, comparative LCA analysis will be performed in order to assess the actual environmental benefits of producing leather-like materials using leather scraps.

Two different resins (one rigid and one flexible) will be then investigated as matrices for the aforementioned composites. In both cases, different leather contents will be used.

After the formulation of the composite materials, characterization will be carried out.

Suitability of Direct Ink Writing can be assessed through rheological tests and printability analysis.

The actual correctness of processing and correct crosslinking will be evaluated through DSC, UV-DSC and by measuring the gel content.

Finally, tensile tests will allow to assess mechanical properties of the material and their suitability for the scope. Both cast and 3D-Printed specimen will be analyzed.

7 Materials and Methods

In this section, an inventory of the various materials employed in the thesis project is presented, offering concise descriptions of their distinctive attributes. Subsequently, we delve into comprehensive explanations of the formulation methods and characterization techniques that have been applied.

An in-depth study of the different composite materials was carried out. Two different polymer resins were studied as matrices for the leather filler: one rigid (ethoxylate bisphenol A diacrylate hereinafter SR349) and one flexible (poly(vinyl alcohol) or PVA). Subsequently, analyses of materials properties were carried out. The test specimens analysed for tensile tests, in order to assess the mechanical properties of the formulations, were both cast and printed using the DIW technique.

7.1. LCA

A comparative LCA has been carried out, comparing virgin leather with a hypothetical resin-leather composite material. As regards the matrix, a general acrylic resin has been considered as representative material. Quantitative data has been taken from literature review [174]–[176].

Raw materials needed for this comparison are vergin leather and acrylic resin.

The functional units taken into account for the two are, respectively, are 0.54 m^2 of 1.6 mm thick leather (usually corresponding to about 660g) and 255g of conventional photocurable acrylic resin. The life cycle impact assessment method chosen is ReCiPe Midpoint (H). Data regarding the resin available in literature is expressed using the International Reference Life Cycle Data System (ILCD) Midpoint+ method. Therefore, it has been converted to ReCiPe Midpoint (H) using inventory tables [176].

The impact parameters selected are Climate change (kg CO_2 eq), and Acidification (kg SO_2 eq). In each category, production, distribution, and disposal step are taken into account.

Figure 30 shows a comparison between typical leather industry (blue linear cycle) and the 3D printing with leather waste (green circular cycle). Leather represents a food industry waste, so it is itself a produced recovering an industrial waste. For leather impact assessment, tanning process, leather product manufacture, and end of life were

taken into account with respective output processes (leather and solid wastes, sewage, harmful substances, emissions).

Figure 30: Graphical scheme of linear industrial leather production (blue) and circular 3D Printing with leather waste production (green).

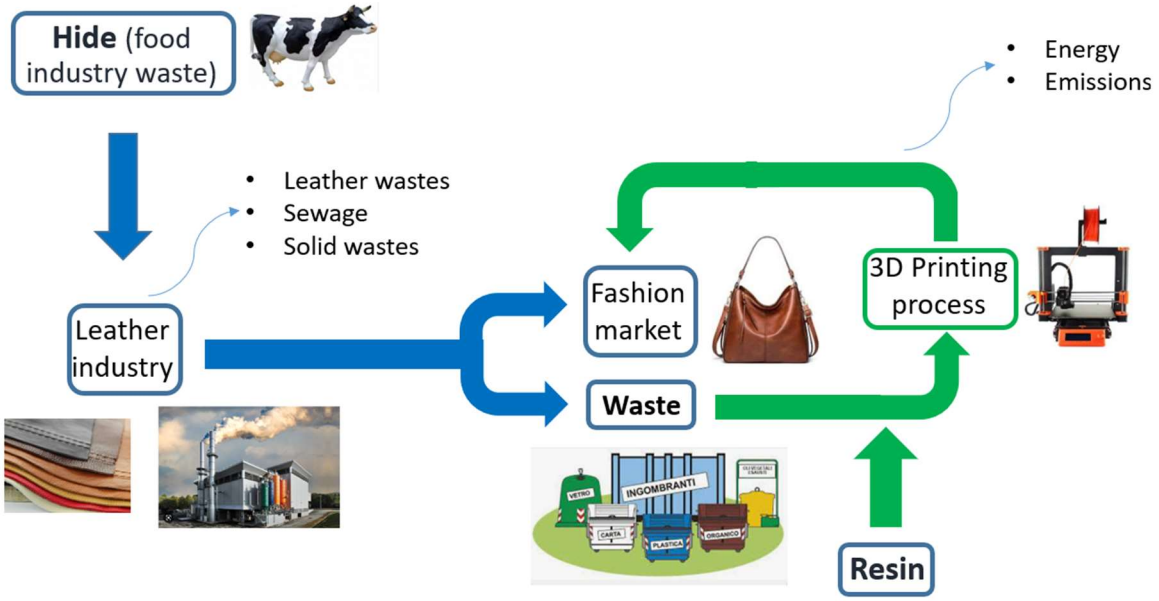

Figure 30: Graphical scheme of linear industrial leather production (blue) and circular 3D Printing with leather waste production (green).

3D printing project offers an alternative to leather wastes and end of life of leather products, thanks to thanks to minimal waste production and low energy consumption (mainly due to UV curing). The goal is, through circular economy, reintroducing the material into the fashion industry. By doing so, the production of leather is reduced and thus the recycling of raw animal skin. Consequently, the impact of raw animal leather, which is not recycled, is considered as an additional impact. Furthermore, emissions related to composite processing were assumed to be zero. In this case, the environmental impact of the leather wastes, used as a raw material, is assumed as null, coming as a byproduct of another industry [174]. Energy, emissions, and solid wastes were considered as output processes.

Environmental impacts (EI), for both parameters, of composite material were calculated for each composition using the following formula:

$$EI = EI_{Recycled\ leather\ from\ waste} \cdot x + EI_{Recycled\ leather\ from\ hides} \cdot x + EI_{Acrylic\ resin} \cdot (1\text{-}x) \quad (4)$$

where EI are respectively the environmental impact of 1 kg of acrylic resin and recycled leather; x represents the percentages of leather.

7.2. Materials

Milled leather scraps were supplied from Stazione Sperimentale Italiana Pelli (SSIP), Italy. The material is shaved gluteraldehyde-tanned leather, which was sieved in a 0.5 mm sieve before use. The ethoxylate bisphenol A diacrylate resin, hereinafter named SR349, was purchased from Arkema (local distributor: Came S.r.l., Italy). Ethyl phenyl (2, 4, 6-trimethyl benzoyl) phosphinate, named TPO-L, was purchased from Lambson Limited, UK. AEROSIL® R 106 (hydrophobic fumed silica) was purchased from EVONIK, Germany. Hydrophilic fumed silica (S5505); dicumyl peroxide; triethoxy(octyl)silane; poly(vinyl alcohol), or PVA (Mw = 31.000÷50.000; 99% hydrolised); dimethyl sulfoxide (DMSO); glycidyl methacrylate (GMA); and glycerol were purchased from Sigma-Aldrich (local distributor: Merk Life Science S.r.l., Italy). N,N,N′,N′-Tetramethylethylenediamine (TEMED) was purchased from Fluka Honeywell, US. 2-Hydroxy-4′-(2-hydroxyethoxy)-2-methylpropiophenone, named Irgacure 2959, was purchased from BASF, Germany.

7.3. Material Formulation

7.3.1. SR349

This resin was chosen because the literature [91]–[93] indicates good mouldability and cross-linking. It belongs to the family of acrylic resins, which polymerise by free radical polyaddition. Free radical polyadditions are a class of chemical reactions in which molecules containing free radicals combine to form larger molecules. These reactions involve the formation of covalent bonds between the radicals, increasing the molecular weight of the compound. In polymer synthesis, free radicals propagate through the polymer chain, creating long, branched chains. Radical polyadditions are often initiated by trigger molecules, called initiators, which generate the first free radical upon application of external stimuli such as UV light or temperature. These radicals react with monomers, triggering the growth of polymer chains.

In case of acrylic resins, the free radicals propagate thanks to acrylic groups. A radical is formed through the breakage of $CH_2{=}CH_2$ double bond present in the acrylic group. Such radical is responsible for the propagation of the reaction and therefore for the formation of a polymer chain.

Having two acrylic groups, SR349 can form a continuous polymeric network and lead to the formation of a macroscopic crosslinked structure.

The photoinitiator TPO-L and its concentration was selected on the basis of UV light system used for UV-assisted three-dimensional printing, to obtain the best printability results and minimize the presence of unreacted groups in the resin, forming radicals at 395 nm. [92], [93]

Dicumyl peroxide, on the contrary, forms radicals when thermally activated, allowing thermal crosslinking of the resin.

Figure 31 shows the chemical scheme for the crosslinking reaction of the resin.

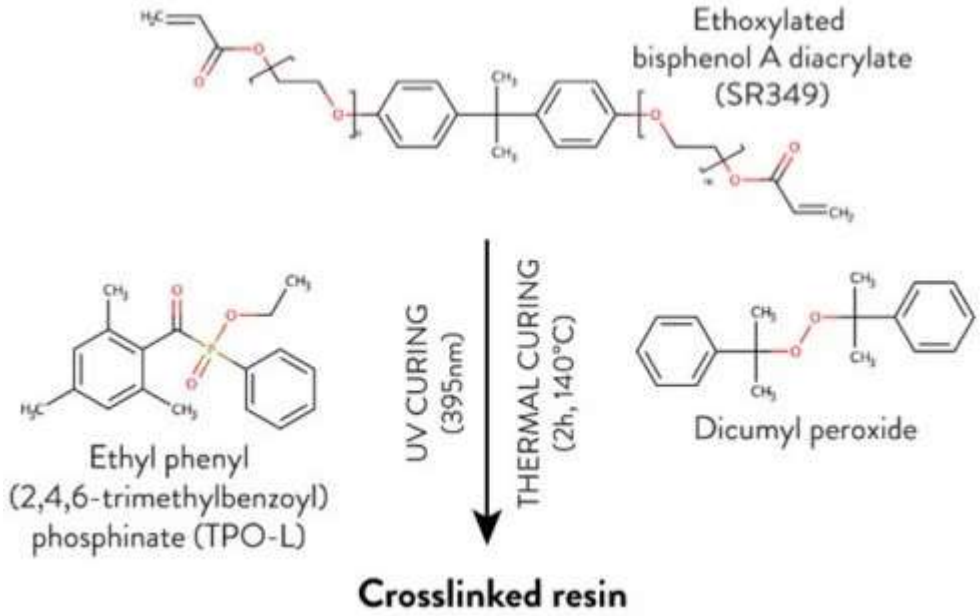

Figure 31: Chemical scheme for SR349 crosslinking.

Composed by resin, silica and TPO-L have been investigated. Silica has been added as a rheological modifier in order to make the formulation suitable for DIW.

SR349 with different percentages of silica (5, 10, 15, 20 % w/w with respect to the resin) were investigated. In the first case, the necessary amount of silica was first dispersed in acetone, using an ultrasonic processor at 20kHz and 52W, at room temperature for 45 minutes. Later, the dispersion was added to SR349 and 3% w/w with respect to the resin of TPO-L. Then the mixture was mechanically stirred at 100°C until complete evaporation of the acetone.

The formulation of leather-SR349 formulations has been carried out by dispersion of leather in acetone and subsequent addition to resin with stirring and evaporation of acetone at 100°C. Subsequently, 3% w/w of TPO-L and 0.3% w/w of dicumyl peroxide have been added and stirred until complete dissolution.

The thermal initiator has been added foreseeing leather ability to shield UV light. In this case, the complete crosslinking can be achieved by first UV irradiation and subsequent thermal treatment.

Leather is a polar filler, while SR349 is an apolar resin. Therefore, compatibility problem between the two were expected. For this reason, a second set of formulations have been prepared by pre-functionalizing the filler before addition to the mixture.

Functionalization has been carried out by dispersing leather particles into ethanol (1:50 w/v ratio) and then adding 6 % w/w with respect to leather of triethoxy(octyl)silane.

Functionalization occurred by mechanical stirring of the mixture for 26h at 50°C. [165], [166]

The expected reaction in an esterification reaction occurring between –OH groups present on leather (containing collagen) and oxygen atoms present on triethoxy(octyl)silane. This leads to the formation of an apolar layer (given by the presence of alkyl chains in the silane) on the surface of the filler.

Afterwards, three ethanol washings have been performed in order to remove reaction residues. Subsequently, functionalized leather has been added to resin and initiators in an analogous way as the non-functionalized formulations.

Sample were called as SRXY, where SR is referred to SR349, X is referred to filler type (S for silica and C for leather), Y is referred to weight percentage of filler with respect to the resin.

In Table 2 are reported all formulation with every percentage with respect to the total mass of the samples.

Table 2: SR349 formulations with respective weight percentages.

Sample	SR349%	Silica%	Leather%	TPOL%	Dicumyl peroxide %
SRS5	92.59%	4.63%	-	2.78%	-
SRS10	88.50%	8.85%	-	2.65%	-
SRS15	84.75%	12.71%	-	2.54%	-
SRS20	81.30%	16.26%	-	2.44%	-
SRC10	88.26%	-	8.83%	2.65%	0.26%
SRC15	84.53%	-	12.68%	2.54%	0.25%
SRC20	81.10%	-	16.22%	2.43%	0.24%

7.3.2. PVA

The second matrix, used for the composite formulation is a methacrylate form of PVA. The choice was made to have a water-soluble, UV-curable polymer, and non-soluble during the processing.

The formulation of PVA started from the dissolving of 10 grams of PVA pellets in a flask with 100 ml of dimethyl sulphoxide (DMSO). After that, 1.55 ml of GMA (5% mol/mol OH) and 0.339 ml of TEMED (1% mol/mol OH) were added to the solution with all in stirring at 60°C for 24 hours. Then the solution was poured through a dripper in 1 l of acetone in stirring at room temperature. Since acetone is not a solvent of PVA, the polymer precipitated and could be isolated. The material formed was collected in freshly acetone to remove excess of GMA and reaction residues. This operation has been done twice. The resultant amount of modified polymer is extracted from acetone and dried at 40°C.

Glycidyl methacrylate (GMA) is added as a source of photocrosslinkable groups (methacrylate) to modify PVA. A small GMA concentration (5% mol/mol OH) was chosen to have a water soluble material after the formulation. N,N,N′,N′-Tetramethylethylenediamine (TEMED) acts as catalyst. The esterification reaction between PVA and GMA occurs though the hydroxyl groups reactions of both compounds. The glycidol was obtained as by-product. Scheme reaction is illustrated in Figure 32. [167]

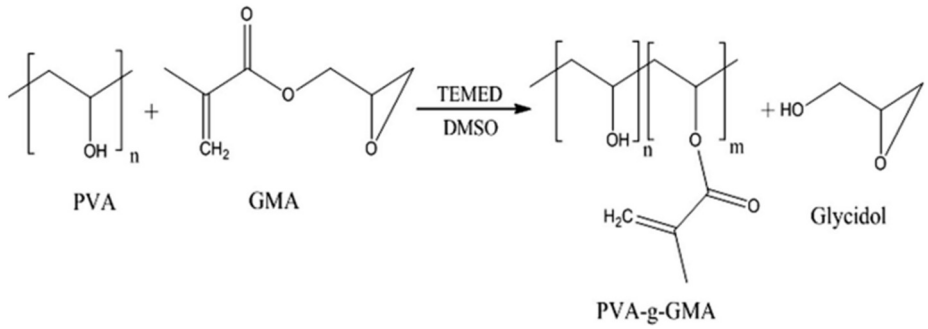

Figure 32: Methacrylation reaction of PVA.

Also PVA was previous evaluated with silica to understand the matrix behaviour. Different percentages of silica (0, 5, 10, 15, and 20 % w/w with respect to water) were dispersed in distilled water, with ultrasonic processor, for 45 minutes at 78W and room temperature. Subsequently, PVA is dissolved in the dispersion, in a ratio H_2O:PVA = 3:1 w/w, together with photoinitiator Irgacure 2959 (3% w/w with respect to the water), at 80°C in stirring.

Glycerol (20% w/w with respect to the PVA-water solution) has been added as a plasticizer.

Considering the formulations of interest (PVA+Leather), the matrix formulation analogous as the previous case (apart from the presence of silica), but the filler is added at the end of the process, in percentages of 20, 25, and 30 % w/w with respect to the matrix, together with 0.3% w/w with respect to distilled water of dicumyl at room temperature.

Also for PVA samples, they are named as PVAXY, where X is referred to filler type (S for silica and C for leather), Y is referred to weight percentage of filler with respect to the resin.

In Table 3 shows all formulation with every percentage with respect to the total mass of the samples.

Table 3: PVA formulations with respective weight percentages.

Sample	H_2O%	PVA%	Silica%	Leather%	Irgacure 2959 %	Dicumyl peroxide %	Glycerol%
PVAS10	57.94%	19.12%	5.79%	-	1.74%	-	15.41%
PVAS15	56.31%	18.58%	8.45%	-	1.69%	-	14.98%

PVAS20	54.76%	18.07%	10.95%	-	1.64%	-	14.57%
PVAC20	52.77%	17.41%	-	14.04%	1.58%	0.16%	14.04%
PVAC25	50.98%	16.82%	-	16.95%	1.53%	0.15%	13.56%
PVAC30	49.31%	16.27%	-	19.67%	1.48%	0.15%	13.12%

7.4. 3D-Printing

A tailor-made, home-assembled Chimera printer incorporating a pneumatic extruder equipped with 12 25mW/cm² Led emitting at 365 nm was used for UV-assisted 3D printing the composite formulations. Print speed ranged between 1 and 10 mm/s and a 0.41 mm tapered metallic nozzle, for silica formulations, and 1.6 mm, for leather formulation, were used. An image of the set-up used is shown in Fig. X. Samples were designed using "Fusion 360" software (Autodesk, US). In order to process the 3D model, the open-source slicing software "PrusaSlicer" (Prusa, Czech Republic) was used.

FOTO?

The strategy adopted for leather samples is a dual curing printing process, in which, after every printed layer, the plate moved under LED lamps for the first UV curing step to guarantee a self-sustainable structure. When the printing was completed, samples were subject to a second UV curing step with UVA lamp to complete the UV curing process. For leather formulations, a thermal curing was carried out in oven to reach the complete curing. Figure 33 shows the process.

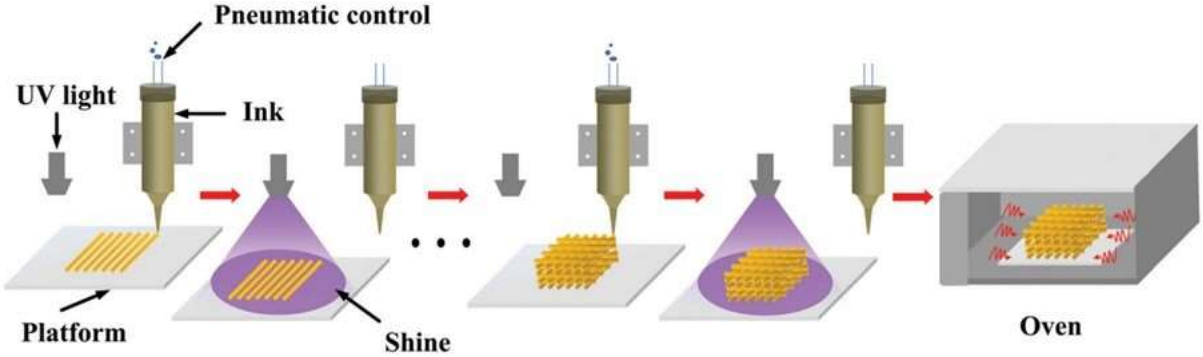

Figure 33: Scheme of dual curing strategy with 3D printing.

UV chamber Polymer 500 W, Helios Italquartz S.r.l., Italy, equipped with a UVA emittance mercury vapor lamp type Zs (950 W/m²), was used for the UV post-curing treatment.

7.5. Material Characterization

7.5.1. Filler dimensional characterization

An optical microscope analysis was carried out to investigate the characteristic dimensions of the leather particles. They were dispersed through stirring in ethanol solution with 1:1000 w/v ratio (0.01g leather : 10ml ethanol); then positioned on a glass slide until drying. 50 photos of the sieved and non-sieved leather were analysed with 50X lens, and the area and perimeter of the particles were calculated using ImageJ. A parameter, shows in Eq. 5, has been defined to quantify the shape and aspect ratio of the filler inscribing it in a circle (filler area/circle area). If the filler is spherical the parameter tends to 1, if it is filamentous the parameter tends to 0. Furthermore, the characteristic particle size has been defined as the diameter of the circle that can circumscribe the particle.

$$P = \frac{A_{filler}}{A_{circle}} \qquad 5$$

7.5.2. Characterization of PVA Methacrylation

The quantification of the degree of substitution (or methacrylation, DM) of the synthesized methacrylated PVA (PVAM) has been performed exploiting spectra obtained from proton nuclear magnetic resonance (H-NMR, Bruker AV 400 SampleXpress machine).

Sample preparation for the H-NMR analysis followed this procedure: 5 mg of PVA and 5 mg of PVAM were individually dissolved in 600 µl of deuterated dimethyl sulfoxide ((CD3)2SO, 2206-27-1, Sigma-Aldrich).

These samples were then transferred to specific tubes for analysis, from which the spectra were derived. Spectra were processed using the MestreNova software.

The degree of methacrylation is defined as the percentage of -OH groups on PVA chain which underwent reaction with GMA, bonding one methacrylic group. This value corresponds to the number of methacrylic groups present each 100 repetitive units on the chain.

The H-NMR spectra of PVA dissolved in DMSO-d6 show the three separate signals at 4.6, 4.4, and 4.2 ppm which are assigned to proton in (-OH) group of PVA. [168]

Protons belonging to the methyl group in the methacrylic pendants show a peak at 1.86 ppm. In addition, two multiplet signals in the ranges 2.629-2.638 ppm and 2.759 - 2.777 ppm correspond to the two protons of the -CH2 group in the epoxy ring. [167]

The presence of such peaks would correspond to the presence of residual GMA or reaction by-products.

The degree of substitution can be calculated by integrating aforementioned peaks and comparing their intensities. Existing three protons in each methyl groups, the intensity of the corresponding peak has to be divided by 3. Eq. 6 was used.

$$DM[\%] = \frac{\frac{I_{1.86}}{3}}{I_{OH} + \frac{I_{1.86}}{3}} \cdot 100 \qquad 6$$

7.5.3. Rheological tests

Suitable rheological properties are fundamental for both extrusion process and the behaviour of the printed filament deposited on the plate. A rotational rheometer, Discovery HR-2 by TA Instruments, was used for oscillatory rheological tests. The configuration used in this case is the plate-plate (20mm diameter plates). Three different tests were investigated: frequency sweep test; amplitude sweep test; three interval thixotropy test.

The first one has been chosen since at high shear deformations the samples with high filler content escaped the plates. Therefore, for the evaluation of viscosity, a flow rheology test was not possible. Complex viscosity is measured as the oscillation frequency varies and thus the shear rate. The frequency interval of the test is 0.01÷100 Hz and the amplitude of oscillation is 1%. Furthermore, a flow sweep test was performed only for SR349+silica formulations. It determines the shear deformation dependence of viscosity through a rotational test that measure the latter, applying an increasing shear deformation. The last was increased from 0.01 to 1000 s^{-1}.

The amplitude sweep test provides a sweep of increasing shear amplitudes at a constant frequency, implying an increasing shear rate and measuring storage and loss moduli. It is important to determine the crosspoint between G' and G'', which indicates the onset of flow. The stress corresponding to this onset is the yield stress, while the corresponding strain is the yield strain. The yield stress is a crucial parameter for DIW since it ensures shape retention after extrusion. The shear deformation range is 0÷100%.

The last test was performed in oscillatory mode applying three consecutive steps with different shear deformation: (I) 1%; (II) high shear deformation (100%) above the flow point; (III) again 1%. The test simulates printing: the first interval simulates the material in the cartridge (stationary); the second interval simulates extrusion, then large deformations; the third interval simulates the material on the plate (again stationary). Conservative and dissipative modulus are measured, G’ and G’’ respectively. In the first period, G'>G'' because the material has a solid-like behavior (in case this does not happen, the material is not printable). In the second period, G'<G'' because we are going beyond the viscous flow onset. In this regime, the material is liquid-like. If G' returns immediately above G'' in the third period, Shape retention is

ensured because it means that the material comes back to a solid-like state right after extrusion. The duration of the three intervals has been set to 300s each. All tests were carried out at 25°C. [61]

7.5.4. Printability tests

To understand the printability and shape fidelity of materials we took advantage of three different tests [169]: (I) filament uniformity; (II) filament fusion; (III) pore geometry/visual grid. Uniform inks will produce desired uninterrupted extrusion. On the other hand, when inks contain particles or clusters that cause unevenness, the irregularities in extrusion force that arise over time can diminish the reliability of the deposited filaments.

Uniformity and shape fidelity can be investigated when a continuous filament is extruded. So, it's very important to have a homogeneous filament diameter during the whole printing process, that guarantees a planar structure. The considered parameter is d_i. Figure 34 illustrates the test.

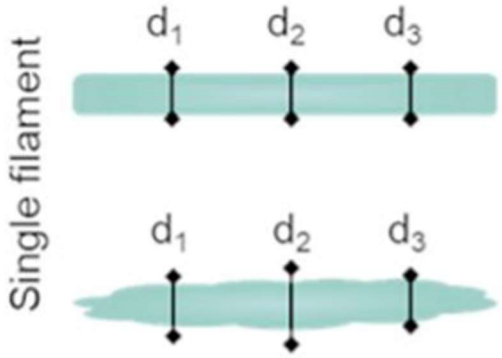

Figure 34: Graphical representation of filament uniformity test.

Eq. 7 was used to explain the filament uniformity, where d_i and d_{av} are respectively the measured and average diameter.

$$U = \frac{\sum_{i=1}^{N} |d_i - d_{av}|}{N} \qquad 7$$

In the second test, Figure 35, we evaluated the merger of adjacent filaments due to the surface tension between the printed material and the collector substrate. Lower is the yield stress, longer is the length of fused segments with a consequently lower resolution in x-y plane. Filament distances f_d, that decreases during the test and it's proportional to the nozzle diameter; fused segment length f_s; filament thickness f_t are the parameters taken into account.

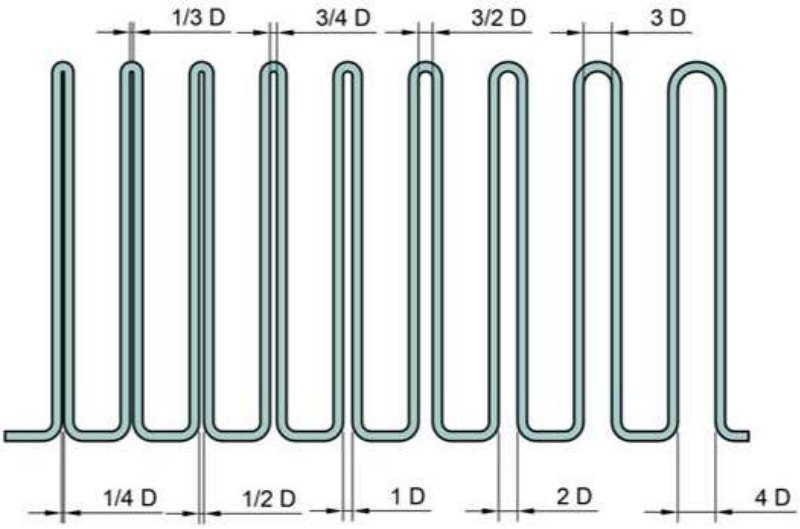

Figure 35: Graphical representation of filament fusion test.

The ratio between the fused filament length and the filament thickness is the evaluation parameter linked to the filament distance. The ideal value of the ratio is 1 and indicates that all filaments are distinguished. The closer we get to this value and the higher is the number of distances interested, the higher is the printability and stability of the material post-extrusion.

The last test evaluates the geometrical accuracy of cross filaments, in Figure 36. The printability index P_r is used, Eq. 8, based on area and perimeter of the pores with an ideal 0-90° laydown pattern.

$$P_r = \frac{l^2}{16A} \qquad 8$$

Where l is the perimeter and A is the area. The ideal value is 1. It indicates the perfect geometry square pores and filament merger. When it's higher than 1, the printed filaments are discontinuous with a nonlinear print direction, given an irregular shape; when it's lower than 1, the pores' shape is rounder. These deviations from the ideal value could be related to the nonoptimal gelation condition or to the low viscosity of the material and the consequently low post-extrusion stability. [169]

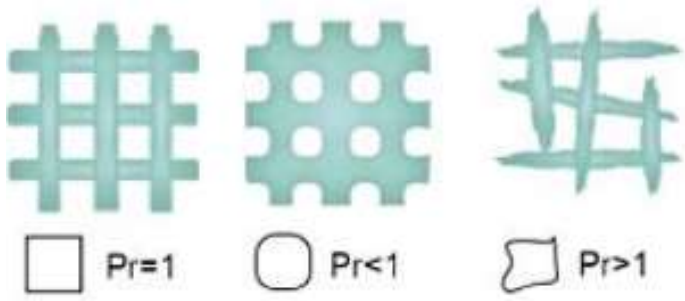

Figure 36: Graphical representation of grid test.

All measurements were taken with the help of software ImageJ software (National Institutes of Health, US).

7.5.5. Gel content

ASTM standard test method D2765-16 (2016) [170] was followed to evaluate the gel content of the samples, that is the percentage of crosslinked monomers after curing. Test method C was followed in this case. Samples were immersed in a liquid acting as a solvent for the monomer, acetone for SR349 and distilled water for PVA, for 24 hours on a magnetic stirrer (with a proportion of 300mL for 2g of sample). With the help of a paper filter (Whatman Filter Papers, Cat No 1001 125), not solubilized residual particles were collected. All was put in a vacuum oven at 70°C until the complete evaporation of the acetone. Measured the mass before and after the tests of the samples, we calculated the gel content percentages followed the Eq. 9:

$$Gel\% = \left(1 - \frac{w_0 - w_f}{w_0}\right) \times 100 \qquad 9$$

Where w_0 is the starting mass of the samples and w_f is the final mass after the drying.

7.5.6. Ultraviolet light-differential scanning calorimetry (UV-DSC)

Ultraviolet light-differential scanning calorimetry (UV-DSC) is a specialized analytical technique that combines the principle of both UV spectroscopy and DSC. It was used to measure the reactivity of functional groups to UV light with the same machine and setup of DSC test, equipped with Lightningcure LC8, Hamamatsu Photonics, Japan. The heat exchange upon UV-irradiation at constant temperature is measured. The tests were performed exposing the samples for 15 minutes (time necessary to complete any phenomenon taking place during the analysis) at room temperature and 210.6 mW/cm² UV intensity (405 nm). Table 4 summarises the test, with samples analysed, goal, and parameters.

Table 4: Summary of samples analised, goal of the test, and parameters used.

DSC	Goal	Parameters
SRS15 **SRC10** **SRC10PC** **PVAS10** **PVAS10PC** **PVAS15** **PVAS15PC** **PVAS20** **PVAS20PC**	Investigate curing% through the enthalpy before and after curing of the samples	Intensity = 210.6 mW/cm² Time = 15 min

PVAC20
PVAC20PC

The Eq. 10 was used to understand the percentage of curing for SR349 samples:

$$1 - \frac{\frac{H_{PC}}{\frac{1}{1+X}}}{\frac{H}{\frac{1}{1+X}}} \qquad 10$$

where H and H_{PC} represent respectively the enthalpy of sample pre and post curing, 1 in the denominator represents the resin quantity, and X represents the filler percentage.

The Eq. 11 was used for PVA samples.

$$1 - \frac{\frac{H_{PC}}{\frac{1}{1+0.8+X}}}{\frac{H}{\frac{1}{1+0.8+X}}} \qquad 11$$

In this case the adding term 0.8 represents the glycerol fraction.

7.5.7. Differential scanning calorimetry (DSC)

Differential scanning calorimetry (DSC) is a thermal analysis method that imposes a thermal history and measures the heat exchange related to changes (whether physical, chemical, or kinetic) in materials. The material under analysis is weighted and deposited in an aluminium pan, while an additional container remains empty, serving as a point of reference. Both containers undergo a specific thermal profile, and by tracking the temporal shift in the heat disparity necessary to maintain the two containers at nearly the same temperature, it becomes feasible to generate a graph depicting specific heat in relation to temperature.

The outcome yields a DSC graph with both exothermic and endothermic peaks as well as points of inflection. This furnishes valuable qualitative and quantitative details, such as the melting point, glass transition temperature, and crosslinking enthalpy. DSC tests were performed following the ISO 11357-1:2023 [171].

In this study, differential scanning calorimeter DSC/823e (MettlerToledo, Columbus, OH, USA), operating within a constant nitrogen flow, was used. The ramp temperature is from 25°C to 250°C with a 10°C/min heating rate. A summary of samples, goal, and parameters was done in Table 5.

Table 5: Summary of samples analised, goal of the test, and parameters used.

DSC	Goal	Parameters
SRS15PC **SRC10** **SRC10PC** **SRC15** **SRC15PC** **SRC20** **SRC20PC** **PVAS10PC** **PVAS15PC** **PVAS20PC** **PVAC20** **PVAC20PC** **PVAC25** **PVAC25PC** **PVAC30** **PVAC30PC**	Investigate T_g and the curing% through the enthalpy before and after curing of the samples	T_{range} = 25÷250 °C Rate = 10 °C/min

The formulas used for the calculation of percentage of curing in DSC test are the same previously described.

7.5.8. Uniaxial tensile test

Uniaxial tensile testing is a mechanical examination in which a specimen is exposed to deliberate unidirectional tension until it reaches a point of failure. This testing procedure yields stress-strain plots, from which key parameters are derived, including Young's modulus (E), ultimate tensile strength (σ_b), the elongation at break (ε_b), and the toughness (k). To understand mechanical properties of the different samples, Zwick Roell Z010, ZwickRoell GmbH & Co. KG, Germany, equipped with a 10 kN cell load, diagonally milled metallic clamps of 8354 type and extensometers, has been used. A preload of 5N was used at a speed of 0.025 mm/s for all samples. The test speed increased from 1 mm/min, in the case of SR349, to 10 mm/min, in the case of PVA.

The Young's modulus was determined as the slope of the line interpolating the stress-strain curve in a strain interval ranging between 0.05% and 0.25%. The elongation at the point of rupture (expressed as a percentage) was computed by measuring the extension (i.e., the change in gauge length) at the specimen's breaking point, dividing it by the original gauge length, and then multiplying the result by 100. For ductile polymers, the maximum stress (in MPa) or for brittle materials, the strength at the point of rupture (in MPa) was determined by dividing the maximum load or break

load by the average initial cross-sectional area of the gauge length. Thoughness is calculated as the integral of stress-sterin curve until failure point (MPa).

In every mechanical test, in SR cases, the dumbbell-shaped sample was secured between two clamps and subjected to controlled unidirectional stretching until reaching failure, at which juncture the testing apparatus automatically halted. Additionally, an extensometer was employed to accurately measure the elongation of the gauge length of the test specimen as the specimen underwent elongation.

7.5.8.1. 3D specimens

7.5.8.1.1. SR349

The tests were carried out following the ASTM standard test method D638 [172] for both 3D printed and cast specimens, as regard the SR. The specimen used in this case is the type 1 with dumbbell form, represented in Figure 37. The chosen filling pattern for all specimens is 'straight aligned' in the longitudinal direction with respect to the applied test load.

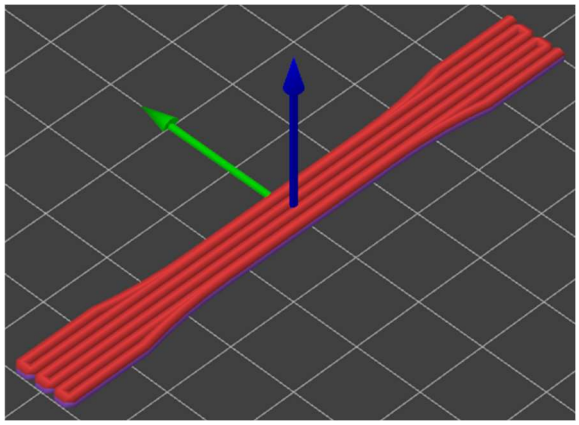

Figure 37: SR349 dumbbell sample for 3D printing.

Specifical dimensions are described in Table 6.

Table 6: SR349 dumbbell sample main dimensions.

Sample	Overall length [mm]	Gage length [mm]	Width [mm]	Thickness [mm]
SRS15 **SRC10** **SRC15** **SRC20**	80	24.24	9.21	1.55

Printing details are shown in Table 7. LED curing time is referred to the curing time for each printed layer. UV lamp curing time is referred to the curing time for each sample side.

Table 7: SR349 dumbbell sample main printing parameters.

Sample	Nozzle diameter [mm]	Layer thickness [mm]	Printed speed [mm/s]	LED curing time [s]	UV lamp curing time [min]
SRS15	0.41	0.2	10	1	10/20
SRC10	1.6	0.8	5	60	20
SRC15	1.6	0.8	5	60	20
SRC20	1.6	0.8	5	60	20

SRCX, after the UV lamp treatment, were thermal cured in oven at 140 °C for 2h.

7.5.8.1.2. PVA

In PVA case, tests follow ASTM standard test method D3039/D3039M–17 (2017) [173] for the specimens form (used for flexible materials). Figure 38 shows the specimens printed for the tests. Also in this case, filling pattern is 'straight aligned' in the longitudinal direction with respect to the applied load. Table 8 described specimens' details.

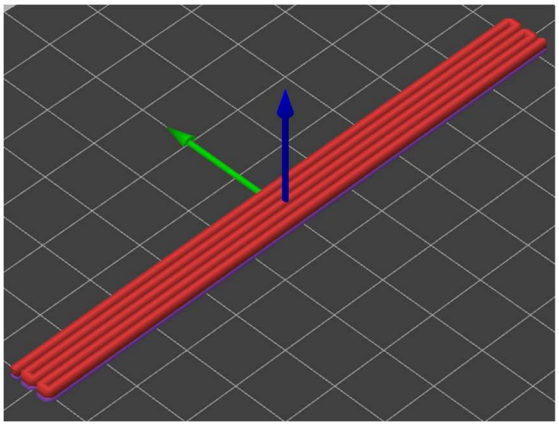

Figure 38: PVA rectangular sample for 3D printing.

Table 8: PVA rectangular sample main dimensions.

Sample	Overall length [mm]	Width [mm]	Thickness [mm]
PVAS15 **PVAC20** **PVAC25** **PVAC30**	103.13	8.13	2.40

Printing details are shown in Table 9. PVAS15 was used to understand matrix behaviour, so just cast samples were analysed.

Table 9: PVA rectangular sample main printing parameters.

Sample	Nozzle diameter [mm]	Layer thickness [mm]	Printed speed [mm/s]	LED curing time [s]	UV lamp curing time [min]
PVAS15	-	-	-	-	20
PVAC20	1.6	0.8	5	60	20
PVAC25	1.6	0.8	5	60	20
PVAC30	1.6	0.8	1	60	20

PVA samples were dried for 24h at 50 °C in oven. In leather cases, they were then thermally cured at 120 °C for 2h.

All the three-dimensional printed specimens were manually polished to eliminate typical roughness because of three-dimensional printing manufacturing.

8 Results

The utilization of UV-assisted three-dimensional printing techniques allows for the controlled extrusion of light-curable inks featuring diverse formulations and mechanical properties, achieved by adjusting the operational variables. Nonetheless, this investigation conducted a series of trials to assess the most suitable parameters for the three-dimensional printing of mixtures containing varying levels of reclaimed leather and exhibiting different rheological characteristics. A first study of silica+matrix was conducted to better understand the properties and the behaviour of the latter.

8.1. LCA

A comparative Life Cycle Assessment (LCA) was conducted, contrasting leather against a composite material comprising acrylic resin, as the representative matrix, and leather waste. The LCA analysis draws upon literature sources [173], [174]. The chosen life cycle impact assessment method is ReCiPe Midpoint (H). Two impact categories, namely Climate change (kg CO_2 eq) and Acidification (kg SO_2 eq), were selected. The assessment comprehensively considers the production, distribution, and disposal stages within each impact category.

Table 10 summarizes the environmental impact comparing 1 kg of virgin leather, recycled leather, raw hides and acrylic resin.

Table 10: LCA analysis comparison on selected materials.

Parameters	Virgin leather	Acrylic resin	Recycled leather	Raw hides
Climate change [kg CO_2 eq]	11.51	4.35	1.56	1.07
Acidification [kg SO_2 eq]	0.42	0.04	0.03	0.03

Recycled leather includes in its value raw hides and leather waste impacts. In the following graphs, Figure 39 and Figure 40, a comparison of virgin and recycled leather as a function of the composite composition is done for both parameters.

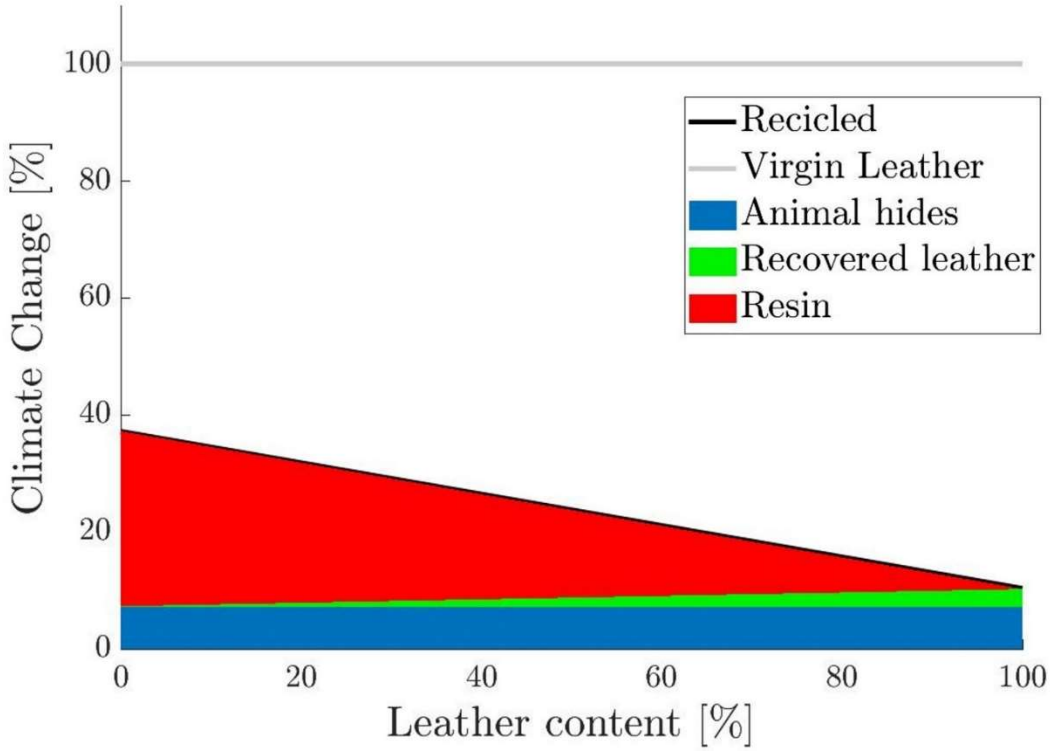

Figure 39: Climate Change comparison between virgin and recycled leather.

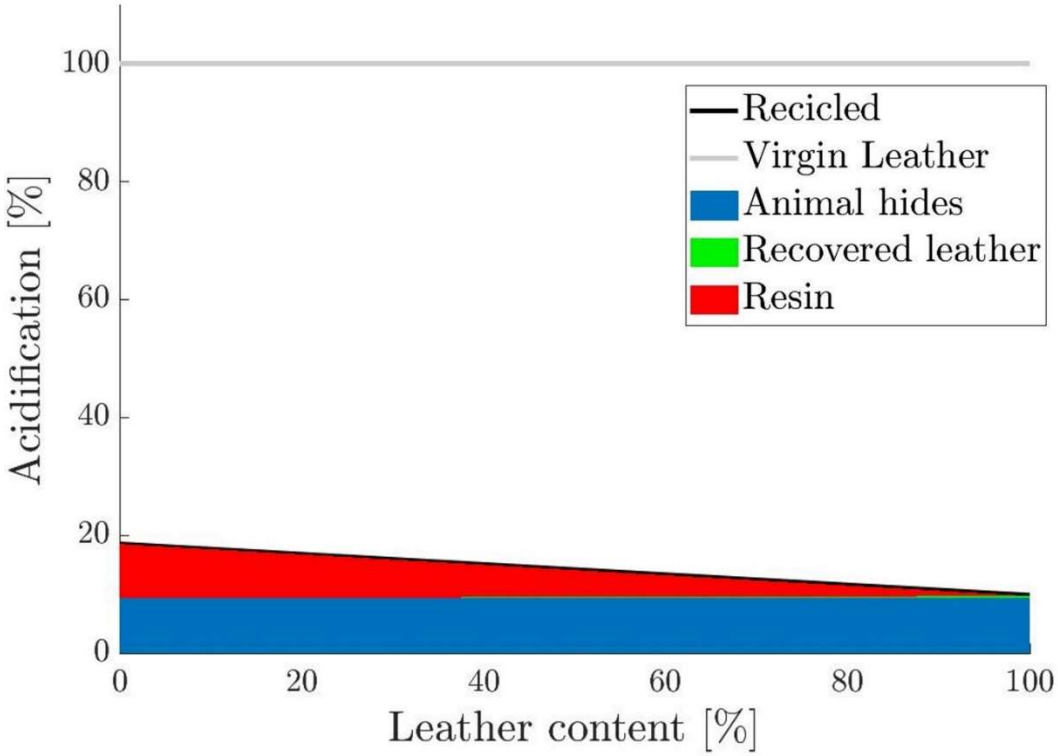

Figure 40: Acidification comparison between virgin and recycled leather.

It's clear the differences between the virgin leather (100% of environmental impact) and the recycled leather, in which the curve values decrease for higher concentration of the latter (and lower of resin consequently).

This scenario has two important consequences: on the one hand the production of leather products from virgin leather decreases, but, as a result, the amount of non-processed raw hides increases, accordingly with the increasing of disposal by incineration and landfill.

8.2. Filler dimensional characterization

50 photos of the sieved and non-sieved leather were analysed with 50X lens. Eq. 5 described the ratio between filler area and circle area to investigate the shape of fillers. Parameter goes to 1 when the filler is spherical, it goes to 0 when filler is filamentous.

$$P = \frac{A_{filler}}{A_{circle}} \qquad 5$$

Table 11 shows results of average P, A_{filler}, A_{circle}, and d_{av} values and standard deviation (σ). d_{av} is the average circle diameter, and, the characteristic dimension of the filler, was defined as that value. Such a low value well describes what you see in the pictures, i.e. elongated, filamentous fibres.

Table 11: Average results (and standard deviations) of P, filler area, circle area, diameter filler.

	P (σ)	**A_{filler} [mm²] (σ)**	**A_{circle} [mm²] (σ)**	**d_{av} [mm] (σ)**
Non-sieved leather	0.312 (0.126)	0.138 (0.136)	0.513 (0.493)	0.720 (0.370)
Sieved leather	0.375 (0.124)	0.107 (0.112)	0.341 (0.441)	0.574 (0.327)

The morphology appears to be very variable, as shown in Figure 41 and Figure 42, but still made up of coils of microfibres, which are fibrous, elongated and branched. Figure 43 and Figure 44 represent respectively non-sieved and sieved leather photos.

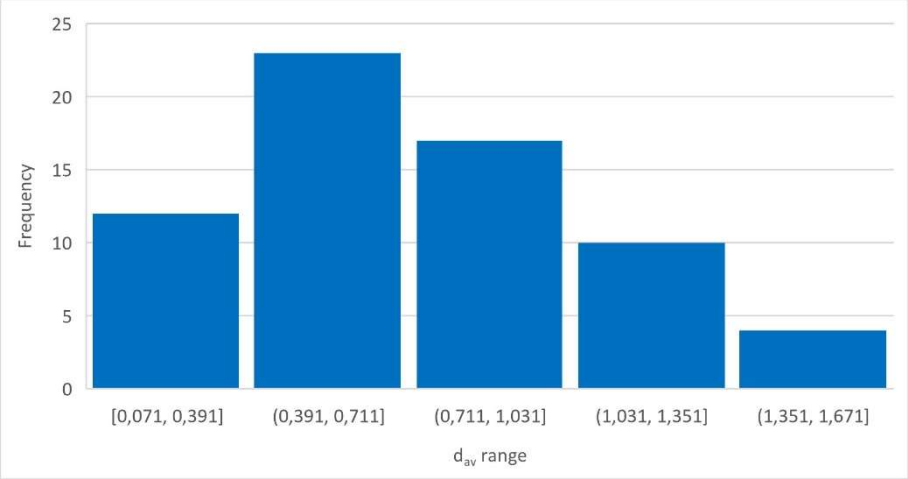

Figure 41: Range distributions of non-sieved leather.

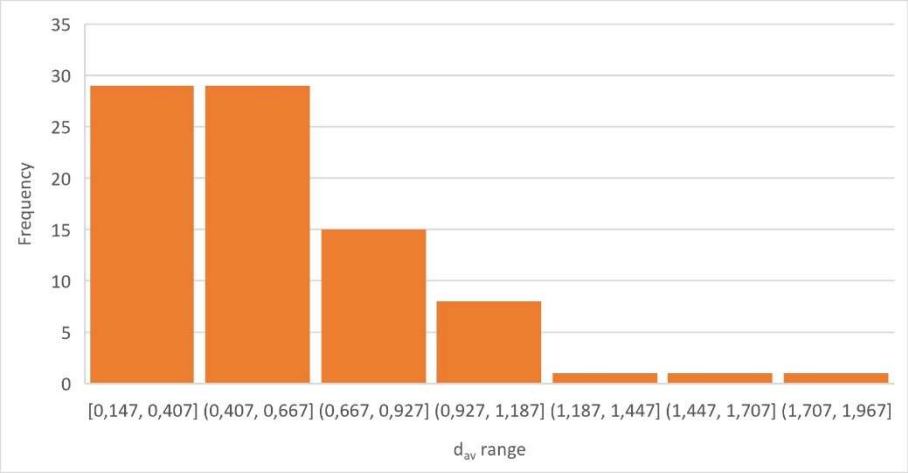

Figure 42: Range distribution of sieved leather.

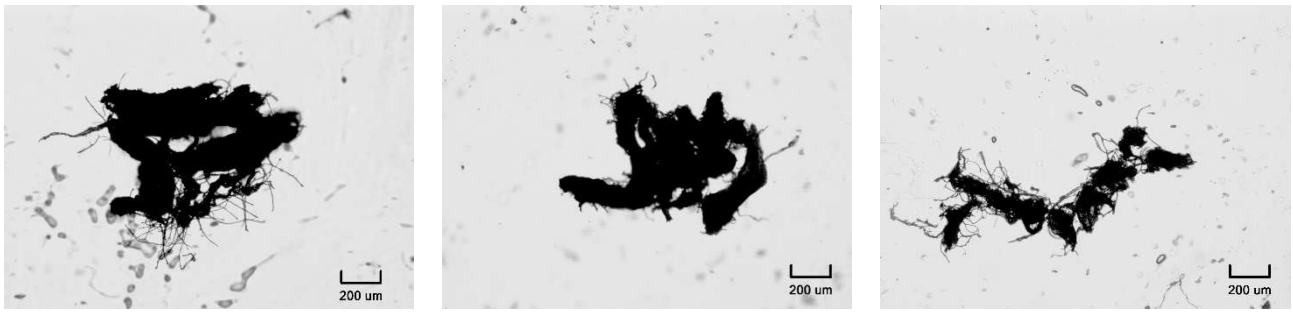

Figure 43: Non-sieved leather filaments.

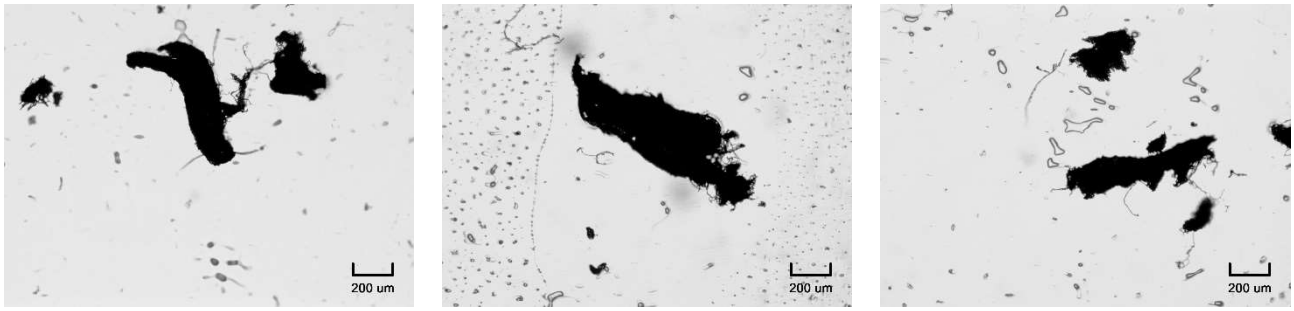

Figure 44: Sieved leather filaments.

8.3. Characterization of PVA Methacrylation

Figure 45 shows H-NMR spectra of PVA and PVAM. The high-intensity signal of the solvent ((CD3)2SO) in both spectra is located at 3.3 ppm.

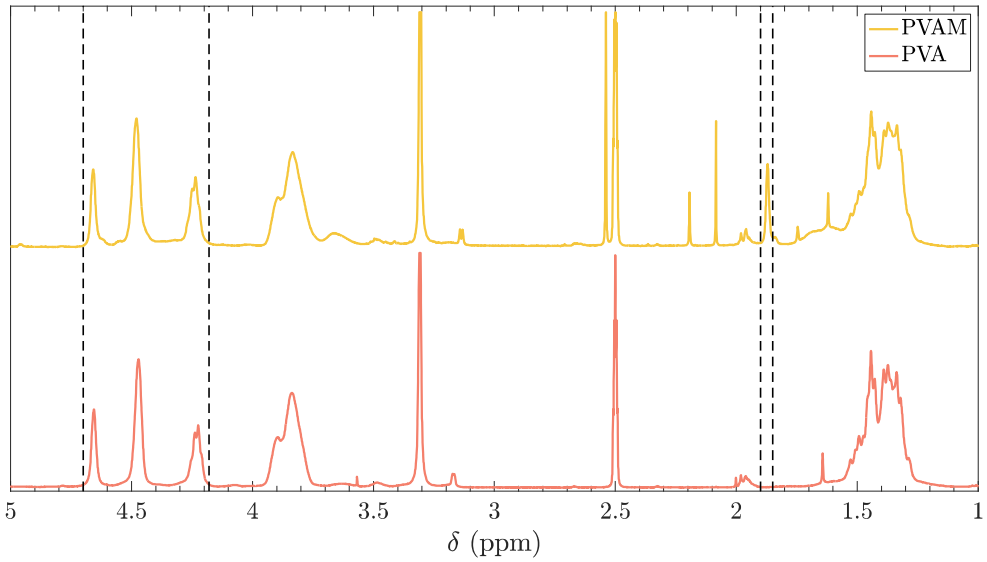

Figure 45: H-NMR spectra of PVA and PVAM.

In the PVAM spectrum, the peak relative to protons belonging to the methyl group in the methacrylic pendants is visible at 1.9 ppm. This peak is not present in the PVA spectrum, confirming methacrylation. In the range between 4.2 and 4.4 ppm, three peaks corresponding to protons in –OH groups are visible in both spectra.

To quantify the reaction's effectiveness, the degree of substitution (or methacrylation, DM) of the synthesized PVAM was calculated used the Eq. 6 applied to PVAM spectrum:

$$DM[\%] = \frac{\frac{I_{1.86}}{3}}{I_{OH} + \frac{I_{1.86}}{3}} \cdot 100 = 4.46\% \qquad 6$$

In order to perform the methacrylation reaction, glycidyl methacrylate has been added in a quantity equal to 5% mol/mol OH. Therefore, the maximum DM achievable is 5%. Having a DM equal to 4.46% indicates a reaction yield equal to 89%.

The absence of peaks in the ranges 2.629-2.638 ppm and 2.759 -2.777 ppm indicates that no residual GMA or reaction by-products are present in the polymer. Therefore, acetone washings following the methacrylation properly removed any contaminant.

8.4. SR349 Results

8.4.1. SR349 + Silica Results

8.4.1.1. Rheological tests

Different formulations were tested. Three percentages of silica were characterized: 0, 5, 10, 15 and 20 % w/w with respect to the matrix. Rheological tests were performed to assess the behaviour of the inks, whether Newtonian or pseudoplastic. Flow sweep test gives this information. In Figure 46 is represented the curves behaviors.

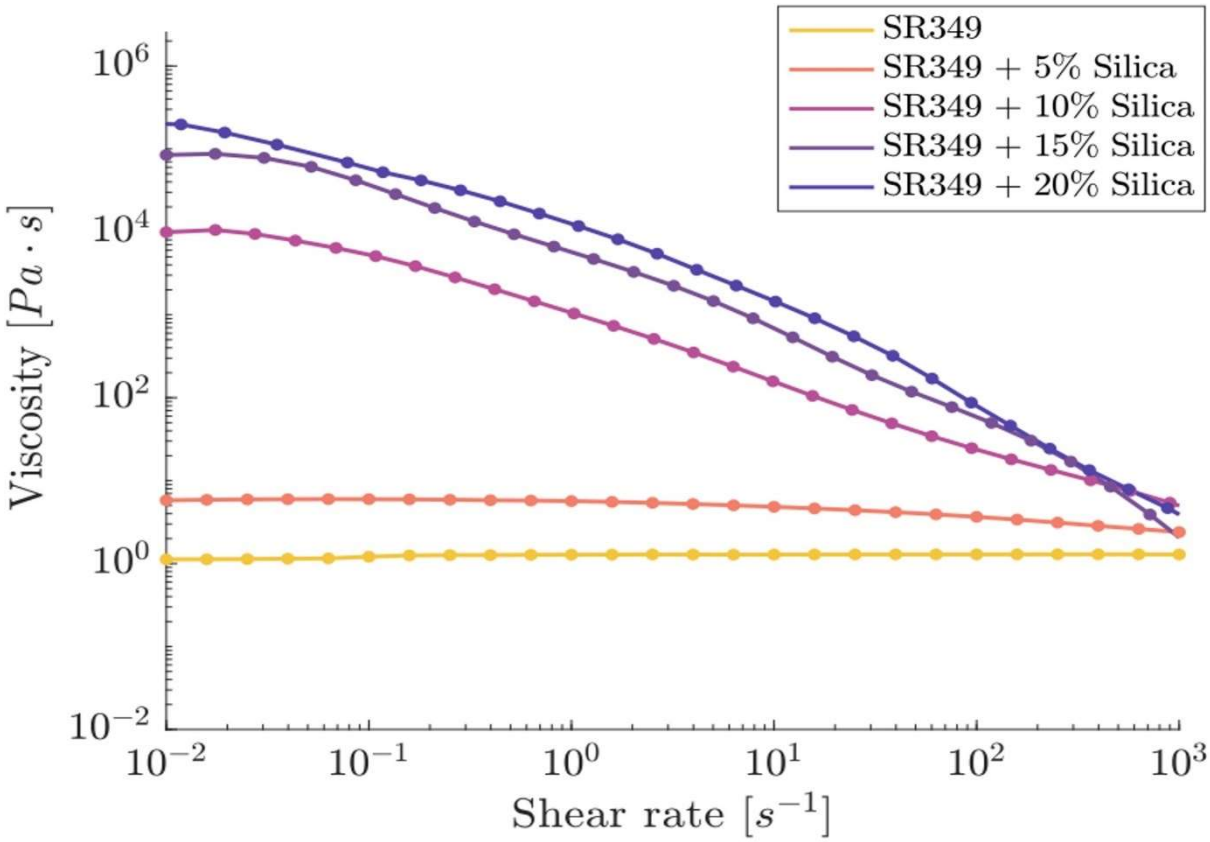

Figure 46: Flow sweep test of SR349+Silica formulations.

Frequency sweep test is then performed, allowing to assess the pseudoplasticity of the formulation. In this oscillatory test, an increasing frequency has been imposed and complex viscosity has been measured. The frequency interval of the test is 0.01÷100 Hz and the amplitude of oscillation is 1%. Results are represented in Figure 47, where SRS10, SRS15, and SRS20 show a pseudoplastic behaviour, so suitable to the three-dimensional printing. Consistent with the expectation, formulations with increasing silica content show increasing viscosity throughout the analysed frequency range.

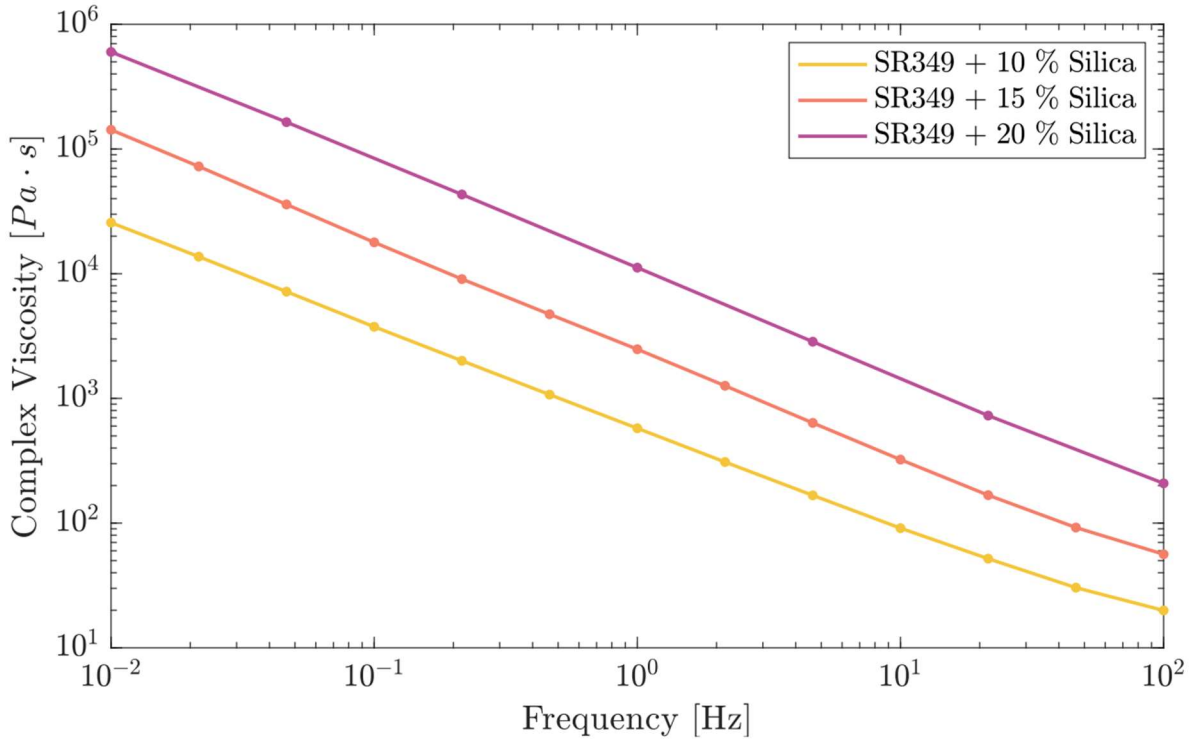

Figure 47: Frequency sweep test of SR349+Silica formulations.

The amplitude sweep test is an oscillatory rheology test that involves the imposition of increasing shear amplitudes while maintaining a constant frequency, resulting in an escalating shear rate. This process allows the measurement of storage and loss moduli. Identifying the intersection point between G' and G'' is crucial, as it corresponds to the initiation of flow. The stress corresponding to this initiation is termed the yield stress, and the strain associated with it is known as the yield strain. The range of shear deformation during this test spans from 0% to 100%. Figure 48 shows how the crosspoint increases at higher silica content. [61][61]

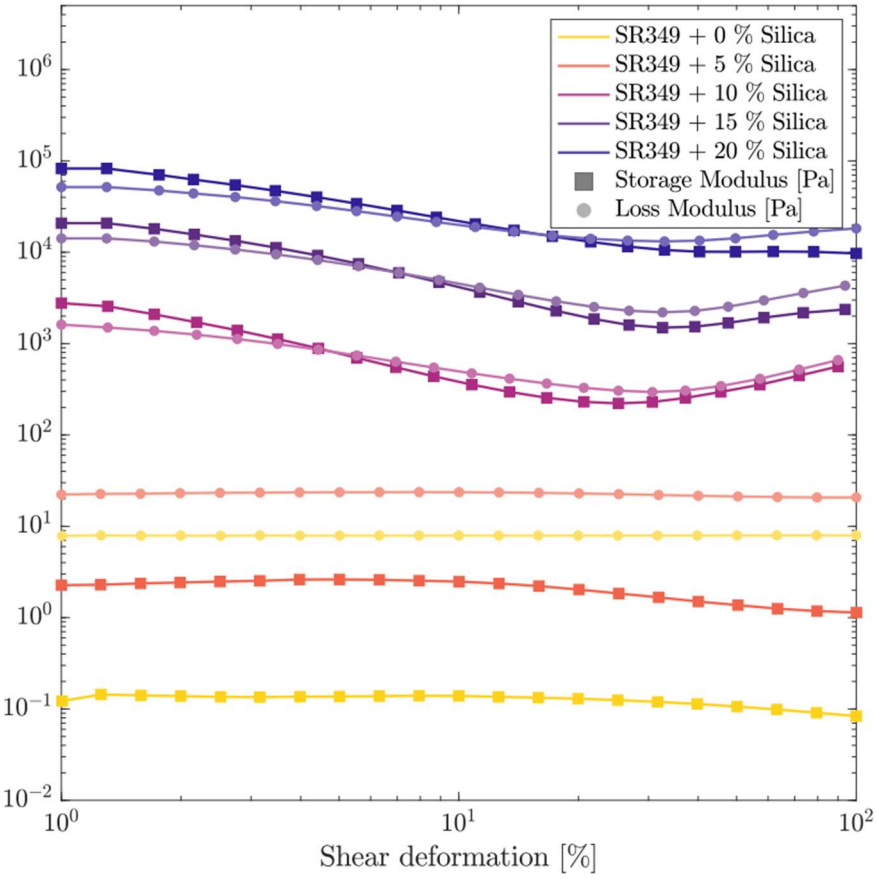

Figure 48: Amplitude sweep test of SR349+Silica formulations.

From this second test, yield stress and yield strain are extrapolated, as reported in Figure 49, that correspond to the crosspoints. Also here, higher silica content, higher yield stress and strain values, so higher pressure to extrude the material. Infine, a very limited linear viscoelastic region (deformation range in which storage modulus is constant) is visible. Samples at 0 and 5 % show no zones of solid-like behavior. The value of 8030 Pa of yield stress for 20% is very high, one begins to perceive that it may not be printable.

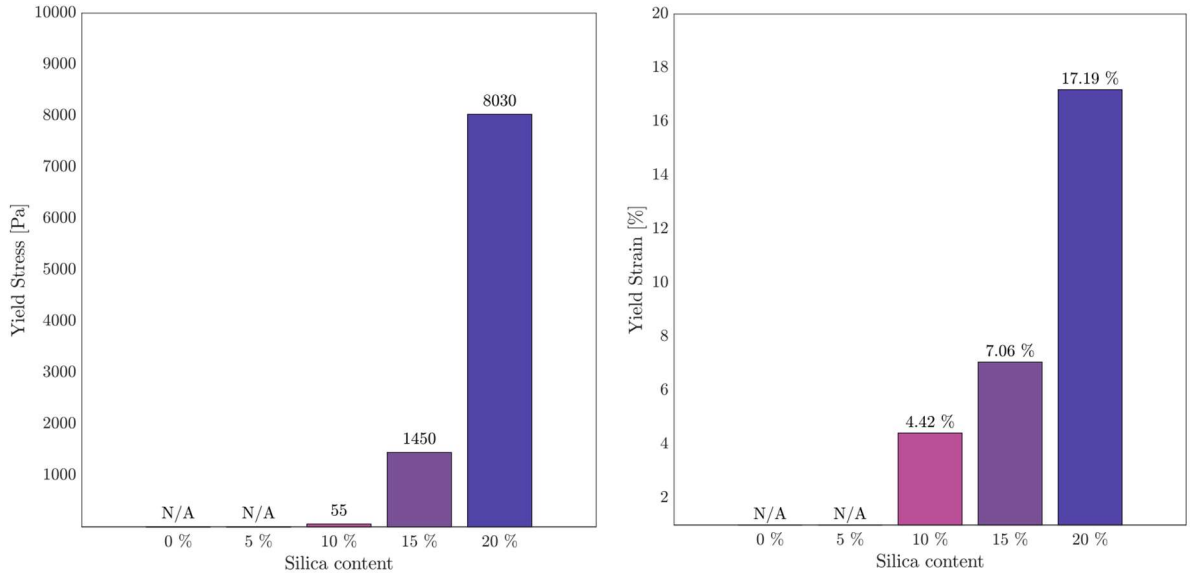

(a) Yield stress. (b) Yield strain.

Figure 49: Yield stress (a) and Yield strain (b) values of different SR349+Silica formulations.

The thixotropy test involves three sequential steps: (I) applying 1% shear deformation to simulate material in a cartridge; (II) subjecting the material to high shear deformation (100%) to simulate extrusion; (III) applying 1% shear deformation to simulate material on the printing plate. The frequency is 1 Hz for the three steps. Conservative (G') and dissipative (G'') moduli are measured as a function of time. Initially, G' > G'' showing a solid-like behaviour for small deformations and therefore the presence of a yield point. This result is coherent with what found in the amplitude sweep test: yield deformation is higher than 1% for the three compositions and therefore solid-like behaviour was expected for this level of stimulus. During extrusion, G' < G'', indicating a liquid-like state. This shows how the flow onset is possible for higher force applied. This way, the material is extrudable. A quick return of G' above G'' post-extrusion is favourable, suggesting That the material can return to a solid-like behaviour after being extruded. The duration of each step is 300 s. The duration of the extrusion though the nozzle is in reality much faster. Therefore, it can be supposed that, being the duration of large deformation much smaller, the extent of thixotropy would be much lower during actual extrusion. Therefore, the materials are expected to come back to solid-like behaviour in a faster way than they did in the current test. Results are represented in Figure 50. At higher silica content, the crosspoint time decreases, indicating a quicker self-sustaining. Finally, higher values of moduli are observed in the three steps for higher silica contents, coherently with previous characterizations and with what expected.

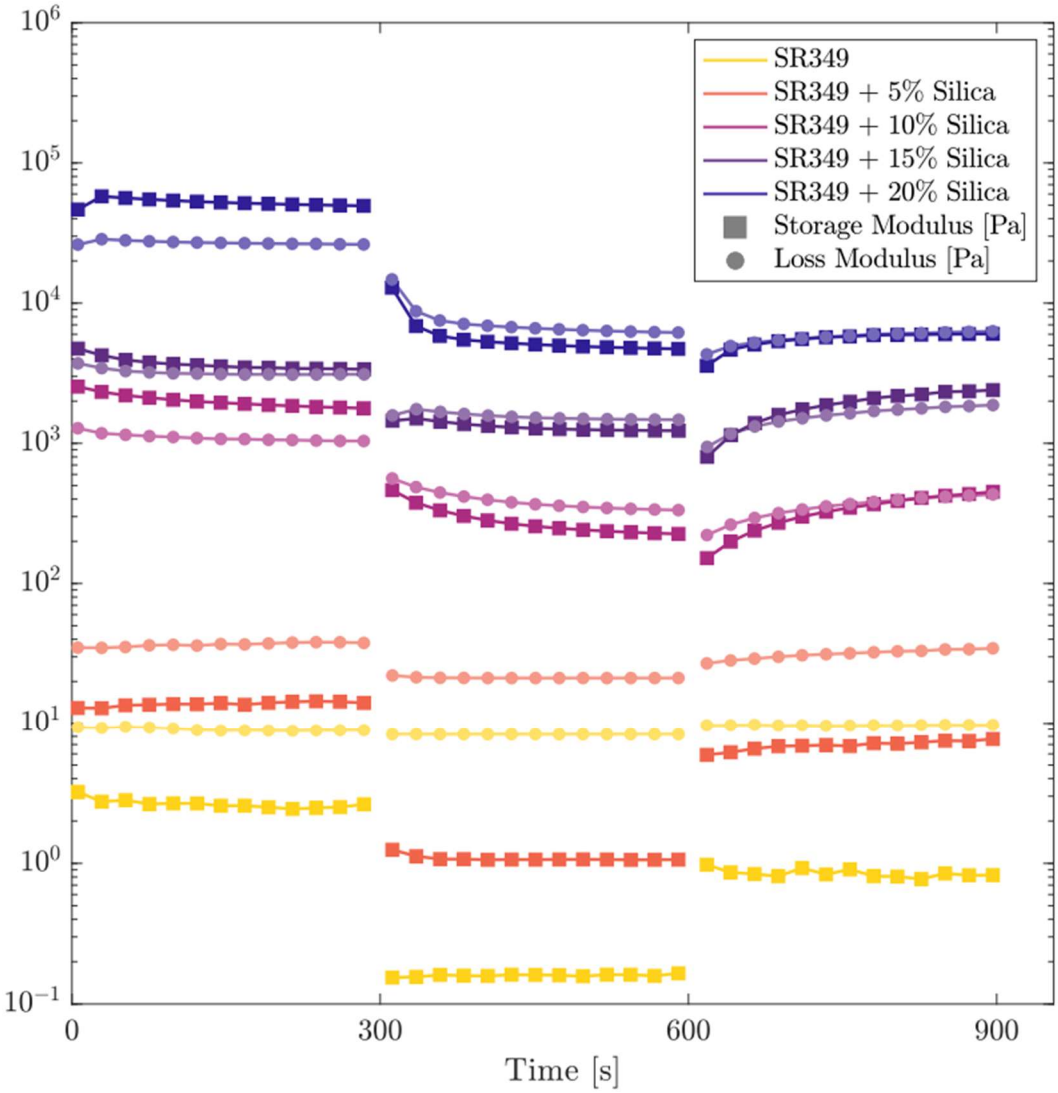

Figure 50: Thixotropy test of SR349+Silica formulations.

8.4.1.2. Printability tests

To understand the best ink for the three-dimensional printing process, printing tests were done for all formulations except for the 20% w/w due to the printing process problems of too high viscosity and impossibility of extrusion, aalready expected as a result of the amplitude sweep test, as reported in Figure 51, and 0% w/w which, lacking viscosity and thus its own post-extrusion stability, was unable to recreate the test.

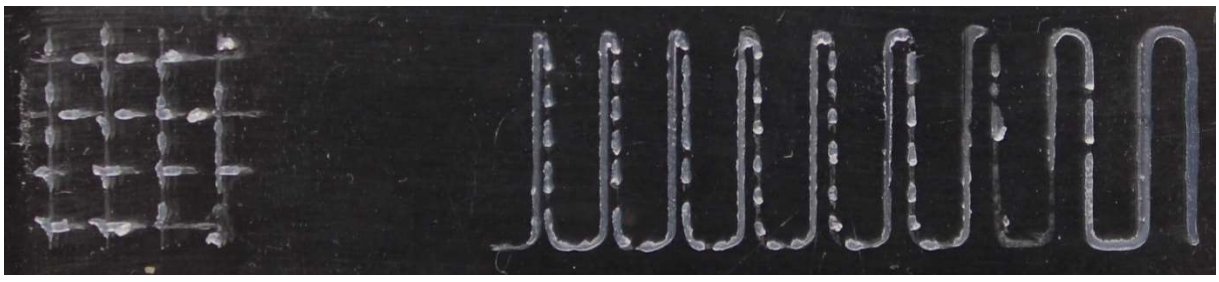

Figure 51: Printability tests of SRS20.

Starting from the filament uniformity, in Figure 52 are reported all results. Taken the average diameter of the printed filament as the reference parameter, the uniformity was calculated. Eq. 7 was used for the test.

$$U = \frac{\sum_{i=1}^{N} |d_i - d_{av}|}{N} \qquad 7$$

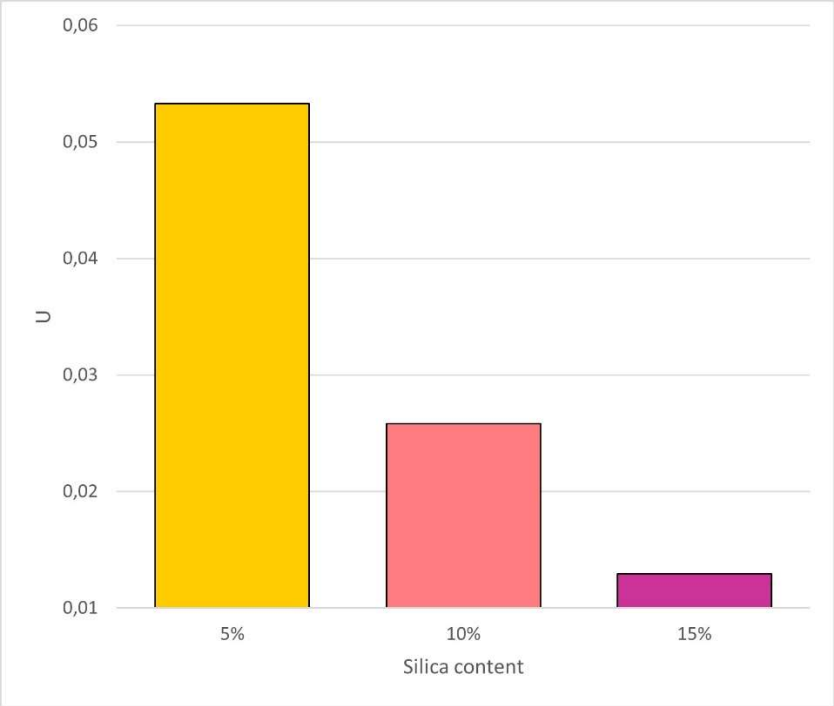

Figure 52: Filament uniformity test of SRSX.

It's evident the difference between formulations. SRS15 shows a very low value parameter, meaning that the ink is very stable after the extrusion, unlike SRS5, that presents a high value.

Filament fusion test, in Figure 53, is another printability test evaluation. Decreasing the distance between filaments, the ability of them to be steady can be understood. Filament distances f_d, that decreases during the test and it's proportional to the nozzle diameter; fused segment length f_s; filament thickness f_t are the parameters taken into account. Also here, higher the silica content, higher is the number of distinguishing filaments.

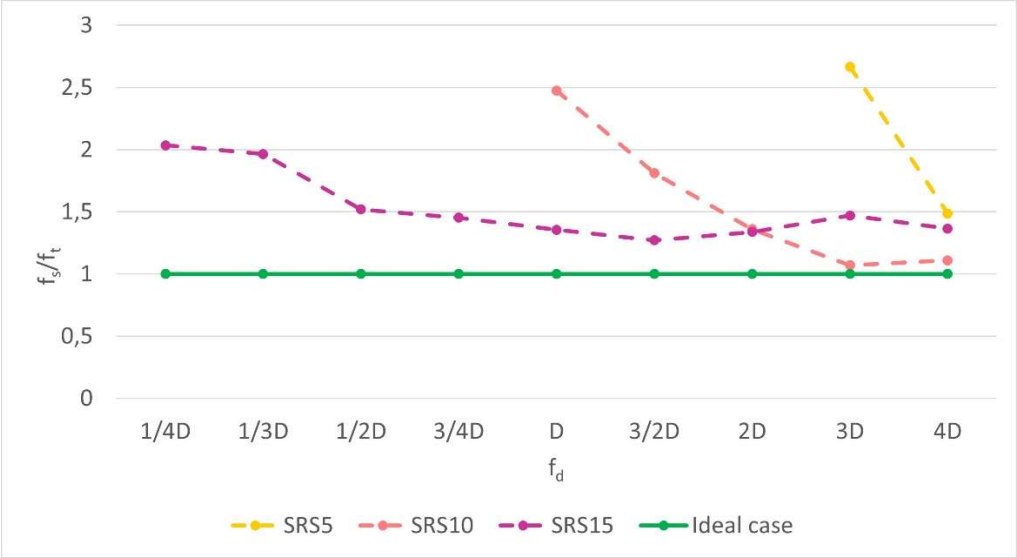

Figure 53: Filament fusion test of SRSX.

Path distances are proportional to the nozzle diameter. SRS5 has only two points due to the fact that only two filaments remained distinguishable, while all the other ones fused. The same reasoning can be made for SRS10, meanwhile, SRS15 is the only one that has no fused filaments and the most constant fused segment length f_s/f_t ratio, indicating a more uniform printing. Being the ratio always very close to 1, the material exhibited a good ability to produce small features with a good fidelity.

In the last test, the grid view, through the printing index P_r of Eq. 8, stability and printability is evaluated. Figure 54 show the results of the different formulations.

$$P_r = \frac{l^2}{16A} \qquad 8$$

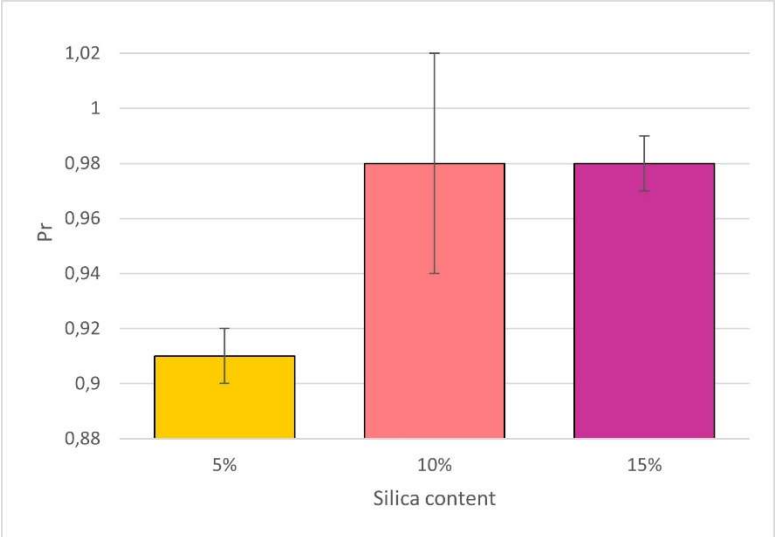

Figure 54: Grid test of SRSX.

Also in this case, SRS15 results the best one. The printability index of SRS10 and SRS15 are the same, but, in the first case, the error degree is higher, meaning that same pores are nonlinear. The Fig. X shows SRS15 grid.

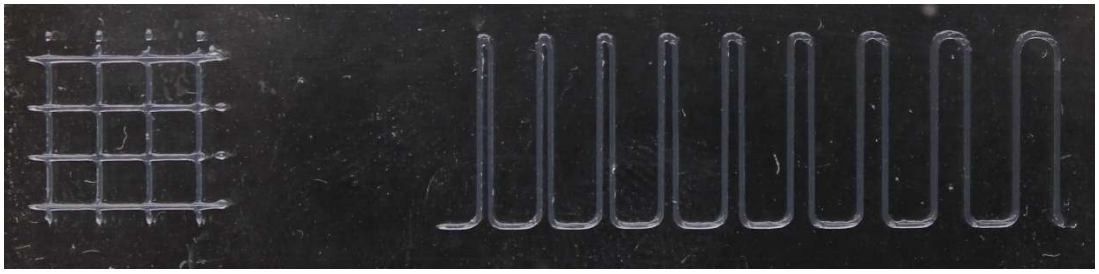

Figure 55: Printability tests of SRS15.

From this point forward, SRS15 was chosen as formulation representative of the matrix and used for further characterization thanks to the better results than the other formulations. So only it is considered for the remaining tests.

8.4.1.3. Gel content

To investigate gel content percentages of printed samples, Eq. 9 was used.

$$Gel\% = \left(1 - \frac{w_0 - w_f}{w_0}\right) \times 100 \qquad 9$$

A gel content below 100% suggests the existence of low molecular weight components, indicating the presence of incompletely reacted monomers. While these components may function as plasticizers, they can pose risks by diminishing mechanical strength and elastic modulus, inducing chemical and physical instability in the polymer. This instability may manifest as issues such as yellowing due to spontaneous and uncontrolled reactions over time. Additionally, these low molecular weight species may migrate to the polymer's surface, forming an adhesive layer.

Two different crosslinking time were evaluated: 10 or 20 minutes for each specimen side, using a UVA lamp.

Table 12 shows the results. At longer exposure time, the percentage of monomers crosslinked is higher, near the totality. Consequently, also the mechanical properties increase and the final material results more rigid.

Table 12: Gel content test results of SRS15.

Sample	Gel%
SRS15 10min UV	98.3
SRS15 20min UV	98.9

8.4.1.4. UV-DSC

The evaluation of reacted functional groups in the material, trough the UV light, was performed through the UV-DSC test at room temperature. The UV intensity is 210.6 mW/cm² and the duration of the test is 15 minutes. In the following Table 13 test results are repoted. Eq. 10 was used to calculate the curing percentages.

$$1 - \frac{\frac{H_{PC}}{\frac{1}{1+0.15}}}{\frac{H}{\frac{1}{1+0.15}}} \qquad 10$$

Table 13: UV-DSC test results of SRS15.

Sample	Curing%
SRS15 10min UV	85.3
SRS15 20min UV	96.7

A remarkable difference was observed in the two types of samples. Higher the curing time, higher the yield of the reaction. After 10 minutes, the crosslinking reaction is arleady at a good level of yield, but has to be continued to reach higher levels. It has to be noted thas a yield of 100% often correspond to material brittleness. In addition, sometimes it can be reached only with a processing which also degrades the material, causing yellowing and formation of volatile or harmful species. A yield slightly lower than 100% does not correspond to low molecular weight oligomer in the polymer. It corresponds to a completely formed network (in which all monomer molecules have been included in such network) in which some molecules retained unreacted groups. Therefore, a value of 96.7% does not indicate the presence of unreacted monomer (that can be harmful), but it is a completely acceptable value.

8.4.1.5. DSC

DSC tests were performed to know the glass transition temperature of the printed samples. The range temperature starts from 25°C and arrives at 250°C with a rate of 10°C/min. This manages to understand the transition of the material from glass to rubber phase. Two different UV lamp time was evaluated in this case. In Table 14 T_g are reported.

Table 14: DSC test results of SRS15.

Sample	T_g [°C]
SRS15 10min UV	49
SRS15 20min UV	52

Consistent with UV-DSC and gel content, there is a slightly higher T_g for the 20 minute crosslinked sample, hence a higher crosslinking density. The small difference between the two indicates that doubling the curing time does not result in such a significant increase in crosslinking density, indicating that already after 10 minutes the crosslinking reaction is well advanced.

8.4.1.6. Uniaxial tensile test

Mechanical behavior was investigated by means of uniaxial tensile testing on SRS15 specimens. Figure 56 shows the average curve trend of printed and cast specimens. In Table 15 and in Figure 57 the average (and standard deviation σ) values of elastic modulus, maximum tensile strength, elongation at break and toughness were summarized, comparing cast samples with printed samples.

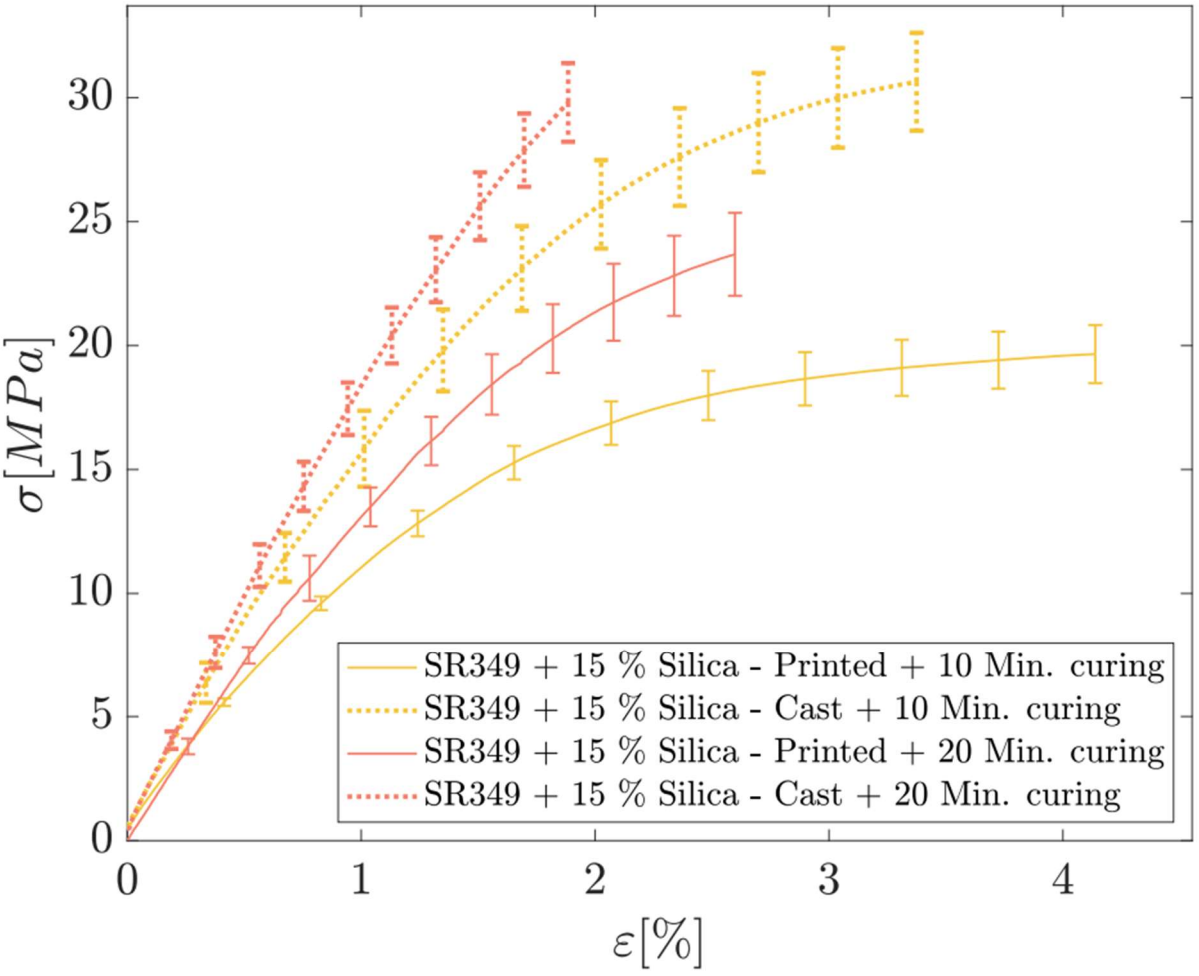

Figure 56: Mechanical test results of SRS15.

All mechanical properties depend on crosslinking time and there is also a difference between printed and casted specimens. A lower UV curing time means lower brittleness material with lower Young's moduli and stresses at break, but higher toughness and elongations at break. Also Printed specimens show more ductile behavior than casted one. This could be attributed to defects in the printed specimens,

or a strong anisotropic behavior of the specimens due to the printing strategy adopted. Modulus and strain at break are typical of cross-linked acrylic resins. Another value confirming that processing is sufficient to give complete crosslinking.

Table 15: Summary of mechanical properties of SRS15.

Sample	E [GPa] (σ)	σ_b [MPa] (σ)	ε_b [%] (σ)	k [MPa] (σ)
SRS15 – Printed + 10min UV	1.26 (0.062)	19.89 (0.964)	4.59 (0.502)	68.98 (6.643)
SRS15 – Cast + 10min UV	1.54 (0.099)	30.36 (1.705)	3.77 (0.295)	78.77 (11.754)
SRS15 – Printed + 20min UV	1.46 (0.100)	24.76 (2.635)	3.20 (0.659)	51.87 (19.656)
SRS15 – Cast + 20min UV	1.92 (0.255)	31.07 (2.464)	2.00 (0.164)	35.56 (5.661)

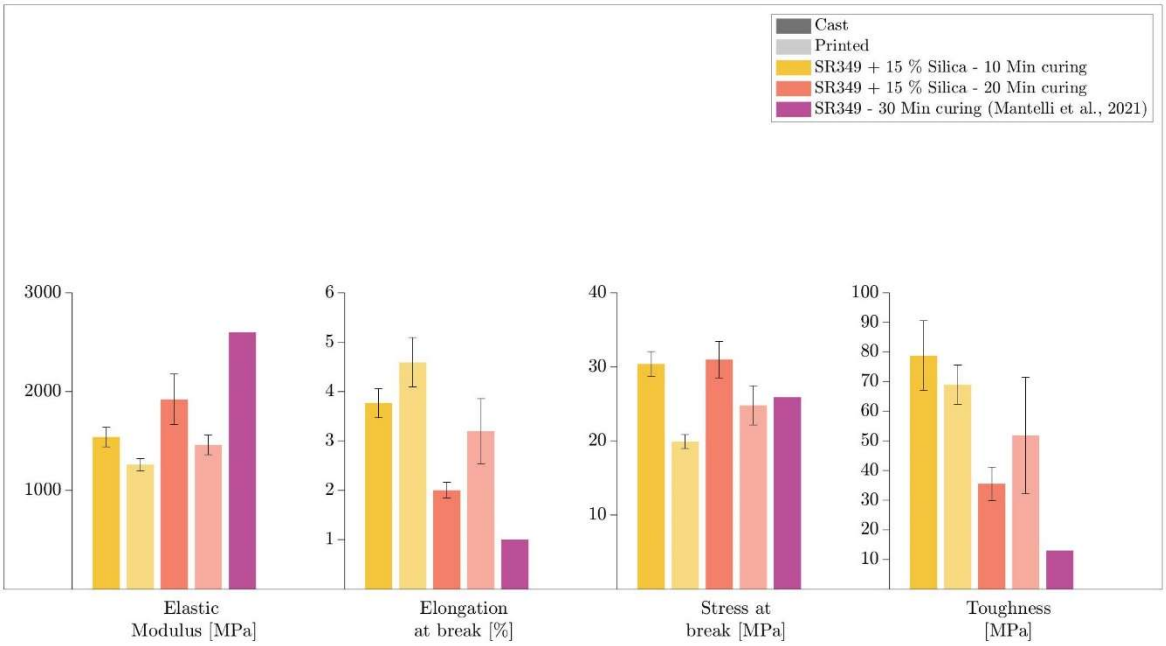

Figure 57: Summary of mechanical properties of printed and cast SRSX.

8.4.2. SR349 + Leather Results

8.4.2.1. Formulation

The specimens containing non-functionalised leather were not properly formulated as the filler did not disperse well in the resin, precipitating as soon as stirring was stopped.

Functionalisation worked, as the mixing between resin and functionalised filler was homogeneous. Consequently, for all subsequent characterisations, the specimens used were the functionalised ones.

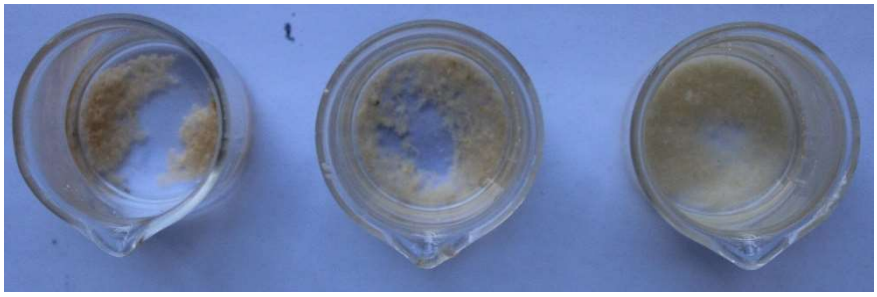

Figure 58: Qualitative test of leather dispersion in: acetone (left); ethanol (middle); water (right).

Figure 58 is only a qualitative test but shows well how the filler disperses well in polar solvents (water, right becker) while tending to aggregate in apolar solvents (acetone, left becker).

8.4.2.2. Rheological tests

Formulations containing three different contents of leather were characterized: 10, 15 and 20 % w/w with respect to the matrix. Frequency sweep test is performed to evaluate shear-thinning behavior. The frequency interval of the test is 0.01÷100 Hz and the amplitude of oscillation is 1%. Figure 59 shows results, where SRC10, SRC15, and SRC20 were analysed.

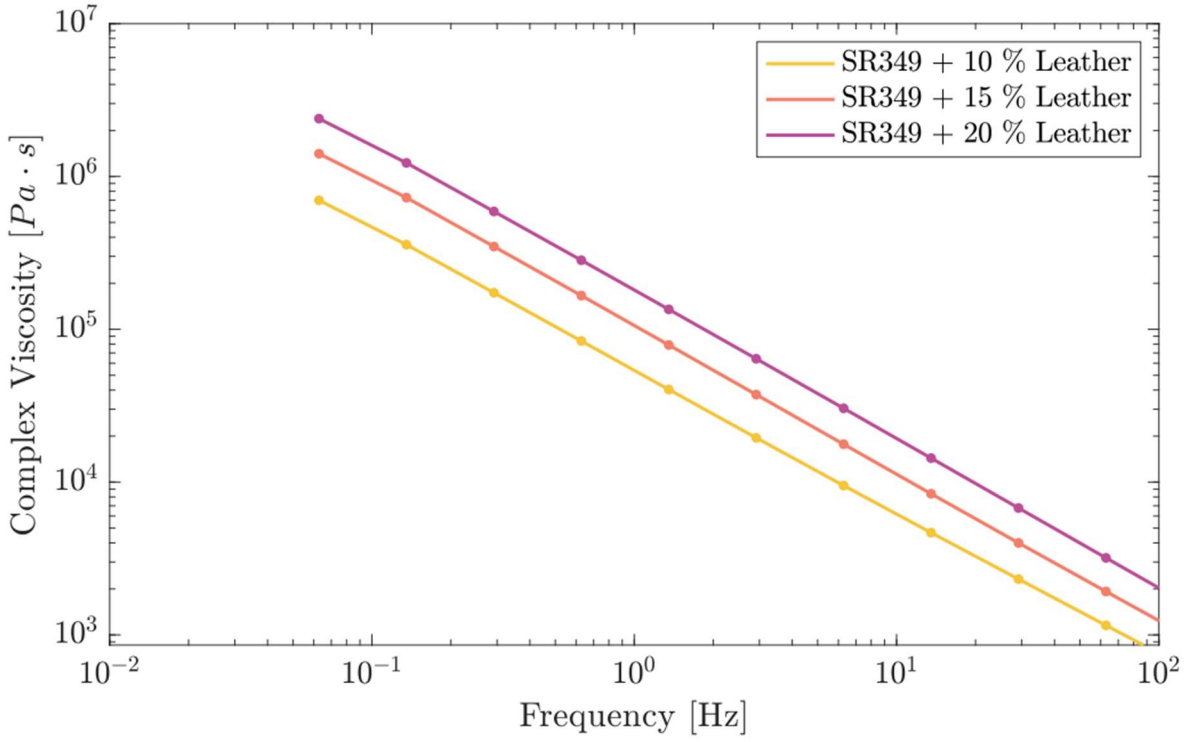

Figure 59: Frequency test of SR349+Leather formulations.

The amplitude sweep test is an oscillatory rheology test that involves the imposition of increasing shear amplitudes while maintaining a constant frequency, resulting in an escalating shear rate. This process allows the measurement of storage and loss moduli. Identifying the intersection point between G' and G'' is crucial, as it corresponds to the initiation of flow. The stress corresponding to this initiation is termed the yield stress, and the strain associated with it is known as the yield strain. The range of shear deformation during this test spans from 0% to 100%. Figure 60 shows the storage and loss moduli at varying strain. It can be noted how the deformation corresponding to the crosspoint decreases at higher leather content. Moduli increase with increasing leather content, coherently with what expected. In this case, no linear viscoelastic region is visible.

[61][61]

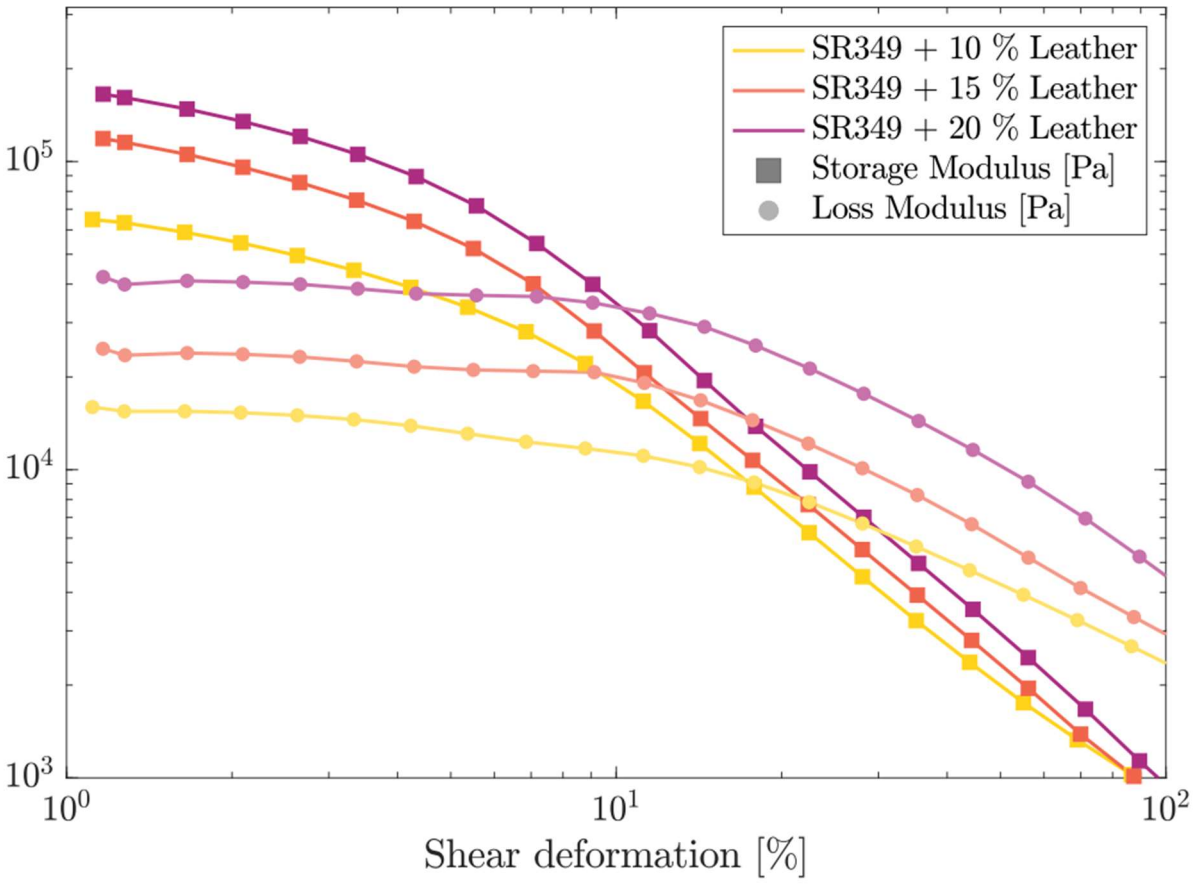

Figure 60: Amplitude sweep test of SR349+Leather formulations.

From this second test, yield stress and yield strain are extrapolated, as reported in Figure 61, that correspond to the crosspoints. The filler has a low bulk density, in fact during formulation it was seen that already at 10% by weight, the volume of filler relative to the matrix was high. This leads to paste-like formulations, so we expect the yield stress to increase as the filler increases. As far as deformation is concerned, it is understandable how formulations with a high solid fraction become less deformable as the latter increases.

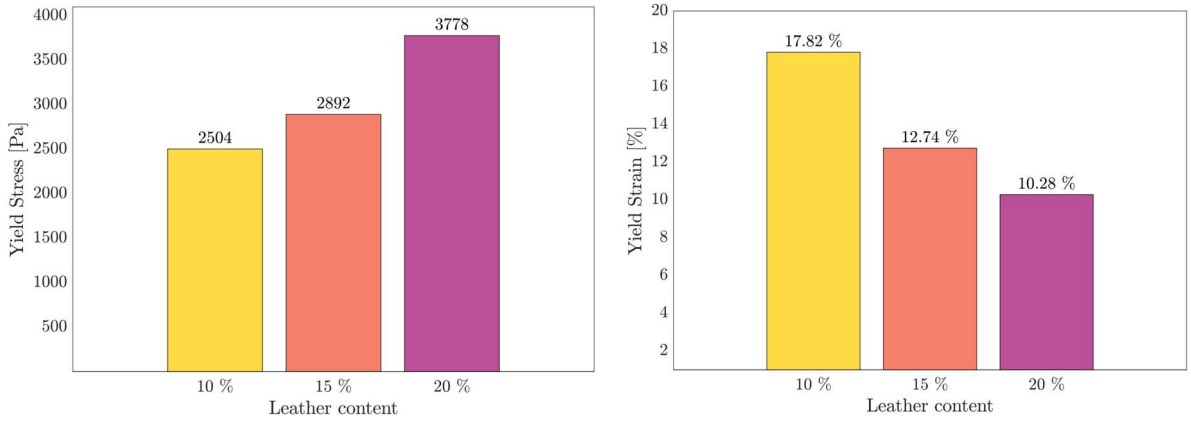

(a) Yield stress. (b) Yield strain.

Figure 61: Yield stress (a) and Yield strain (b) values of different SR349+Leather formulations.

The thixotropy test involves three sequential steps: (I) applying 1% shear deformation to simulate material in a cartridge; (II) subjecting the material to high shear deformation (100%) to simulate extrusion; (III) applying 1% shear deformation to simulate material on the printing plate. The frequency is 1 Hz for the three steps. Conservative (G') and dissipative (G'') moduli are measured. Initially, G' > G'' showing a solid-like behaviour for small deformations and therefore the presence of a yield point. This result is coherent with what found in the amplitude sweep test: yield deformation is higher than 1% for the three compositions and therefore solid-like behaviour was expected for this level of stimulus. During extrusion, G' < G'', indicating a liquid-like state. This shows how the flow onset is possible for higher force applied. This way, the material is extrudable. A quick return of G' above G'' post-extrusion is favourable, suggesting That the material can return to a solid-like behaviour after being extruded. The duration of each step is 300 s. The duration of the extrusion though the nozzle is in reality much faster. Therefore, it can be supposed that, being the duration of large deformation much smaller, the extent of thixotropy would be much lower during actual extrusion. Therefore, the materials are expected to come back to solid-like behaviour in a faster way than they did in the current test. Findings are depicted in Figure 62, in which G' and G'' as a function of the time. All formulations show a solid-like behaviour immediately after the start of the third step, which is to be expected given the high solid (volume) fraction of the formulation. It can be seen that the modulus increases as the amount of filler increases, consistent with what was found in the amplitude sweep.

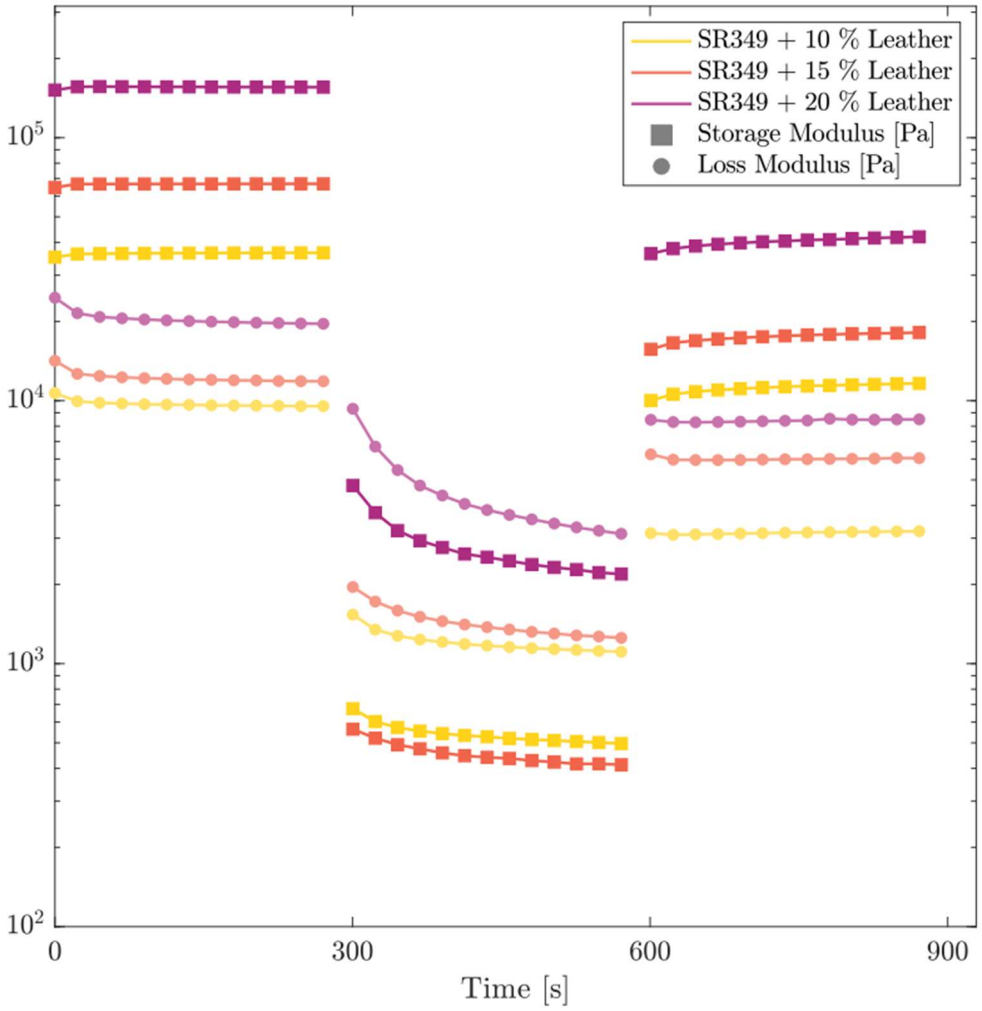

Figure 62: Thixotropy test of SR349+Leather formulations.

8.4.2.3. Printability tests

All formulations, 10, 15, and 20 % w/w of leather respect to the resin, are tested to evaluate the printability and stability behaviour, but, probably, during functionalisation perhaps the filler swells by being immersed in ethyl alcohol for 26h. This fact, coupled with the low viscosity of the resin, leads to demixing during extrusion and the formation of aggregates in the nozzle. This resulted in a discontinuous flow of material and an inability to print homogeneously.

In conclusion, SR349 + leather was successively tested only in cast.

8.4.2.4. Gel content

To investigate gel content percentages of printed samples, Eq. 9 was used.

$$Gel\% = \left(1 - \frac{w_0 - w_f}{w_0}\right) \times 100 \qquad 9$$

Table 16 shows the results. The gel content decreases as the filler content increases. It is very likely that the filler contains soluble components. This would confirm the trend and suggest that the gel contend is actually higher than measured.

Table 16: Gel content test results of SRCX.

Sample	Gel%
SRC10	92.31
SRC15	91.95
SRC20	83.03

8.4.2.5. UV-DSC

The evaluation of reacted functional groups in the material, trough the UV light, was performed through the UV-DSC test at room temperature. The UV intensity is 210.6 mW/cm² and the duration of the test is 15 minutes. In the following Table 17: UV-DSC test results of SRC10. test results are reported. Eq. 10 was used to calculate the curing percentages.

$$1 - \frac{\frac{H_{PC}}{\frac{1}{1+0.1}}}{\frac{H}{\frac{1}{1+0.1}}} \qquad 10$$

. Where 1 and 0.1 at denominators represents respectively the resin and filler fractions.

Table 17: UV-DSC test results of SRC10.

Sample	Curing%
SRC10	0.16

Only SRC10 was evaluated since the UV curing process is practically null. This result justifies the initial assumption to adopt a dual curing strategy because of the assumption that leather shields UV rays.

8.4.2.6. DSC

DSC tests were performed to know the glass transition temperature of the printed samples and their reacted functional groups using thermal source. For these specimens, a dual curing strategy was carried out. The range temperature starts from 25°C and arrives at 250°C with a rate of 10°C/min. In Table 18 T_g are reported. Eq. 10 shows the strategy adopted to calculate the curing percentages.

$$1 - \frac{\frac{H_{PC}}{\frac{1}{1+X}}}{\frac{H}{\frac{1}{1+X}}} \qquad 10$$

Where X represents the filler percentage (0.1 for 10%; 0.15 for 15%; 0.2 for 20%).

Table 18: DSC test results of SRCX.

Sample	Curing%	T_g [°C]
SRC10	87.95	43.96
SRC15	81.06	45.03
SRC20	98.48	45.24

There is no definite trend for either T_g or conversion rates, so all the matrix reticulates independently of the amount of filler.

Such a T_g is not very high. Given the intended application, i.e. the fashion/accessories market, it was nevertheless deemed acceptable but improvable.

8.4.2.7. Uniaxial tensile test

Mechanical behavior was investigated by means of uniaxial tensile testing only on casted specimens. Figure 63 shows the average curve trend of cast specimens, with a comparison with SRS15 cast. In Tab. X the average values of elastic modulus, maximum tensile strength, elongation at break and toughness were summarized, comparing cast samples with printed samples.

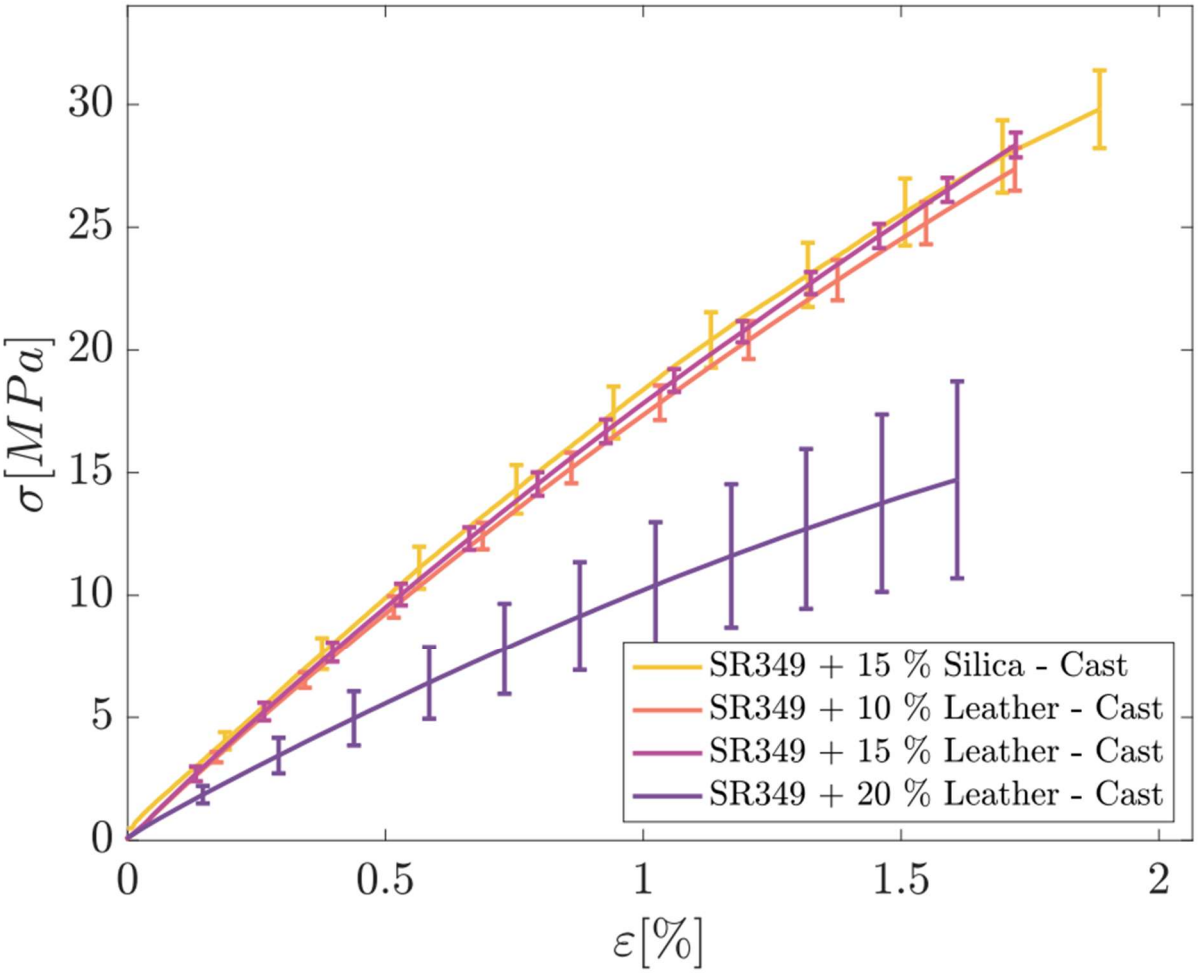

Figure 63: Mechanical test results of SRCX cast.

SRC10 and SRC15 exhibit similar characteristics compared to the control formulation (matrix+silica). This suggests that a uniform dispersion has been achieved, and the functionalization has effectively promoted compatibility between the matrix and the filler. However, a further increase in the filler quantity has a diminishing effect, indicating the establishment of a threshold value.

As previously mentioned, the small apparent density of the filler results in a high-volume fraction even at lower weight fractions. Consequently, it is reasonable to assume that a filler content of 20% w/w goes beyond the maximum limit for proper mixing and resin permeation into the filler.

Table 19 and Figure 64 summarised average mechanical properties, and standard deviation σ.

Table 19: Summary of mechanical properties of SRCX.

Sample	E [MPa] (σ)	σb [MPa] (σ)	εb [%] (σ)	k [MPa] (σ)
SRC10	1942.58 (91.12)	25.88 (2.88)	1.57 (0.28)	22.18 (6.35)
SRC15	1923.95 (64.26)	29.55 (3.36)	1.82 (0.23)	29.07 (7.67)
SRC20	1086.57 (179.26)	14.04 (4.03)	1.55 (0.25)	12.29 (5.26)
SRS15	1918 (255.09)	31.07 (2.46)	2.00 (0.16)	35.56 (5.66)

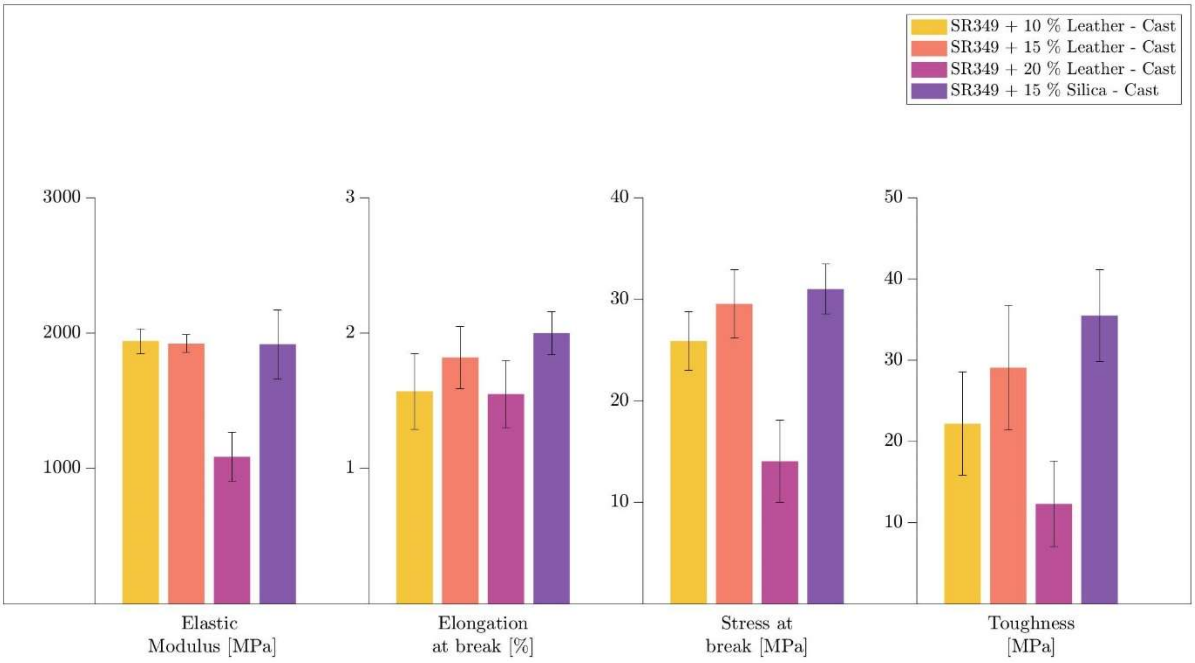

Figure 64: Summary of mechanical properties of printed and cast SRCX.

8.5. PVA Results

8.5.1. PVA + Silica Results

8.5.1.1. Rheological tests

Three different silica concentrations than PVA matrix were analysed: 10, 15, and 20 % w/w. Glycerol in 20% w/w respect to water and PVA, were added to formulations.

The frequency sweep test is executed to evaluate the pseudoplastic characteristics of the formulation. In this oscillatory test, an escalating frequency is applied, and the complex viscosity is measured. The frequency range for the test spans from 0.01 to 100

Hz, with a 1% amplitude of oscillation. The outcomes are depicted in Figure 65, illustrating that PVAS10, PVAS15, and PVAS20 exhibit pseudoplastic behavior, making them suitable for 3D printing. As in SR349 case, formulations with higher silica content demonstrate elevated viscosity across the entire frequency range.

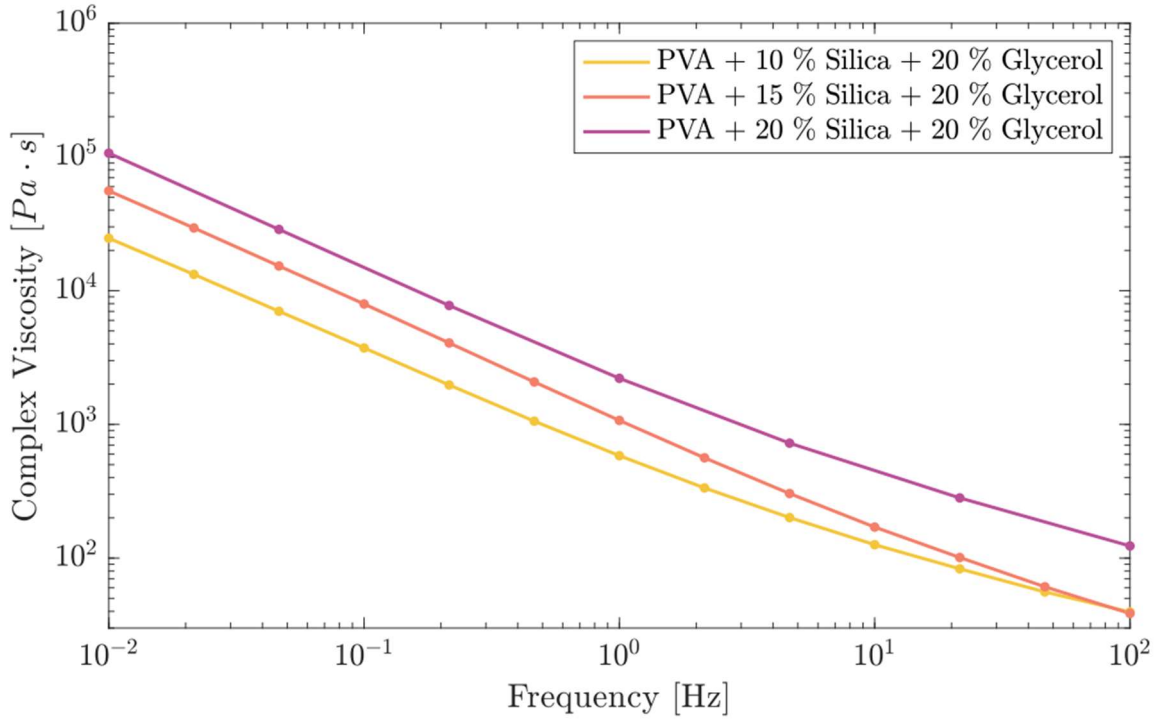

Figure 65: Frequency sweep test of PVA+Silica formulations.

The amplitude sweep involves applying progressively larger shear amplitudes at a constant frequency, leading to a gradual increase in shear rate. This method facilitates the measurement of storage and loss moduli. Identifying the point of intersection between G' and G'' is important, signifying the onset of flow. The stress at this initiation is the yield stress, and the corresponding strain is the yield strain. Shear deformation ranges from 0% to 100% during this test. Figure 66 illustrates the upward trend of the crosspoint with elevated silica content.

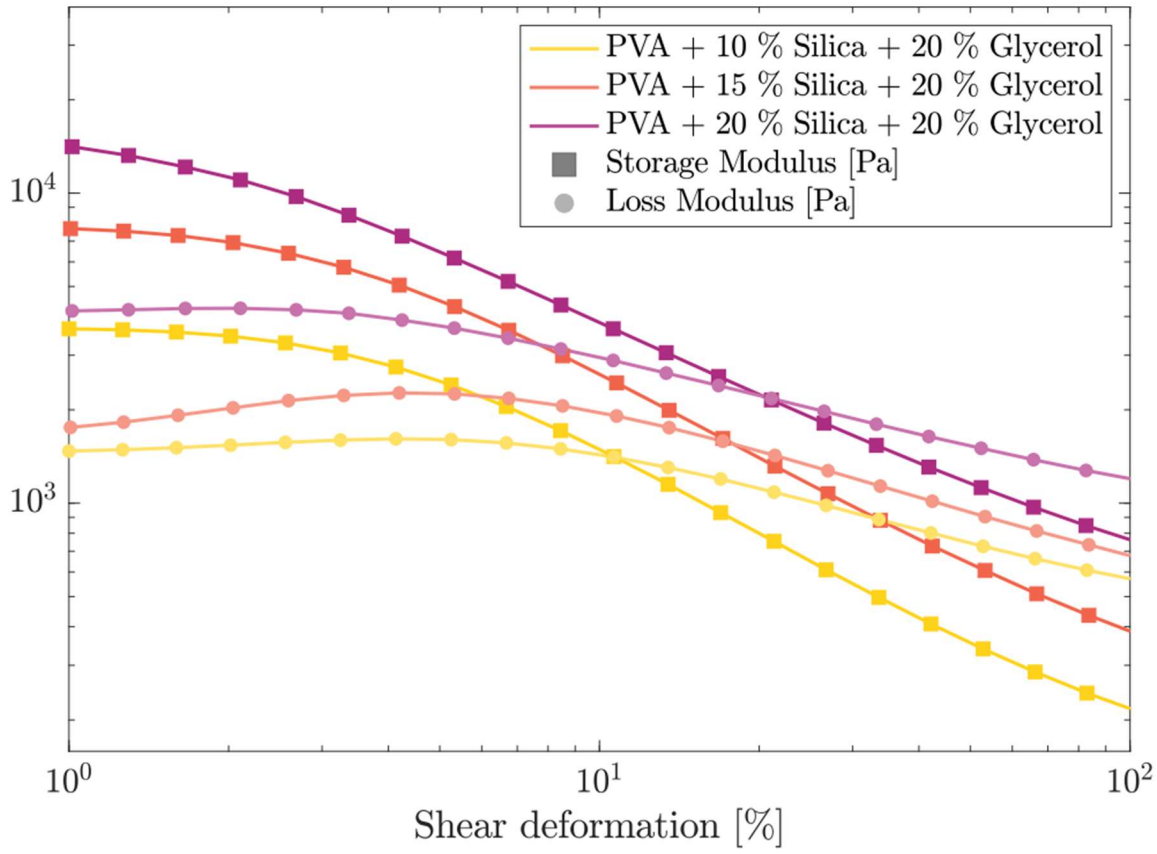

Figure 66: Amplitude sweep test of PVA+Silica formulations.

From this second test, yield stress and yield strain are extrapolated, as reported in Figure 67, that correspond to the crosspoints. In this case, yield stresses are not as high as in the previous case (SR349), so no printability problems due to inability to extrude are expected (as in the case of SRC20).

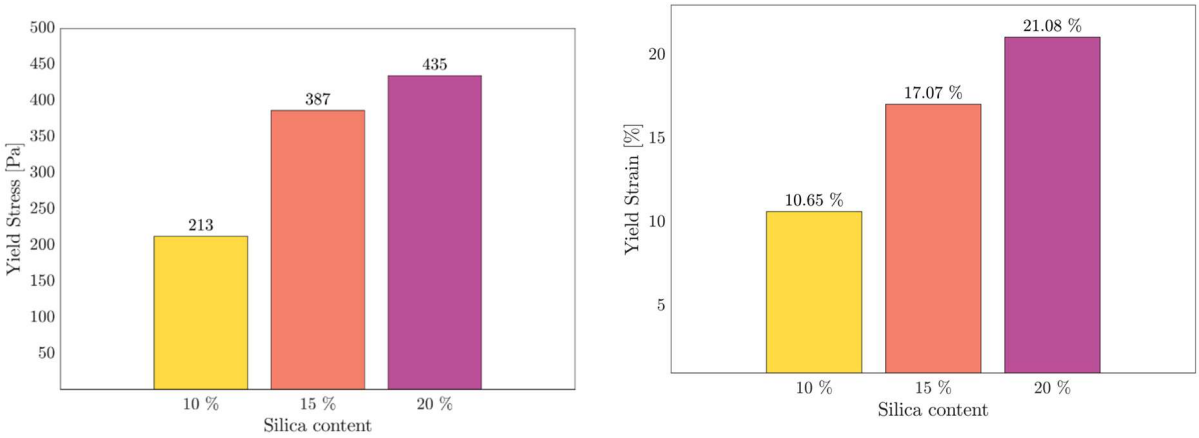

(a) Yield stress.

(b) Yield strain.

Figure 67: Yield stress (a) and Yield strain (b) values of different PVA+Silica formulations.

The thixotropy test comprises three steps: (I) applying 1% shear deformation to simulate material in a cartridge; (II) subjecting the material to high shear deformation

(100%) for extrusion simulation; (III) applying 1% shear deformation for material on the printing plate. Frequency is 1 Hz for all steps. Conservative (G') and dissipative (G'') moduli are measured over time. Initially, G' > G'', indicating solid-like behavior with a yield point. During extrusion, G' < G'', suggesting a liquid-like state, allowing extrusion. Rapid G' recovery post-extrusion is favorable, indicating a return to solid-like behavior. Each step lasts 300 s, with faster actual extrusion durations. Figure 68 illustrates the outcomes. With increased silica content, the crosspoint time decreases, implying a faster self-sustaining behavior (minimal difference between PVAS15 and PVAS20). Additionally, higher modulus values are observed in the three steps for higher silica contents, aligning with prior characterizations and expectations.

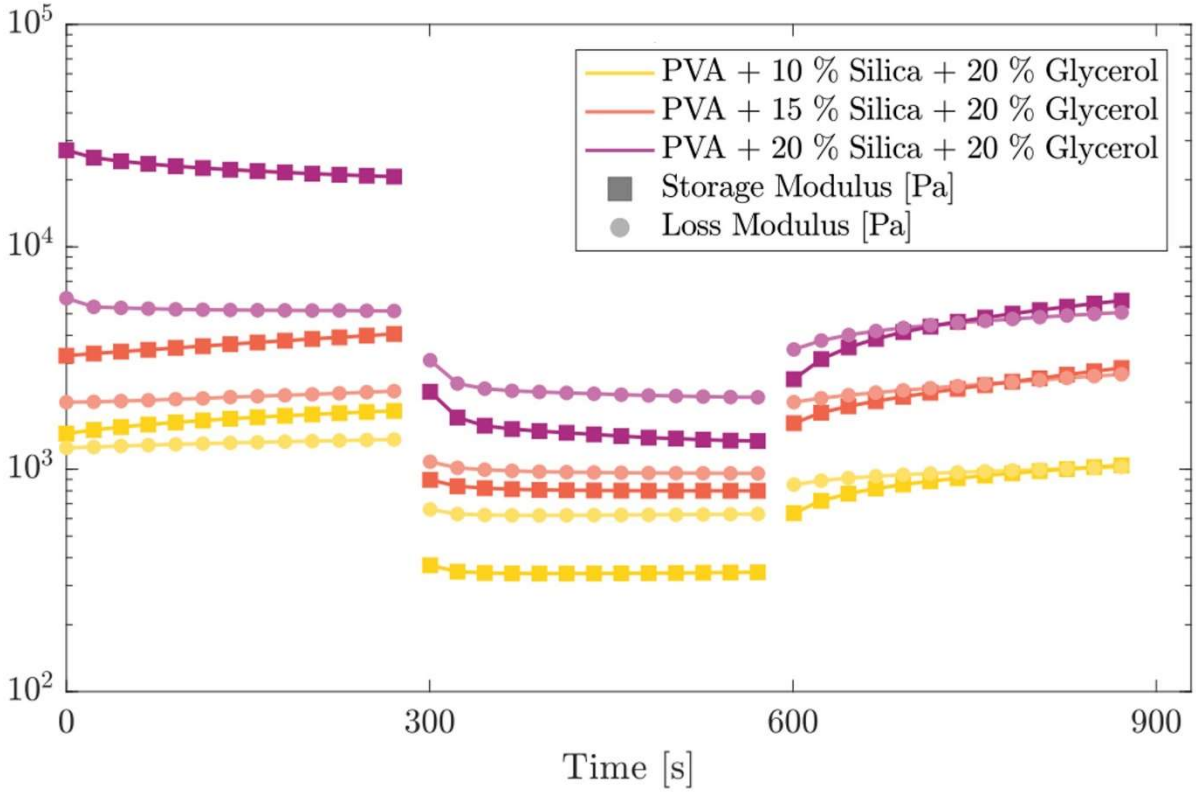

Figure 68: Thixotropy test of PVA+Silica formulations.

8.5.1.2. Printability tests

In this case silica filler was studied with the only purpose of understanding the mechanical properties of the PVA matrix, so no printability tests were done.

8.5.1.3. Gel content

To investigate gel content percentages of printed samples, Eq. 9 was used.

$$Gel\% = \left(1 - \frac{w_0 - w_f}{w_0}\right) \times 100 \qquad 9$$

In this case, w_0 takes into account lost glycerol, so it is not the entire sample weight, but the sample less the glycerol weight.

Only PVAS15 was taken into account and the result is represented in Table 20.

Table 20: Gel content test result of PVAS15.

Sample	Gel%
PVAS15	86.36

8.5.1.4. UV-DSC

The assessment of reactive functional groups in the material using UV light was conducted via the UV-DSC test carried out at room temperature. The UV intensity employed was 210.6 mW/cm², and the test duration extended for 15 minutes. The results, in Table 21, extrapolated from the curves obtained, show a practically complete cross-linking of the samples.

Table 21: UV-DSC test results of PVASX.

Sample	Curing%
PVAS10	≅ 100
PVAS15	≅ 100
PVAS20	≅ 100

8.5.1.5. DSC

DSC analyses were conducted to determine the glass transition temperature (T_g) of the PVAS15 casted samples. The temperature range initiated at 25°C and progressed to 250°C, with a heating rate of 10°C/minute. Table 22 details the recorded glass transition temperatures (T_g).

Table 22: DSC test results of PVASX.

Sample	T_g [°C]
PVAS15	44.21

8.5.1.6. Uniaxial tensile test

The mechanical characteristics were scrutinized through uniaxial tensile testing conducted on PVAS15 specimens. A comparison was made between material samples with and without glycerol to rationalize its application for enhancing PVA ductility. Figure 69 illustrates the averaged curve trends of the cast specimens.

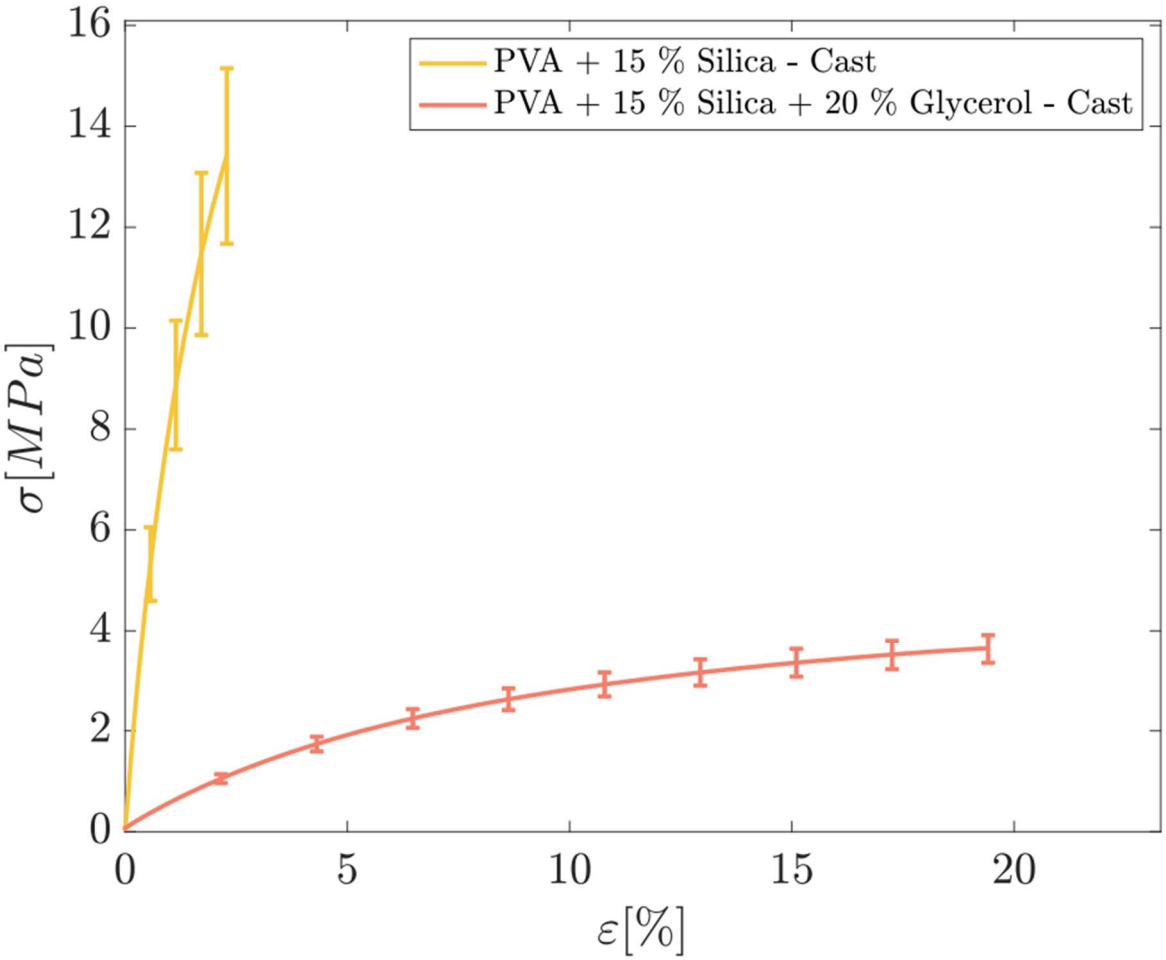

Figure 69: Mechanical test results of PVAS15 cast with and without glycerol.

From the graph is evident the different behavior of the two materials. Glycerol gives ductility to the virgin matrix decreasing the Young's modulus, elongation at break, and toughness, as the Table 23 and the summarize. Also standard deviations (σ) are reported. It can be seen how the material, initially rigid and brittle, takes on mechanical properties typical of elastomeric matrices.

Table 23: Summary of mechanical properties of PVAS15 cast with and without glycerol.

Sample	E [MPa] (σ)	σ_b [MPa] (σ)	ε_b [%] (σ)	k [MPa] (σ)
PVAS15 Cast	1162.07 (216.72)	14.44 (1.97)	2.28 (0.54)	20.42 (7.05)
PVAS15 + 20% Gly Cast	56.20 (5.15)	3.66 (0.16)	19.81 (2.07)	50.26 (5.43)

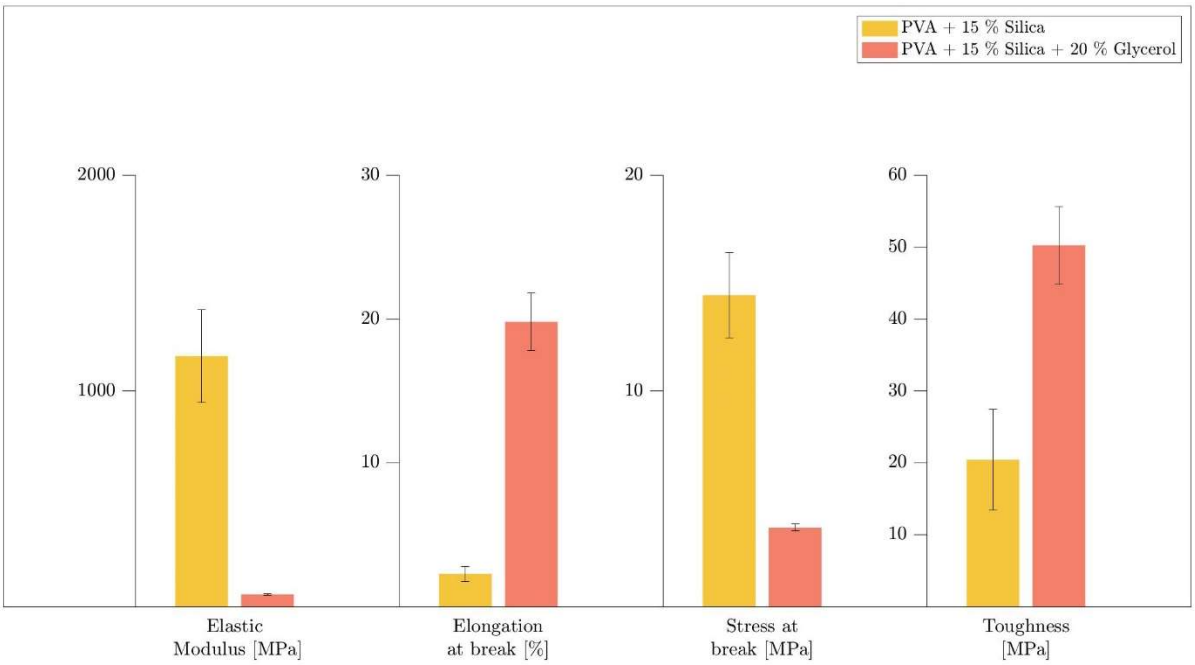

Figure 70: Summary of mechanical properties of printed and cast PVASX.

8.5.2. PVA + Leather Results

8.5.2.1. Rheological tests

Different concentrations of leather, 20%, 25%, and 30% w/w in relation to the matrix, were investigated. Again 20% w/w of glycerol is added.

The primary examination performed was the frequency sweep, with complex viscosity as the resultant parameter. The test encompasses a frequency range from 0.01 to 1000 Hz, employing a 1% oscillation amplitude. The results of these analyses are depicted in Figure 71.

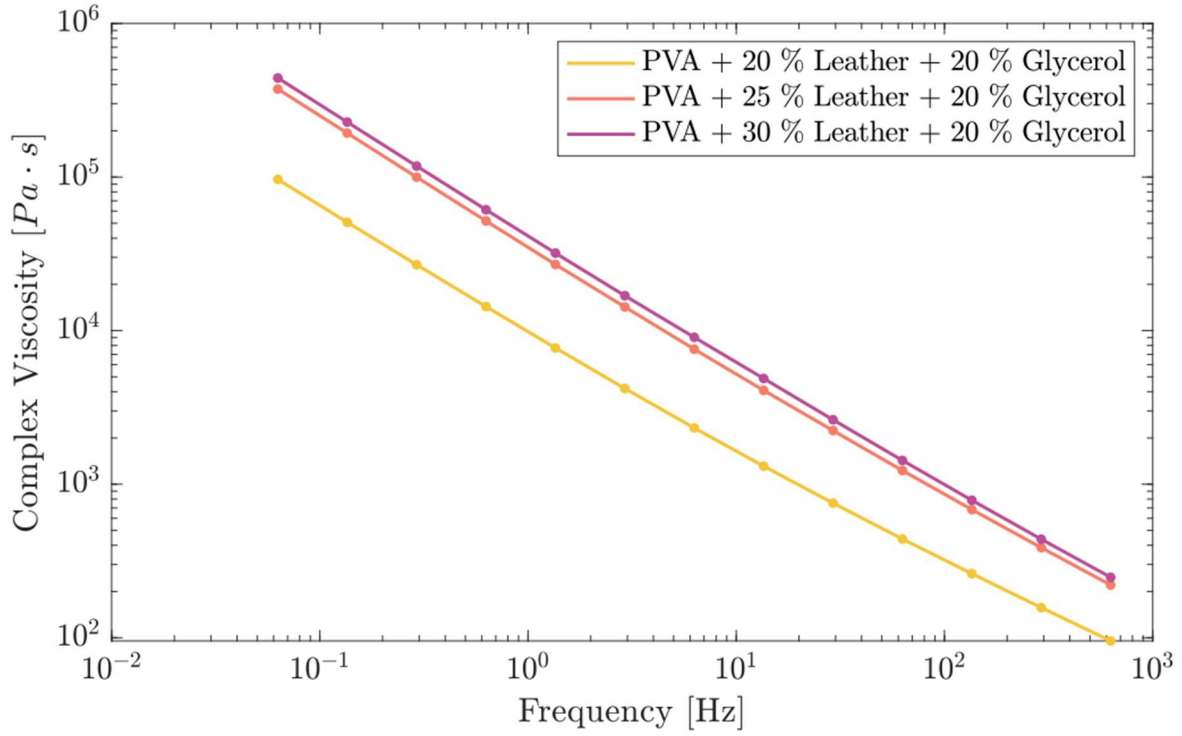

Figure 71: Frequency sweep test of PVA+Leather formulations.

The amplitude sweep test, an oscillatory rheology procedure, involves applying increasing shear amplitudes while maintaining a constant frequency, resulting in a rising shear rate. This method measures storage and loss moduli. Identifying the intersection of G' and G'' is crucial, marking the onset of flow. The stress at this point is the yield stress, and the corresponding strain is the yield strain. Shear deformation ranges from 0% to 100%. Figure 72 shows the storage and loss moduli with varying strain. The crosspoint deformation decreases with higher leather content, while moduli increase, aligning with expectations.

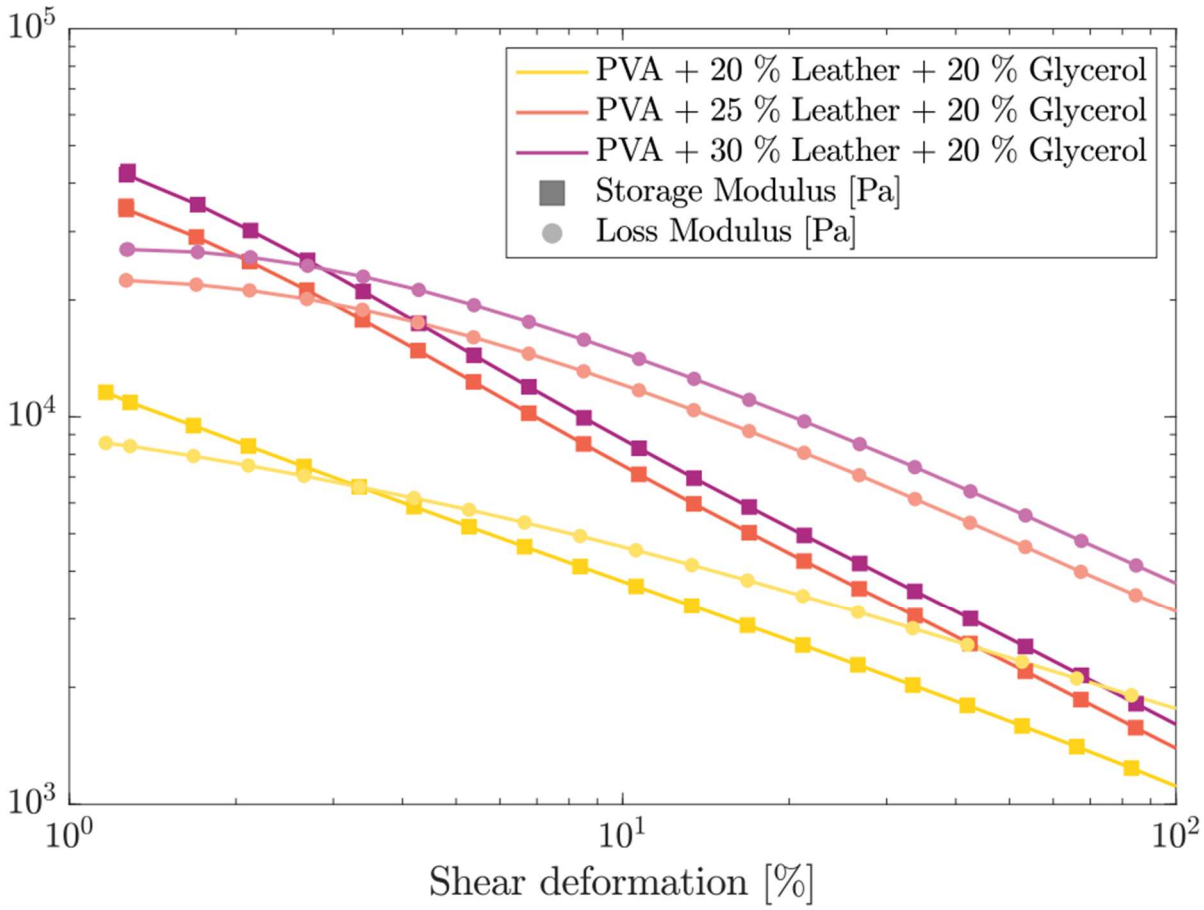

Figure 72: Amplitude sweep test of PVA+Leather formulations.

From this second test, yield stress and yield strain are extrapolated, as reported in Figure 73, that correspond to the crosspoints. The filler has a low bulk density, in fact during formulation it was seen that already at 20% by weight, the volume of filler relative to the matrix was high. This leads to paste-like formulations, so we expect the yield stress to increase as the filler increases. As far as deformation is concerned, it is understandable how formulations with a high solid fraction become less deformable as the latter increases.

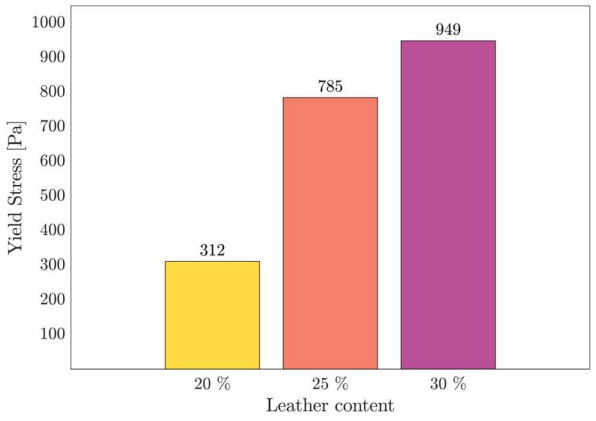

(a) Yield stress.

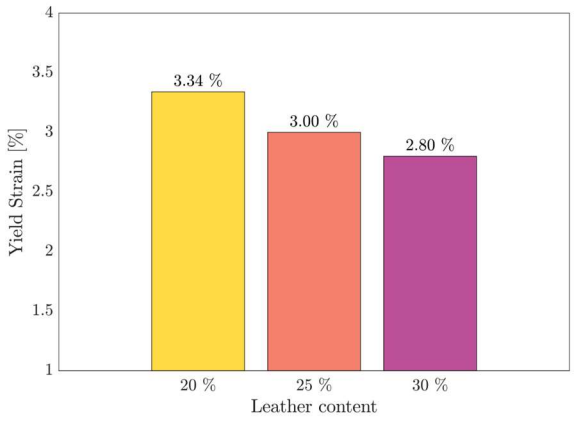

(b) Yield strain.

Figure 73: Yield stress (a) and Yield strain (b) values of different PVA+Leather formulations.

The examination of thixotropy involves three consecutive phases: (I) applying a 1% shear deformation to replicate material in a cartridge; (II) subjecting the substance to significant shear deformation (100%) to mimic extrusion; (III) implementing an additional 1% shear deformation to simulate material on a plate. The measurements encompass both conservative (G') and dissipative (G'') moduli. Initially, G' exceeds G'' due to a creep threshold. During extrusion, G' dips below G'', indicating a liquid-like state. A swift recovery of G' above G'' after extrusion is beneficial, signifying material cessation. Tests consist in 300 s steps, and the outcomes are depicted in Figure 74. All formulations show a solid-like behaviour immediately after the start of the third step, which is to be expected given the high solid (volume) fraction of the formulation. It can be seen that the modulus increases as the amount of filler increases, consistent with what was found in the amplitude sweep. They show also higher conservative modulus than dissipative one, although the discrepancy is small, immediately after the beginning of the third step.

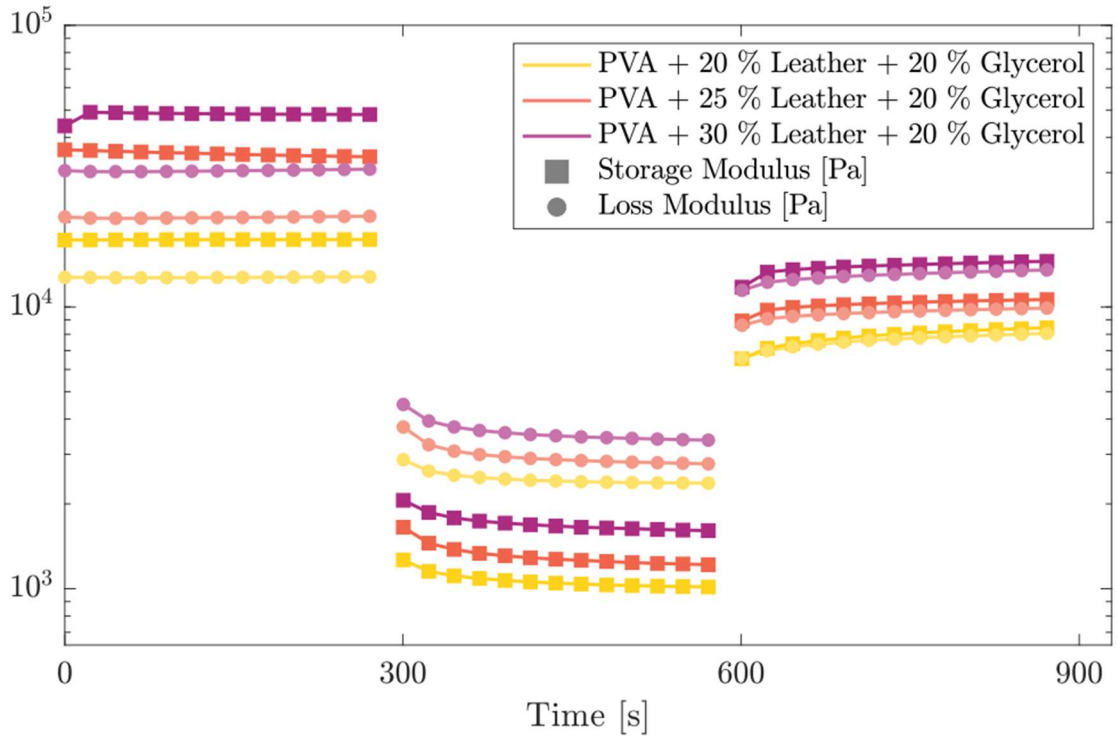

Figure 74: Thixotropy test of PVA+Leather formulations.

8.5.2.2. Printability tests

Starting from the filament uniformity, in Figure 75 are reported all results. Taken the average diameter of the printed filament as the reference parameter, the uniformity was calculated for all PVA formulations. Eq. 7 was used for the test.

$$U = \frac{\sum_{i=1}^{N} |d_i - d_{av}|}{N} \qquad 7$$

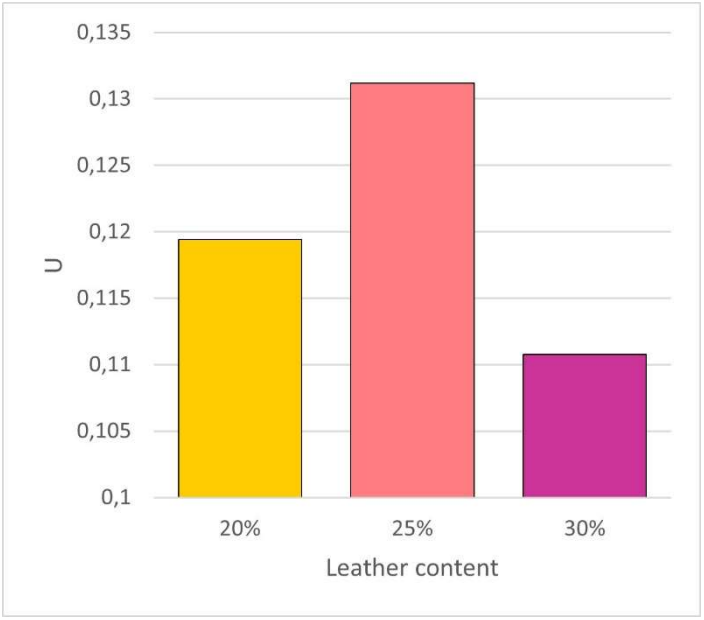

Figure 75: Filament uniformity test of PVACX.

The filament fusion test, as illustrated in Figure 76, is an additional assessment of stability. By reducing the separation between filaments, one can gauge their stability. Parameters under consideration include filament distances (f_d), which diminish during the test and are proportional to the nozzle diameter, fused segment length (f_s), and filament thickness (f_t).

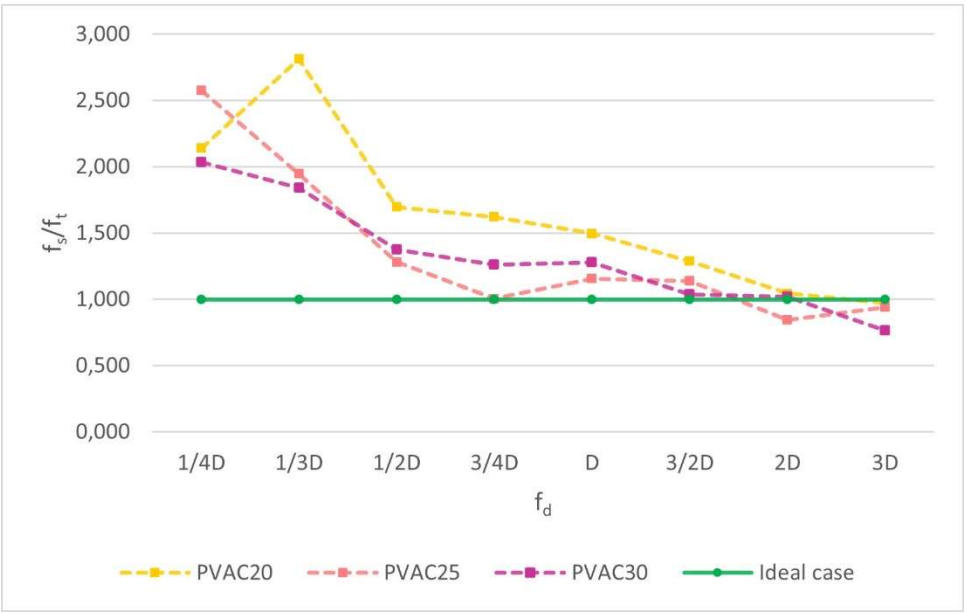

Figure 76: Filament fusion test of PVACX.

The distances covered follow the proportionality of the nozzle diameter. All three formulations exhibit excellent printing performance, displaying no noticeable differences, but PVAC25 and PVAC30 demonstrated similar printability.

In the final assessment, the grid view examines stability and printability using the printing index (P_r) as defined in Eq. 8. Figure 77 displays the outcomes for various formulations.

$$P_r = \frac{l^2}{16A} \quad (8)$$

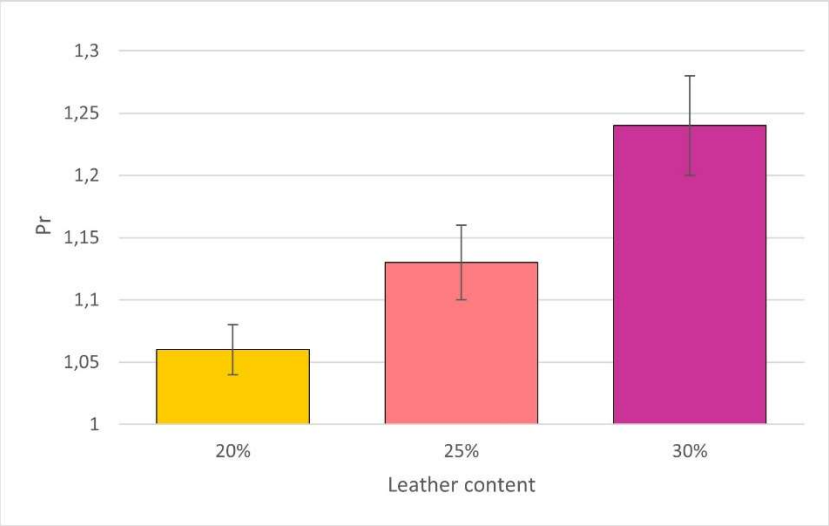

Figure 77: Grid test of PVACX.

There is a clear trend in the parameter. For higher leather values, the index increases. This is justified by the fact that, when the nozzle crosses the already printed filaments, it drags material with it. As a result, it can be seen that the greater the amount of leather equals the greater the amount of material dragged.

8.5.2.3. Gel content

Eq. 9 was used to investigate gel content percentages of different formulations.

$$Gel\% = \left(1 - \frac{w_0 - w_f}{w_0}\right) \times 100 \quad (9)$$

Also here w_0 takes into account lost glycerol, so it is not the entire sample weight, but the sample less the glycerol weight. The gel content decreases as the filler content increases. It is very likely that the filler contains water-soluble components. This would confirm the trend and suggest that the gel contend is actually higher than measured. Table 24 shows the results.

Table 24: Gel content results of PVACX.

Sample	Gel%
PVAC20	99.19
PVAC25	96.38
PVAC30	89.14

8.5.2.4. UV-DSC

The analysis of reactive functional groups in the material using UV light was performed through the UV-DSC test conducted at room temperature. The test utilized a UV intensity of 210.6 mW/cm², and the duration extended for 15 minutes. The results of the test are because of the null ability of UV to crosslink. Also these results justify the dual curing strategy.

8.5.2.5. DSC

DSC analyses were conducted to determine the glass transition temperature (T_g) of the casted specimens and their thermal curing percentage. The temperature range initiated at X°C and progressed to 250°C, with a heating rate of 10°C/minute. Table 25details the recorded T_g and curing percentages.

Table 25: DSC test results of PVACX.

Sample	Curing%	T_g [°C]
PVAC20	72.17	43.83
PVAC25	90.89	47.26
PVAC30	88.74	47.08

The observed conversions are relatively low, depending on the nature of the process. The material being cured is a polymer which can crosslink in correspondence on the few methacrylic groups added, in contrast to usual monomers with low molecular weight and many crosslinking sites. The limited availability of crosslinkable groups fand the reduced mobility of polymeric PVA chains leads to a very slow kinetic profile at elevated conversion levels, residual reactive groups are very unlikely to meet.

Nevertheless, this result is not a big concern. Unreacted molecules are anyway high molecular weight polymeric chains, excluding concerns of toxicity associated with usual monomeric residues. Moreover, the mechanical properties remain largely unaffected, as the unreacted material does not impart the typical plasticizing effects characteristic of residual monomers.

There is no consistent trend observed for the rates of T_g. The values are not exceptionally high. However, considering the intended use in the fashion and accessories market, they are considered acceptable but with room for improvement.

8.5.2.6. Uniaxial tensile test

The mechanical attributes were examined using uniaxial tensile testing on both printed and cast specimens with varying formulations. Figure 78 depicts the average trends of the curves for these specimens proposing a comparison with the PVAS15 cast.

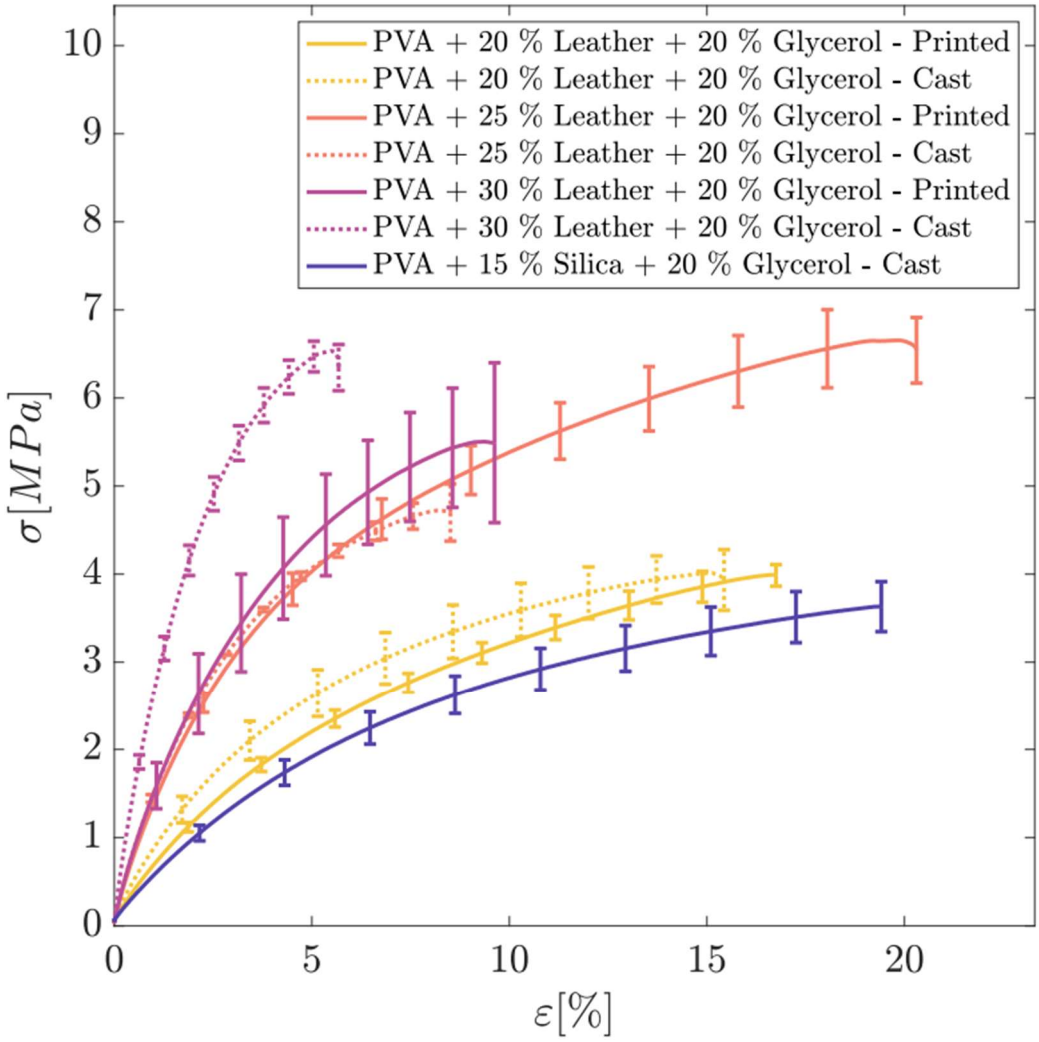

Figure 78: Mechanical test of printed and cast PVACX.

All compositions exhibit a higher modulus and tensile strength compared to the control composition of PVA+Silica+Glycerol. Consequently, it can be inferred that the filler, without any functionalization, has been adequately dispersed, exhibiting good adhesion and impregnation with the matrix. The filler, therefore, serves a reinforcing function.

The printed specimens show increased elongation at break, and a lower modulus and tensile strength. It is evident that the printing process has an impact on the material. It is plausible to hypothesize that extrusion through a nozzle aligns the filler within the material. Given the branched morphology of leather particles, this alignment might result in an apparently lower volumetric fraction within the material. Consequently, the reinforcing action of the filler is mitigated.

All formulations display mechanical properties typical of elastomeric resins and are potentially usable with appropriate design and sizing of the produced parts. The goal of these formulations was to emulate the mechanical characteristics of virgin leather, approximately 100 MPa modulus, 10% elongation at break, and 10% deformation at

break. The PVAC25 printed formulation closely approaches this target. Testing various combinations of plasticizers and fillers makes it presumable that the target can be achieved.

It is worth noting that the major polyurethanes used to produce synthetic leather have mechanical properties significantly different from those of virgin leather but are still employed with suitable sizing adjustments.

Young's modulus, elongation at break, and toughness averages, with their respective standard deviations σ, are summarized in Table 26 and in Figure 79.

Table 26: Summary of mechanical properties of printed and cast PVACX.

Sample	E [MPa] (σ)	σ_b [MPa] (σ)	ε_b [%] (σ)	k [MPa] (σ)
PVAC20 - Printed	74.18 (3.54)	3.96 (0.19)	17.64 (2.90)	47.96 (11.05)
PVAC20 - Cast	108.32 (15.53)	4.02 (0.17)	14.63 (3.11)	41.38 (11.85)
PVAC25 - Printed	170.77 (11.00)	6.67 (0.34)	19.25 (2.57)	94.37 (12.89)
PVAC25 - Cast	175.36 (16.56)	4.78 (0.28)	9.17 (1.32)	27.54 (1.41)
PVAC30 - Printed	178.57 (15.03)	5.72 (0.85)	12.45 (1.80)	50.05 (19.64)
PVAC30 - Cast	310.03 (22.62)	6.29 (0.63)	5.95 (1.06)	26.75 (8.55)
PVAS15 - Cast	56.20 (5.15)	3.66 (0.16)	19.81 (2.07)	50.26 (5.43)

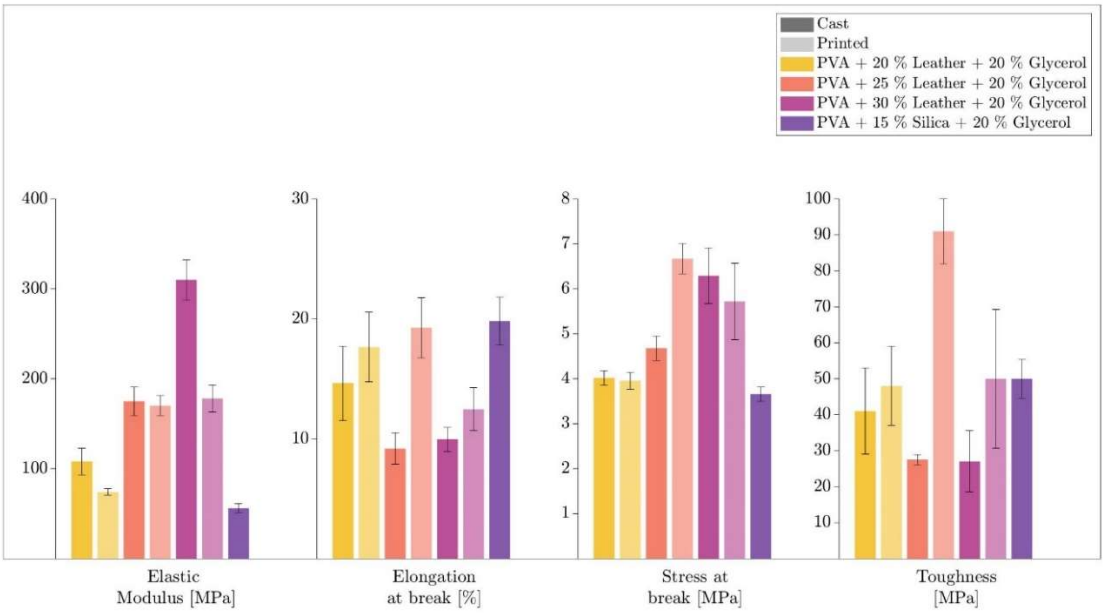

Figure 79: Summary of mechanical properties of printed and cast PVACX.

The result of a 4x4 cm 3D printed sample is shown in Figure 80.

Figure 80: Results of 3D printed sample after: printing (left), curing (middle); drying (right).

8.3.2.6.1. Material formulations

Here a summary of all PVA+Leather formulations is done in Table 27. Percentages are referred to the total mass of the specimens. A comparison between weight fractions before and after drying was evaluated, considered null the water fraction.

Table 27: PVACX weight fraction before and after drying.

Sample	H_2O%	PVA%	Leather%	Irgacure 2959 %	Dicumyl peroxide %	Glycerol%
PVAC20	52.77%	17.41%	14.04%	1.58%	0.16%	14.04%
PVAC25	50.98%	16.82%	16.95%	1.53%	0.15%	13.56%
PVAC30	49.31%	16.27%	19.67%	1.48%	0.15%	13.12%
PVAC20 - Dry	-	36.87%	29.72%	3.35%	0.34%	29.72%
PVAC25 - Dry	-	34.32%	34.58%	3.12%	0.31%	27.67%
PVAC30 - Dry	-	32.10%	38.81%	2.92%	0.29%	25.88%

9 Conclusions

In this work the evaluation of leather as reinforcing filler for 3D printing is done. This was born from the environmental impact aims, that, with continued growth in demand in the coming years, will become increasingly important.

From this point of view, thanks to LCA, it was demonstrated the important difference between a conventional leather industry production, and a recycled leather production through the additive manufacturing.

Also the goal as filler composite for polymer matrices was successfully achieved. Rigid and ductile matrices, respectively SR349 and PVA, responded very well to the mechanical tests, highlighting a threshold value for the leather concentration. Curing characterization confirmed the proper crosslinking of the different formulations, due to the dual curing strategy with thermal and UV-light sources.

As regard the printability, PVA shown high printing qualities. Due to the high leather concentration, PVAC30 has been the most complicated, the very low printing speed (1 mm/s), resulting from the low ink flow, is a demonstration of that. Considering both printing and mechanical characteristics, PVAC25 results the best one thanks a regular ink flow without defects and good mechanical properties.

SR349 resulted non-ideal as polymer matrix for leather. Despite the use of the biggest diameter nozzle, 1.6 mm, the main problem was related to the continuous clogging of the latter, resulting in an intermittent flow. This caused an incomplete print, with material missing. This could be caused by a not perfect chemical affinity of resin and filler, non-polar resin and polar leather, or due to the filler dimension. Nowadays, SR349 with leather fillers, can be used for cast applications. In this case an evident threshold of leather concentration will notice, specifically over 15% w/w. Some future developments have been investigated for SR349 matrix and leather fillers, and their ability to be printed, as reducing the leather dimensions, avoiding clusters formation, or find the most suitable functionalization process to avoid swelling of the leather by immersion in solution.

The main future goal regards the applications of these materials. By varying the leather concentration and the glycerol (only for PVA formulations) one, different behaviors were shown by materials, and consequently different applications could be recovered by them.

Also environmental end-of-life impacts for 3D-Printed recycled leather composites have to be assessed, due to no accurate existing literature data on leather goods.

Bibliography

[1] "ISO/ASTM 52900:2021(en), Additive manufacturing — General principles — Fundamentals and vocabulary." https://www.iso.org/obp/ui/#iso:std:iso-astm:52900:ed-2:v1:en (accessed Sep. 11, 2023).

[2] W. Gao *et al.*, "The status, challenges, and future of additive manufacturing in engineering," *CAD Comput. Aided Des.*, vol. 69, pp. 65–89, 2015, doi: 10.1016/j.cad.2015.04.001.

[3] K. P. Karunakaran, A. Bernard, S. Suryakumar, L. Dembinski, and G. Taillandier, "Rapid manufacturing of metallic objects," *Rapid Prototyp. J.*, vol. 18, no. 4, pp. 264–280, Jan. 2012, doi: 10.1108/13552541211231644.

[4] D. Bak, "Rapid prototyping or rapid production? 3D printing processes move industry towards the latter," *Assem. Autom.*, vol. 23, no. 4, pp. 340–345, Jan. 2003, doi: 10.1108/01445150310501190.

[5] N. Hopkinson, R. Hague, and P. Dickens, *Rapid Manufacturing: An Industrial Revolution for the Digital Age*. 2006.

[6] S. C. Ligon, R. Liska, J. Stampfl, M. Gurr, and R. Mülhaupt, "Polymers for 3D Printing and Customized Additive Manufacturing," *Chem. Rev.*, vol. 117, no. 15, pp. 10212–10290, 2017, doi: 10.1021/acs.chemrev.7b00074.

[7] W. Oropallo and L. A. Piegl, "Ten challenges in 3D printing," *Eng. Comput.*, vol. 32, no. 1, pp. 135–148, 2016, doi: 10.1007/s00366-015-0407-0.

[8] T. D. Ngo, A. Kashani, G. Imbalzano, K. T. Q. Nguyen, and D. Hui, "Additive manufacturing (3D printing): A review of materials, methods, applications and challenges," *Compos. Part B Eng.*, vol. 143, pp. 172–196, 2018, doi: 10.1016/j.compositesb.2018.02.012.

[9] D. Ahn, H. Kim, and S. Lee, "Fabrication direction optimization to minimize post-machining in layered manufacturing," *Int. J. Mach. Tools Manuf.*, vol. 47, no. 3–4, pp. 593–606, 2007, doi: 10.1016/j.ijmachtools.2006.05.004.

[10] S. K. Bhargava, S. Ramakrishna, M. Brandt, and P. R. Selvakannan, *Additive Manufacturing for Chemical Sciences and Engineering*. Springer Nature, 2022.

[11] A. Al-Ahmad *et al.*, "Bacterial and Candida albicans adhesion on rapid prototyping-produced 3D-scaffolds manufactured as bone replacement materials," *J. Biomed. Mater. Res. Part A*, vol. 87A, no. 4, pp. 933–943, Dec. 2008, doi: https://doi.org/10.1002/jbm.a.31832.

[12] M. W. Laschke *et al.*, "Incorporation of growth factor containing Matrigel promotes vascularization of porous PLGA scaffolds," *J. Biomed. Mater. Res. Part A*, vol. 85A, no. 2, pp. 397–407, May 2008, doi: https://doi.org/10.1002/jbm.a.31503.

[13] M. Rücker *et al.*, "Vascularization and biocompatibility of scaffolds consisting of different calcium phosphate compounds," *J. Biomed. Mater. Res. - Part A*, vol. 86, no. 4, pp. 1002–1011, 2008, doi: 10.1002/jbm.a.31722.

[14] M. Rücker *et al.*, "Angiogenic and inflammatory response to biodegradable scaffolds in dorsal skinfold chambers of mice," *Biomaterials*, vol. 27, no. 29, pp. 5027–5038, 2006, doi: 10.1016/j.biomaterials.2006.05.033.

[15] S. Castillo, D. Muse, F. Medina, E. Macdonald, and R. Wicker, "Electronics integration in conformal substrates fabricated with additive layered manufacturing," *20th Annu. Int. Solid Free. Fabr. Symp. SFF 2009*, pp. 730–737, Jan. 2009.

[16] F. Medina *et al.*, "Integrating multiple rapid manufacturing technologies for developing advanced customized functional devices," *Rapid Prototyp. Manuf. 2005 Conf. Proc.*, pp. 10–12, Jan. 2005.

[17] S. B. Kesner and R. D. Howe, "Design Principles for Rapid Prototyping Forces Sensors Using 3-D Printing," *IEEE/ASME Trans. Mechatronics*, vol. 16, no. 5, pp. 866–870, 2011, doi: 10.1109/TMECH.2011.2160353.

[18] M. Melzer *et al.*, "Elastic magnetic sensor with isotropic sensitivity for in-flow detection of magnetic objects," *RSC Adv.*, vol. 2, no. 6, pp. 2284–2288, 2012, doi: 10.1039/c2ra01062c.

[19] I. Gibson, T. Kvan, and L. Wai Ming, "Rapid prototyping for architectural models," *Rapid Prototyp. J.*, vol. 8, no. 2, pp. 91–95, Jan. 2002, doi: 10.1108/13552540210420961.

[20] S. Wannarumon and E. Bohez, "Rapid Prototyping and Tooling Technology in Jewelry CAD," *Comput. Aided. Des. Appl.*, vol. 1, Jan. 2004, doi: 10.1080/16864360.2004.10738300.

[21] P. Wu, J. Wang, and X. Wang, "A critical review of the use of 3-D printing in the construction industry," *Autom. Constr.*, vol. 68, pp. 21–31, 2016, doi: https://doi.org/10.1016/j.autcon.2016.04.005.

[22] N. R. Council, *Accelerating Technology Transition: Bridging the Valley of Death for Materials and Processes in Defense Systems*. Washington, DC: The National

Academies Press, 2004.

[23] "Scopus - Document search." https://www.scopus.com/search/form.uri?display=basic#basic (accessed Nov. 14, 2023).

[24] I. Gibson, D. Rosen, and B. Stucker, *Additive manufacturing technologies: 3D printing, rapid prototyping, and direct digital manufacturing, second edition*. 2015.

[25] J.-Y. Lee, J. An, and C. K. Chua, "Fundamentals and applications of 3D printing for novel materials," *Appl. Mater. Today*, vol. 7, pp. 120–133, 2017, doi: 10.1016/j.apmt.2017.02.004.

[26] J. R. C. Dizon, A. H. Espera, Q. Chen, and R. C. Advincula, "Mechanical characterization of 3D-printed polymers," *Addit. Manuf.*, vol. 20, pp. 44–67, 2018, doi: 10.1016/j.addma.2017.12.002.

[27] O. A. Mohamed, S. H. Masood, and J. L. Bhowmik, "Optimization of fused deposition modeling process parameters: a review of current research and future prospects," *Adv. Manuf.*, vol. 3, no. 1, pp. 42–53, 2015, doi: 10.1007/s40436-014-0097-7.

[28] A. K. Sood, R. K. Ohdar, and S. S. Mahapatra, "Parametric appraisal of mechanical property of fused deposition modelling processed parts," *Mater. Des.*, vol. 31, no. 1, pp. 287–295, 2010, doi: 10.1016/j.matdes.2009.06.016.

[29] P. Parandoush and D. Lin, "A review on additive manufacturing of polymer-fiber composites," *Compos. Struct.*, vol. 182, pp. 36–53, 2017, doi: 10.1016/j.compstruct.2017.08.088.

[30] X. Wang, M. Jiang, Z. Zhou, J. Gou, and D. Hui, "3D printing of polymer matrix composites: A review and prospective," *Compos. Part B Eng.*, vol. 110, pp. 442–458, 2017, doi: 10.1016/j.compositesb.2016.11.034.

[31] C. F. Revelo and H. A. Colorado, "3D printing of kaolinite clay ceramics using the Direct Ink Writing (DIW) technique," *Ceram. Int.*, vol. 44, no. 5, pp. 5673–5682, 2018, doi: https://doi.org/10.1016/j.ceramint.2017.12.219.

[32] L. Zhou, J. Fu, Q. Gao, P. Zhao, and Y. He, "All-Printed Flexible and Stretchable Electronics with Pressing or Freezing Activatable Liquid-Metal–Silicone Inks," *Adv. Funct. Mater.*, vol. 30, no. 3, p. 1906683, Jan. 2020, doi: https://doi.org/10.1002/adfm.201906683.

[33] S. Gu, Y. Tian, K. Liang, and Y. Ji, "Chitin nanocrystals assisted 3D printing of polycitrate thermoset bioelastomers," *Carbohydr. Polym.*, vol. 256, p. 117549, 2021, doi: https://doi.org/10.1016/j.carbpol.2020.117549.

[34] Z. Guo, P. Yu, Y. Liu, and J. Zhao, "High-precision resistance strain sensors of multilayer composite structure via direct ink writing: Optimized layer flatness

and interfacial strength," *Compos. Sci. Technol.*, vol. 201, p. 108530, 2021, doi: https://doi.org/10.1016/j.compscitech.2020.108530.

[35] M. Hausmann *et al.*, "Dynamics of Cellulose Nanocrystal Alignment During 3D Printing," *ACS Nano*, vol. 12, Jul. 2018, doi: 10.1021/acsnano.8b02366.

[36] A. Reiser *et al.*, "Multi-metal electrohydrodynamic redox 3D printing at the submicron scale," *Nat. Commun.*, vol. 10, no. 1, p. 1853, 2019, doi: 10.1038/s41467-019-09827-1.

[37] R. Ajdary *et al.*, "Acetylated Nanocellulose for Single-Component Bioinks and Cell Proliferation on 3D-Printed Scaffolds," *Biomacromolecules*, vol. 20, no. 7, pp. 2770–2778, 2019, doi: https://doi.org/10.1021/acs.biomac.9b00527.

[38] G. Yang *et al.*, "Direct-ink-writing (DIW) 3D printing functional composite materials based on supra-molecular interaction," *Compos. Sci. Technol.*, vol. 215, p. 109013, 2021, doi: https://doi.org/10.1016/j.compscitech.2021.109013.

[39] A. M. Elliott, O. S. Ivanova, C. B. Williams, and T. A. Campbell, "Inkjet Printing of Quantum Dots in Photopolymer for Use in Additive Manufacturing of Nanocomposites," *Adv. Eng. Mater.*, vol. 15, no. 10, pp. 903–907, Oct. 2013, doi: https://doi.org/10.1002/adem.201300020.

[40] P. F. Blazdell, J. R. G. Evans, M. J. Edirisinghe, P. Shaw, and M. J. Binstead, "The computer aided manufacture of ceramics using multilayer jet printing," *J. Mater. Sci. Lett.*, vol. 14, no. 22, pp. 1562–1565, 1995, doi: 10.1007/BF00455415.

[41] P. F. Blazdell and J. R. G. Evans, "Application of a continuous ink jet printer to solid freeforming of ceramics," *J. Mater. Process. Technol.*, vol. 99, no. 1, pp. 94–102, 2000, doi: https://doi.org/10.1016/S0924-0136(99)00392-1.

[42] P. Blazdell, "Solid free-forming of ceramics using a continuous jet printer," *J. Mater. Process. Technol.*, vol. 137, no. 1, pp. 49–54, 2003, doi: https://doi.org/10.1016/S0924-0136(02)01060-9.

[43] S. H. Ko, J. Chung, N. Hotz, K. H. Nam, and C. P. Grigoropoulos, "Metal nanoparticle direct inkjet printing for low-temperature 3D micro metal structure fabrication," *J. Micromechanics Microengineering*, vol. 20, no. 12, p. 125010, 2010, doi: 10.1088/0960-1317/20/12/125010.

[44] A. Bîrcă, O. Gherasim, V. Grumezescu, and A. M. Grumezescu, "Chapter 1 - Introduction in thermoplastic and thermosetting polymers," V. Grumezescu and A. M. B. T.-M. for B. E. Grumezescu, Eds. Elsevier, 2019, pp. 1–28.

[45] A. G. Demir and B. Previtali, "Additive manufacturing of cardiovascular CoCr stents by selective laser melting," *Mater. Des.*, vol. 119, pp. 338–350, 2017, doi: https://doi.org/10.1016/j.matdes.2017.01.091.

[46] N. M. Terry Wohlers, Robert Ian Campbell, Olaf Diegel, Joseph Kowen, Ray

Huff, "Wohlers Report 2021 | 3D Printing and Additive Manufacturing Global State of the Industry," *https://www.fastenernewsdesk.com/*, p. 375, 2021, Accessed: Nov. 14, 2023. [Online]. Available: https://www.fastenernewsdesk.com/28315/wohlers-report-2021-3d-printing-and-additive-manufacturing-global-state-of-the-industry/.

[47] D. Herzog, V. Seyda, E. Wycisk, and C. Emmelmann, "Additive manufacturing of metals," *Acta Mater.*, vol. 117, pp. 371–392, 2016, doi: https://doi.org/10.1016/j.actamat.2016.07.019.

[48] S. Santoni, S. G. Gugliandolo, M. Sponchioni, D. Moscatelli, and B. M. Colosimo, "3D bioprinting: current status and trends—a guide to the literature and industrial practice," *Bio-Design Manuf.*, vol. 5, no. 1, pp. 14–42, 2022, doi: 10.1007/s42242-021-00165-0.

[49] J. V Alemán *et al.*, "Definitions of terms relating to the structure and processing of sols, gels, networks, and inorganic-organic hybrid materials (IUPAC Recommendations 2007)," vol. 79, no. 10, pp. 1801–1829, 2007, doi: doi:10.1351/pac200779101801.

[50] G. Ratheesh, J. R. Venugopal, A. Chinappan, H. Ezhilarasu, A. Sadiq, and S. Ramakrishna, "3D Fabrication of Polymeric Scaffolds for Regenerative Therapy," *ACS Biomater. Sci. & Eng.*, vol. 3, no. 7, pp. 1175–1194, 2017, doi: 10.1021/acsbiomaterials.6b00370.

[51] A. Shafiee and A. Atala, "Tissue Engineering: Toward a New Era of Medicine," *Annu. Rev. Med.*, vol. 68, no. 1, pp. 29–40, Jan. 2017, doi: 10.1146/annurev-med-102715-092331.

[52] C. M. Magin, D. L. Alge, and K. S. Anseth, "Bio-inspired 3D microenvironments: a new dimension in tissue engineering," *Biomed. Mater.*, vol. 11, no. 2, p. 22001, 2016, doi: 10.1088/1748-6041/11/2/022001.

[53] A.-V. Do, B. Khorsand, S. Geary, and A. Salem, "3D Printing of Scaffolds for Tissue Regeneration Applications," *Adv. Healthc. Mater.*, vol. 4, Jun. 2015, doi: 10.1002/adhm.201500168.

[54] A. Caseiro, H. Almeida, and P. Bártolo, "Additive manufacturing techniques for scaffold-based cartilage tissue engineering: A review on various additive manufacturing technologies in generating scaffolds for cartilage tissue engineering," *Virtual Phys. Prototyp.*, vol. 8, pp. 175–186, Jan. 2013.

[55] F. P. W. Melchels, M. A. N. Domingos, T. J. Klein, J. Malda, P. J. Bartolo, and D. W. Hutmacher, "Additive manufacturing of tissues and organs," *Prog. Polym. Sci.*, vol. 37, no. 8, pp. 1079–1104, 2012, doi: https://doi.org/10.1016/j.progpolymsci.2011.11.007.

[56] B. Husár, M. Hatzenbichler, V. Mironov, R. Liska, J. Stampfl, and A. Ovsianikov,

"6 - Photopolymerization-based additive manufacturing for the development of 3D porous scaffolds," P. Dubruel and S. B. T.-B. for B. R. Van Vlierberghe, Eds. Woodhead Publishing, 2014, pp. 149–201.

[57] B. Husár and R. Liska, "ChemInform Abstract: Vinyl Carbonates, Vinyl Carbamates, and Related Monomers: Synthesis, Polymerization, and Application," *Chem. Soc. Rev.*, vol. 41, pp. 2395–2405, Nov. 2011, doi: 10.1039/c1cs15232g.

[58] R. A. GIORDANO, B. M. Wu, S. W. Borland, L. G. Cima, E. M. Sachs, and M. J. Cima, "Mechanical properties of dense polylactic acid structures fabricated by three dimensional printing," *J. Biomater. Sci. Polym. Ed.*, vol. 8, no. 1, pp. 63–75, Jan. 1997, doi: 10.1163/156856297X00588.

[59] J. Malda *et al.*, "25th anniversary article: Engineering hydrogels for biofabrication," *Adv. Mater.*, vol. 25, no. 36, pp. 5011–5028, 2013, doi: 10.1002/adma.201302042.

[60] M. A. S. R. Saadi *et al.*, "Direct Ink Writing: A 3D Printing Technology for Diverse Materials," *Adv. Mater.*, vol. 34, no. 28, 2022, doi: 10.1002/adma.202108855.

[61] L. del-Mazo-Barbara and M.-P. Ginebra, "Rheological characterisation of ceramic inks for 3D direct ink writing: A review," *J. Eur. Ceram. Soc.*, vol. 41, no. 16, pp. 18–33, 2021, doi: 10.1016/j.jeurceramsoc.2021.08.031.

[62] J. D. Boerckel *et al.*, "Effects of protein dose and delivery system on BMP-mediated bone regeneration," *Biomaterials*, vol. 32, no. 22, pp. 5241–5251, 2011, doi: 10.1016/j.biomaterials.2011.03.063.

[63] W. R. Gombotz and S. F. Wee, "Protein release from alginate matrices," *Adv. Drug Deliv. Rev.*, vol. 64, pp. 194–205, 2012, doi: https://doi.org/10.1016/j.addr.2012.09.007.

[64] Q. Wang, L. Wang, M. S. Detamore, and C. Berkland, "Biodegradable Colloidal Gels as Moldable Tissue Engineering Scaffolds," *Adv. Mater.*, vol. 20, no. 2, pp. 236–239, Jan. 2008, doi: https://doi.org/10.1002/adma.200702099.

[65] S. J. de Jong, W. N. E. van Dijk-Wolthuis, J. J. Kettenes-van den Bosch, P. J. W. Schuyl, and W. E. Hennink, "Monodisperse Enantiomeric Lactic Acid Oligomers: Preparation, Characterization, and Stereocomplex Formation," *Macromolecules*, vol. 31, no. 19, pp. 6397–6402, Sep. 1998, doi: 10.1021/ma980553i.

[66] I. Rashkov, N. Manolova, S. M. Li, J. L. Espartero, and M. Vert, "Synthesis, Characterization, and Hydrolytic Degradation of PLA/PEO/PLA Triblock Copolymers with Short Poly(l-lactic acid) Chains," *Macromolecules*, vol. 29, no. 1, pp. 50–56, Jan. 1996, doi: 10.1021/ma950530t.

[67] S. Buwalda, P. Dijkstra, L. Calucci, C. Forte, and J. Feijen, "Influence of Amide versus Ester Linkages on the Properties of Eight-Armed PEG-PLA Star Block

Copolymer Hydrogels," *Biomacromolecules*, vol. 11, pp. 224–232, Nov. 2009, doi: 10.1021/bm901080d.

[68] S. Chaterji, I. K. Kwon, and K. Park, "Smart polymeric gels: Redefining the limits of biomedical devices," *Prog. Polym. Sci.*, vol. 32, no. 8, pp. 1083–1122, 2007, doi: https://doi.org/10.1016/j.progpolymsci.2007.05.018.

[69] N. Peppas and W. Leobandung, "Stimuli-sensitive hydrogels: Ideal carriers for chronobiology and chronotherapy," *J. Biomater. Sci. Polym. Ed.*, vol. 15, pp. 125–144, Feb. 2004, doi: 10.1163/156856204322793539.

[70] A. C. H. Tsang, J. Zhang, K. N. Hui, K. S. Hui, and H. Huang, "Recent Development and Applications of Advanced Materials via Direct Ink Writing," *Adv. Mater. Technol.*, vol. 7, no. 7, 2022, doi: 10.1002/admt.202101358.

[71] M. Wehner *et al.*, "An integrated design and fabrication strategy for entirely soft, autonomous robots," *Nature*, vol. 536, no. 7617, pp. 451–455, 2016, doi: 10.1038/nature19100.

[72] D. Rus and M. T. Tolley, "Design, fabrication and control of soft robots," *Nature*, vol. 521, no. 7553, pp. 467–475, 2015, doi: 10.1038/nature14543.

[73] A. E. Jakus, E. B. Secor, A. L. Rutz, S. W. Jordan, M. C. Hersam, and R. N. Shah, "Three-Dimensional Printing of High-Content Graphene Scaffolds for Electronic and Biomedical Applications," *ACS Nano*, vol. 9, no. 4, pp. 4636–4648, Apr. 2015, doi: 10.1021/acsnano.5b01179.

[74] M. A. Skylar-Scott *et al.*, "Biomanufacturing of organ-specific tissues with high cellular density and embedded vascular channels," *Sci. Adv.*, vol. 5, no. 9, p. eaaw2459, Sep. 2023, doi: 10.1126/sciadv.aaw2459.

[75] S. Ghosh, S. T. Parker, X. Wang, D. L. Kaplan, and J. A. Lewis, "Direct-Write Assembly of Microperiodic Silk Fibroin Scaffolds for Tissue Engineering Applications," *Adv. Funct. Mater.*, vol. 18, no. 13, pp. 1883–1889, Jul. 2008, doi: https://doi.org/10.1002/adfm.200800040.

[76] B. Y. Ahn *et al.*, "Omnidirectional Printing of Flexible, Stretchable, and Spanning Silver Microelectrodes," *Science (80-.).*, vol. 323, no. 5921, pp. 1590–1593, Mar. 2009, doi: 10.1126/science.1168375.

[77] J. T. Muth *et al.*, "Embedded 3D printing of strain sensors within highly stretchable elastomers," *Adv. Mater.*, vol. 26, no. 36, pp. 6307–6312, 2014, doi: 10.1002/adma.201400334.

[78] K. Tian *et al.*, "3D Printing of Transparent and Conductive Heterogeneous Hydrogel–Elastomer Systems," *Adv. Mater.*, vol. 29, no. 10, p. 1604827, Mar. 2017, doi: https://doi.org/10.1002/adma.201604827.

[79] J. Raney, N. Nadkarni, C. Daraio, D. Kochmann, J. Lewis, and K. Bertoldi, "Stable

propagation of mechanical signals in soft media using stored elastic energy," *Proc. Natl. Acad. Sci.*, vol. 113, pp. 9722–9727, Aug. 2016, doi: 10.1073/pnas.1604838113.

[80] A. Sydney Gladman, E. A. Matsumoto, R. G. Nuzzo, L. Mahadevan, and J. A. Lewis, "Biomimetic 4D printing," *Nat. Mater.*, vol. 15, no. 4, pp. 413–418, 2016, doi: 10.1038/nmat4544.

[81] E. B. Duoss *et al.*, "Three-Dimensional Printing of Elastomeric, Cellular Architectures with Negative Stiffness," *Adv. Funct. Mater.*, vol. 24, no. 31, pp. 4905–4913, Aug. 2014, doi: https://doi.org/10.1002/adfm.201400451.

[82] S. Chen, G. Liu, H. Yadegari, H. Wang, and S. Qiao, "Three-dimensional MnO 2 ultrathin nanosheet aerogels for high-performance Li–O 2 batteries," *J. Mater. Chem. A*, vol. 3, pp. 2559–2563, Jan. 2015, doi: 10.1039/C5TA00004A.

[83] C. P. Lee, R. Karyappa, and M. Hashimoto, "3D printing of milk-based product," *RSC Adv.*, vol. 10, pp. 29821–29828, Aug. 2020, doi: 10.1039/D0RA05035K.

[84] Y. Zhang *et al.*, "Recent Progress of Direct Ink Writing of Electronic Components for Advanced Wearable Devices," *ACS Appl. Electron. Mater.*, vol. 1, no. 9, pp. 1718–1734, 2019, doi: 10.1021/acsaelm.9b00428.

[85] V. G. Rocha, E. Saiz, I. S. Tirichenko, and E. García-Tuñón, "Direct ink writing advances in multi-material structures for a sustainable future," *J. Mater. Chem. A*, vol. 8, no. 31, pp. 15646–15657, 2020, doi: 10.1039/d0ta04181e.

[86] Y. Yang, R. Boom, B. Irion, D.-J. van Heerden, P. Kuiper, and H. de Wit, "Recycling of composite materials," *Chem. Eng. Process. Process Intensif.*, vol. 51, pp. 53–68, 2012, doi: https://doi.org/10.1016/j.cep.2011.09.007.

[87] L. Giorgini, T. Benelli, G. Brancolini, and L. Mazzocchetti, "Recycling of carbon fiber reinforced composite waste to close their life cycle in a cradle-to-cradle approach," *Curr. Opin. Green Sustain. Chem.*, vol. 26, p. 100368, 2020, doi: https://doi.org/10.1016/j.cogsc.2020.100368.

[88] D. Ayre, "Technology advancing polymers and polymer composites towards sustainability: A review," *Curr. Opin. Green Sustain. Chem.*, vol. 13, pp. 108–112, 2018, doi: https://doi.org/10.1016/j.cogsc.2018.06.018.

[89] G. Oliveux, L. O. Dandy, and G. A. Leeke, "Current status of recycling of fibre reinforced polymers: Review of technologies, reuse and resulting properties," *Prog. Mater. Sci.*, vol. 72, pp. 61–99, 2015, doi: https://doi.org/10.1016/j.pmatsci.2015.01.004.

[90] P. T. Mativenga, A. A. M. Sultan, J. Agwa-Ejon, and C. Mbohwa, "Composites in a Circular Economy: A Study of United Kingdom and South Africa," *Procedia CIRP*, vol. 61, pp. 691–696, 2017, doi: https://doi.org/10.1016/j.procir.2016.11.270.

[91] M. Invernizzi, G. Natale, M. Levi, S. Turri, and G. Griffini, "UV-Assisted 3D Printing of Glass and Carbon Fiber-Reinforced Dual-Cure Polymer Composites," *Materials (Basel).*, vol. 9, p. 583, Jul. 2016, doi: 10.3390/ma9070583.

[92] A. Mantelli *et al.*, "UV-Assisted 3D Printing of Polymer Composites from Thermally and Mechanically Recycled Carbon Fibers," *Polymers (Basel).*, vol. 13, p. 726, Feb. 2021, doi: 10.3390/polym13050726.

[93] A. Mantelli, M. Levi, S. Turri, and R. Suriano, "Remanufacturing of end-of-life glass-fiber reinforced composites via UV-assisted 3D printing," *Rapid Prototyp. J.*, vol. ahead-of-p, Sep. 2019, doi: 10.1108/RPJ-01-2019-0011.

[94] D. M. Sánchez, M. de la Mata, F. J. Delgado, V. Casal, and S. I. Molina, "Development of carbon fiber acrylonitrile styrene acrylate composite for large format additive manufacturing," *Mater. Des.*, vol. 191, p. 108577, 2020, doi: https://doi.org/10.1016/j.matdes.2020.108577.

[95] M. G. Mohammed and R. Kramer, "All-Printed Flexible and Stretchable Electronics," *Adv. Mater.*, vol. 29, no. 19, p. 1604965, May 2017, doi: https://doi.org/10.1002/adma.201604965.

[96] J. W. Boley, E. L. White, G. T.-C. Chiu, and R. K. Kramer, "Direct Writing of Gallium-Indium Alloy for Stretchable Electronics," *Adv. Funct. Mater.*, vol. 24, no. 23, pp. 3501–3507, Jun. 2014, doi: https://doi.org/10.1002/adfm.201303220.

[97] S.-Z. Guo, K. Qiu, F. Meng, S. H. Park, and M. C. McAlpine, "3D Printed Stretchable Tactile Sensors," *Adv. Mater.*, vol. 29, no. 27, p. 1701218, Jul. 2017, doi: https://doi.org/10.1002/adma.201701218.

[98] Z. Wang, X. Guan, H. Huang, H. Wang, W. Lin, and Z. Peng, "Full 3D Printing of Stretchable Piezoresistive Sensor with Hierarchical Porosity and Multimodulus Architecture," *Adv. Funct. Mater.*, vol. 29, no. 11, p. 1807569, Mar. 2019, doi: https://doi.org/10.1002/adfm.201807569.

[99] Y.-G. Park, H. S. An, J.-Y. Kim, and J.-U. Park, "High-resolution, reconfigurable printing of liquid metals with three-dimensional structures," *Sci. Adv.*, vol. 5, no. 6, p. eaaw2844, Sep. 2023, doi: 10.1126/sciadv.aaw2844.

[100] M. Skylar-Scott, S. Gunasekaran, and J. Lewis, "Laser-assisted direct ink writing of planar and 3D metal architectures," *Proc. Natl. Acad. Sci.*, vol. 113, p. 201525131, May 2016, doi: 10.1073/pnas.1525131113.

[101] J. J. Adams *et al.*, "Conformal Printing of Electrically Small Antennas on Three-Dimensional Surfaces," *Adv. Mater.*, vol. 23, no. 11, pp. 1335–1340, Mar. 2011, doi: https://doi.org/10.1002/adma.201003734.

[102] N. Zhou, C. Liu, J. A. Lewis, and D. Ham, "Gigahertz Electromagnetic Structures via Direct Ink Writing for Radio-Frequency Oscillator and Transmitter Applications," *Adv. Mater.*, vol. 29, no. 15, p. 1605198, Apr. 2017, doi:

https://doi.org/10.1002/adma.201605198.

[103] B. Chen *et al.*, "Three-dimensional ultraflexible triboelectric nanogenerator made by 3D printing," *Nano Energy*, vol. 45, pp. 380–389, 2018, doi: https://doi.org/10.1016/j.nanoen.2017.12.049.

[104] R. Wang *et al.*, "Direct-writing of vanadium dioxide/polydimethylsiloxane three-dimensional photonic crystals with thermally tunable terahertz properties," *J. Mater. Chem. C*, vol. 7, May 2019, doi: 10.1039/C8TC05759A.

[105] P. Jiang *et al.*, "Direct ink writing of high-strength and swelling-resistant biocompatible physical-crosslinking hydrogels," *Biomater. Sci.*, vol. 7, Feb. 2019, doi: 10.1039/C9BM00081J.

[106] D. Roach *et al.*, "Long Liquid Crystal Elastomer Fibers with Large Reversible Actuation Strains for Smart Textiles and Artificial Muscles," *ACS Appl. Mater. Interfaces*, vol. 11, May 2019, doi: 10.1021/acsami.9b04401.

[107] W. Wu, A. DeConinck, and J. A. Lewis, "Omnidirectional Printing of 3D Microvascular Networks," *Adv. Mater.*, vol. 23, no. 24, pp. H178–H183, Jun. 2011, doi: https://doi.org/10.1002/adma.201004625.

[108] Q. Fu, E. Saiz, and A. P. Tomsia, "Direct ink writing of highly porous and strong glass scaffolds for load-bearing bone defects repair and regeneration," *Acta Biomater.*, vol. 7, no. 10, pp. 3547–3554, 2011, doi: https://doi.org/10.1016/j.actbio.2011.06.030.

[109] A. M. Deliormanlı and M. N. Rahaman, "Direct-write assembly of silicate and borate bioactive glass scaffolds for bone repair," *J. Eur. Ceram. Soc.*, vol. 32, no. 14, pp. 3637–3646, 2012, doi: https://doi.org/10.1016/j.jeurceramsoc.2012.05.005.

[110] W. Kim, M. Kim, and G. H. Kim, "3D-Printed Biomimetic Scaffold Simulating Microfibril Muscle Structure," *Adv. Funct. Mater.*, vol. 28, no. 26, p. 1800405, Jun. 2018, doi: https://doi.org/10.1002/adfm.201800405.

[111] M. J. Rodriguez, J. Brown, J. Giordano, S. J. Lin, F. G. Omenetto, and D. L. Kaplan, "Silk based bioinks for soft tissue reconstruction using 3-dimensional (3D) printing with in vitro and in vivo assessments," *Biomaterials*, vol. 117, pp. 105–115, 2017, doi: https://doi.org/10.1016/j.biomaterials.2016.11.046.

[112] H. Wei, Q. Zhang, Y. Yao, L. Liu, Y. Liu, and J. Leng, "Direct-Write Fabrication of 4D Active Shape-Changing Structures Based on a Shape Memory Polymer and Its Nanocomposite," *ACS Appl. Mater. Interfaces*, vol. 9, no. 1, pp. 876–883, Jan. 2017, doi: 10.1021/acsami.6b12824.

[113] Y. Chen *et al.*, "A biocompatible thermoset polymer binder for Direct Ink Writing of porous titanium scaffolds for bone tissue engineering," *Mater. Sci. Eng. C*, vol. 95, pp. 160–165, 2019, doi: https://doi.org/10.1016/j.msec.2018.10.033.

[114] N. Kleger, M. Cihova, K. Masania, A. R. Studart, and J. F. Löffler, "3D Printing of Salt as a Template for Magnesium with Structured Porosity," *Adv. Mater.*, vol. 31, no. 37, p. 1903783, Sep. 2019, doi: https://doi.org/10.1002/adma.201903783.

[115] Y. Lakhdar, C. Tuck, J. Binner, A. Terry, and R. Goodridge, "Additive manufacturing of advanced ceramic materials," *Prog. Mater. Sci.*, vol. 116, p. 100736, 2021, doi: https://doi.org/10.1016/j.pmatsci.2020.100736.

[116] Q. Chang *et al.*, "Hydrogels from natural egg white with extraordinary stretchability, direct-writing 3D printability and self-healing for fabrication of electronic sensor and actuator," *J. Mater. Chem. A*, vol. 7, Sep. 2019, doi: 10.1039/C9TA06233E.

[117] A. Saha *et al.*, "Additive Manufacturing of Catalytically Active Living Materials," *ACS Appl. Mater. Interfaces*, vol. 10, no. 16, pp. 13373–13380, Apr. 2018, doi: 10.1021/acsami.8b02719.

[118] M. Schaffner, P. A. Rühs, F. Coulter, S. Kilcher, and A. R. Studart, "3D printing of bacteria into functional complex materials," *Sci. Adv.*, vol. 3, no. 12, p. eaao6804, Sep. 2023, doi: 10.1126/sciadv.aao6804.

[119] J. R. Centre and I. for E. and Sustainability, *General guide for Life Cycle Assessment – Provisions and action steps*. Publications Office, 2010.

[120] L. Jacquemin, P.-Y. Pontalier, and C. Sablayrolles, "Life cycle assessment (LCA) applied to the process industry: a review," *Int. J. Life Cycle Assess.*, vol. 17, no. 8, pp. 1028–1041, 2012, doi: 10.1007/s11367-012-0432-9.

[121] M. A. J. Huijbregts *et al.*, "ReCiPe2016: a harmonised life cycle impact assessment method at midpoint and endpoint level," *Int. J. Life Cycle Assess.*, vol. 22, no. 2, pp. 138–147, 2017, doi: 10.1007/s11367-016-1246-y.

[122] J. W. Bennett, "Pearce, D. W., and R. K. Turner. Economics of Natural Resources and the Environment. Baltimore MD: Johns Hopkins University Press, 1990, 378 pp., $@@-@@42.50, $@@-@@19.50 paper," *Am. J. Agric. Econ.*, vol. 73, no. 1, pp. 227–228, Feb. 1991, doi: https://doi.org/10.2307/1242904.

[123] J. Kirchherr, D. Reike, and M. Hekkert, "Conceptualizing the circular economy: An analysis of 114 definitions," *Resour. Conserv. Recycl.*, vol. 127, pp. 221–232, 2017, doi: https://doi.org/10.1016/j.resconrec.2017.09.005.

[124] A. Zamagni, H.-L. Pesonen, and T. Swarr, "From LCA to Life Cycle Sustainability Assessment: concept, practice and future directions," *Int. J. Life Cycle Assess.*, vol. 18, no. 9, pp. 1637–1641, 2013, doi: 10.1007/s11367-013-0648-3.

[125] C. Peña *et al.*, "Using life cycle assessment to achieve a circular economy," *Int. J. Life Cycle Assess.*, vol. 26, no. 2, pp. 215–220, 2021, doi: 10.1007/s11367-020-01856-z.

[126] C. Spreafico, "An analysis of design strategies for circular economy through life cycle assessment," *Environ. Monit. Assess.*, vol. 194, no. 3, p. 180, 2022, doi: 10.1007/s10661-022-09803-1.

[127] L. Muthukrishnan, "Nanotechnology for cleaner leather production: a review," *Environ. Chem. Lett.*, vol. 19, no. 3, pp. 2527–2549, 2021, doi: 10.1007/s10311-020-01172-w.

[128] H. A. Innis, "The Davis Family and the Leather Industry, 1834-1934, by Bruce Pettit Davis and Carroll Langstaff Davis (Toronto, Ryerson, 1934, pp. 145).," *Can. J. Econ. Polit. Sci. Can. Econ. Sci. Polit.*, vol. 3, no. 1, pp. 143–144, 1937, doi: DOI: 10.2307/136838.

[129] "Trade statistics | ITC." https://intracen.org/resources/data-and-analysis/trade-statistics (accessed Nov. 14, 2023).

[130] "Leather Goods Market Size & Growth | Global Report [2030]." https://www.fortunebusinessinsights.com/leather-goods-market-104405 (accessed Nov. 14, 2023).

[131] J. Hu, Z. Xiao, R. Zhou, W. Deng, M. Wang, and S. Ma, "Ecological utilization of leather tannery waste with circular economy model," *J. Clean. Prod.*, vol. 19, no. 2, pp. 221–228, 2011, doi: https://doi.org/10.1016/j.jclepro.2010.09.018.

[132] K. Chojnacka *et al.*, "Progress in sustainable technologies of leather wastes valorization as solutions for the circular economy," *J. Clean. Prod.*, vol. 313, p. 127902, 2021, doi: https://doi.org/10.1016/j.jclepro.2021.127902.

[133] W. Yu, *The mechanical properties of leather in relation to softness*. University of Leicester (United Kingdom), 1999.

[134] K. J. Bieńkiewicz, *Physical Chemistry of Leather Making*. Krieger Publishing Company, 1983.

[135] F. O'Flaherty, W. T. Roddy, R. M. Lollar, and A. C. Society, *The Chemistry and Technology of Leather*, no. v. 3. R.E. Krieger Publishing Company, 1978.

[136] R. Mayne and R. E. Burgeson, *Structure and function of collagen types*. United States: Academic Press Inc.,Orlando, FL, 1987.

[137] E. Heidemann, *Fundamentals of Leather Manufacture*. Eduard Roether KG, 1993.

[138] A. J. Hodge and F. O. Schmitt, "THE CHARGE PROFILE OF THE TROPOCOLLAGEN MACROMOLECULE AND THE PACKING ARRANGEMENT IN NATIVE-TYPE COLLAGEN FIBRILS*," *Proc. Natl. Acad. Sci.*, vol. 46, no. 2, pp. 186–197, Feb. 1960, doi: 10.1073/pnas.46.2.186.

[139] V. Beghetto, A. Zancanaro, A. Scrivanti, U. Matteoli, and G. D. Pozza, "The Leather Industry: A Chemistry Insight Part I: an Overview of the Industrial Process," 2013, [Online]. Available:

https://api.semanticscholar.org/CorpusID:56351164.

[140] J. H. BOWES and R. H. KENTEN, "The swelling of collagen in alkaline solutions; swelling in solutions of univalent bases," *Biochem. J.*, vol. 46, no. 5, pp. 524–529, 1950, doi: 10.1042/bj0460524.

[141] A. D. Covington and W. R. Wise, *Tanning Chemistry: The Science of Leather*. The Royal Society of Chemistry, 2019.

[142] J. Bella, B. Brodsky, and H. M. Berman, "Hydration structure of a collagen peptide," *Structure*, vol. 3, no. 9, pp. 893–906, 1995, doi: https://doi.org/10.1016/S0969-2126(01)00224-6.

[143] A. G. Ward, "The mechanical properties of leather," *Rheol. Acta*, vol. 13, no. 1, pp. 103–112, 1974, doi: 10.1007/BF01526892.

[144] P. Fratzl, K. Misof, I. Zizak, G. Rapp, H. Amenitsch, and S. Bernstorff, "Fibrillar Structure and Mechanical Properties of Collagen," *J. Struct. Biol.*, vol. 122, no. 1, pp. 119–122, 1998, doi: https://doi.org/10.1006/jsbi.1998.3966.

[145] Y. . Osin, L. Y. Makhotkina, L. N. Abutalipova, and I. S. Abdullin, "SEM and X-ray analysis of surface microstructure of a natural leather processed in a low temperature plasmafn2fn2Paper presented at the 10th International School on Vacuum, Electron and Ion Technologies (VEIT97), 22–27 September 1997, Varna, Bulgaria.," *Vacuum*, vol. 51, no. 2, pp. 221–225, 1998, doi: https://doi.org/10.1016/S0042-207X(98)00163-8.

[146] M. Tuckermann, M. Mertig, and W. Pompe, "In situ observation of moisture-induced swelling of leather in an environmental scanning electron microscope," *Rev. Sci. Instrum.*, vol. 72, no. 2, pp. 1449–1452, Feb. 2001, doi: 10.1063/1.1334625.

[147] Z. Li, D. Paudecerf, and J. Yang, "Mechanical behaviour of natural cow leather in tension," *Acta Mech. Solida Sin.*, vol. 22, no. 1, pp. 37–44, 2009, doi: https://doi.org/10.1016/S0894-9166(09)60088-4.

[148] C.-K. Liu, N. P. Latona, G. L. DiMaio, and P. H. Cooke, "Viscoelasticity studies for a fibrous collagen material: chrome-free leather," *J. Mater. Sci.*, vol. 42, no. 20, pp. 8509–8516, 2007, doi: 10.1007/s10853-007-1744-1.

[149] C.-K. Liu, M. D. McClintick, A. STANLEY, and S. SCHNEIDER, "An energy approach to the characterization of the fracture resistance of leather," *J. Am. Leather Chem. Assoc.*, vol. 92, no. 5, pp. 103–118, 1997.

[150] E. K. Roh, K. W. Oh, and S. H. Kim, "Classification of synthetic polyurethane leather by mechanical properties according to consumers' preference for fashion items," *Fibers Polym.*, vol. 14, no. 10, pp. 1731–1738, 2013, doi: 10.1007/s12221-013-1731-x.

[151] "Szycher's Handbook of Polyurethanes By Michael Szycher (CardioTech

International, Inc.). CRC Press: Boca Raton, FL. 1999. xviii + 673 pp. $129.95. ISBN 0-8493-0602-7.," *J. Am. Chem. Soc.*, vol. 122, no. 16, p. 3983, Apr. 2000, doi: 10.1021/ja004704k.

[152] I. Yilgör, E. Yilgör, and G. L. Wilkes, "Critical parameters in designing segmented polyurethanes and their effect on morphology and properties: A comprehensive review," *Polymer (Guildf).*, vol. 58, pp. A1–A36, 2015, doi: https://doi.org/10.1016/j.polymer.2014.12.014.

[153] M. Sáenz-Pérez, E. Lizundia, J. M. Laza, J. García-Barrasa, J. L. Vilas, and L. M. León, "Methylene diphenyl diisocyanate (MDI) and toluene diisocyanate (TDI) based polyurethanes: thermal, shape-memory and mechanical behavior," *RSC Adv.*, vol. 6, no. 73, pp. 69094–69102, 2016, doi: 10.1039/C6RA13492K.

[154] D.-K. Lee and H.-B. Tsai, "Properties of segmented polyurethanes derived from different diisocyanates," *J. Appl. Polym. Sci.*, vol. 75, no. 1, pp. 167–174, Jan. 2000, doi: https://doi.org/10.1002/(SICI)1097-4628(20000103)75:1<167::AID-APP19>3.0.CO;2-N.

[155] K. Joseph and N. Nithya, "Material flows in the life cycle of leather," *J. Clean. Prod.*, vol. 17, no. 7, pp. 676–682, 2009, doi: https://doi.org/10.1016/j.jclepro.2008.11.018.

[156] D. Navarro, J. Wu, W. Lin, P. Fullana-i-Palmer, and R. Puig, "Life cycle assessment and leather production," *J. Leather Sci. Eng.*, vol. 2, no. 1, p. 26, 2020, doi: 10.1186/s42825-020-00035-y.

[157] K. Fela, K. Wieczorek-Ciurowa, M. Konopka, and Z. Woźny, "Present and prospective leather industry waste disposal," *Polish J. Chem. Technol.*, vol. 13, no. 3, pp. 53–55, 2011, doi: doi:10.2478/v10026-011-0037-2.

[158] D. Masilamani, B. Madhan, G. Shanmugam, S. Palanivel, and B. Narayan, "Extraction of collagen from raw trimming wastes of tannery: a waste to wealth approach," *J. Clean. Prod.*, vol. 113, pp. 338–344, 2016, doi: https://doi.org/10.1016/j.jclepro.2015.11.087.

[159] L. Šánek, J. Pecha, K. Kolomazník, and M. Bařinová, "Biodiesel production from tannery fleshings: Feedstock pretreatment and process modeling," *Fuel*, vol. 148, pp. 16–24, 2015, doi: https://doi.org/10.1016/j.fuel.2015.01.084.

[160] A. Cabrera-Codony *et al.*, "From biocollagenic waste to efficient biogas purification: Applying circular economy in the leather industry," *Environ. Technol. Innov.*, vol. 21, p. 101229, 2021, doi: https://doi.org/10.1016/j.eti.2020.101229.

[161] S. Selvaraj, S. Ramalingam, S. Parida, J. R. Rao, and N. F. Nishter, "Chromium containing leather trimmings valorization: Sustainable sound absorber from collagen hydrolysate intercalated electrospun nanofibers," *J. Hazard. Mater.*, vol.

405, p. 124231, 2021, doi: https://doi.org/10.1016/j.jhazmat.2020.124231.

[162] M. E. Bautista, L. Pérez, M. T. García, S. Cuadros, and A. Marsal, "Valorization of tannery wastes: Lipoamino acid surfactant mixtures from the protein fraction of process wastewater," *Chem. Eng. J.*, vol. 262, pp. 399–408, 2015, doi: https://doi.org/10.1016/j.cej.2014.10.004.

[163] S. Majee, G. Halder, and T. Mandal, "Formulating nitrogen-phosphorous-potassium enriched organic manure from solid waste: A novel approach of waste valorization," *Process Saf. Environ. Prot.*, vol. 132, pp. 160–168, 2019, doi: https://doi.org/10.1016/j.psep.2019.10.013.

[164] S. Famielec, "Chromium Concentrate Recovery from Solid Tannery Waste in a Thermal Process," *Materials*, vol. 13, no. 7. 2020, doi: 10.3390/ma13071533.

[165] J. Sánchez, R. Cue-Sampedro, L. Peña-Parás, and E. Palacios-Aguilar, "Functionalization of Carbon Nanotubes and Polymer Compatibility Studies," *J. Mater. Sci. Res.*, Oct. 2014, doi: 10.5539/jmsr.v3n1p1.

[166] C. Cionti, G. Vavassori, E. Pargoletti, D. Meroni, and G. Cappelletti, "One-step, highly stable Pickering emulsions stabilized by ZnO: tuning emulsion stability by in situ functionalization," *J. Colloid Interface Sci.*, vol. 628, pp. 82–89, 2022, doi: https://doi.org/10.1016/j.jcis.2022.07.129.

[167] E. A. Kamoun, A. M. Omer, M. M. Abu-Serie, S. N. Khattab, H. M. Ahmed, and A. A. Elbardan, "Photopolymerized PVA-g-GMA Hydrogels for Biomedical Applications: Factors Affecting Hydrogel Formation and Bioevaluation Tests," *Arab. J. Sci. Eng.*, vol. 43, no. 7, pp. 3565–3575, 2018, doi: 10.1007/s13369-017-3054-5.

[168] I. Korbag and S. Mohamed, "Studies on the formation of intermolecular interactions and structural characterization of polyvinyl alcohol/lignin film," *Int. J. Environ. Stud.*, pp. 1–10, Feb. 2016, doi: 10.1080/00207233.2016.1143700.

[169] A. Schwab, R. Levato, M. D'Este, S. Piluso, D. Eglin, and J. Malda, "Printability and Shape Fidelity of Bioinks in 3D Bioprinting," *Chem. Rev.*, vol. 120, no. 19, pp. 11028–11055, 2020, doi: 10.1021/acs.chemrev.0c00084.

[170] "D2765 Standard Test Methods for Determination of Gel Content and Swell Ratio of Crosslinked Ethylene Plastics." https://www.astm.org/d2765-16.html (accessed Nov. 15, 2023).

[171] "ISO 11357-1:2023(en), Plastics — Differential scanning calorimetry (DSC) — Part 1: General principles." https://www.iso.org/obp/ui/#iso:std:iso:11357:-1:ed-4:v1:en (accessed Nov. 15, 2023).

[172] "D638 Standard Test Method for Tensile Properties of Plastics." https://www.astm.org/d0638-14.html (accessed Nov. 18, 2023).

[173] "D3039/D3039M Standard Test Method for Tensile Properties of Polymer Matrix Composite Materials." https://www.astm.org/d3039_d3039m-08.html (accessed Nov. 15, 2023).

[174] M. Shou and T. Domenech, "Integrating LCA and blockchain technology to promote circular fashion – A case study of leather handbags," *J. Clean. Prod.*, vol. 373, p. 133557, 2022, doi: https://doi.org/10.1016/j.jclepro.2022.133557.

[175] R. Rajan, E. Rainosalo, M. Lebedevaite, J. Ostrauskaite, and V. Talacka, "Life Cycle Assessment, Optical 3D printing of dental models using acrylic resin based on soybean oils," 2022.

[176] Y. Dong, M. Hossain, L. Hongyang, and P. Liu, "Developing Conversion Factors of LCIA Methods for Comparison of LCA Results in the Construction Sector," *Sustainability*, vol. 13, p. 9016, Aug. 2021, doi: 10.3390/su13169016.

A Appendix A

Next photos represent the printability tests of SRS5 (above) and SRS10 (below).

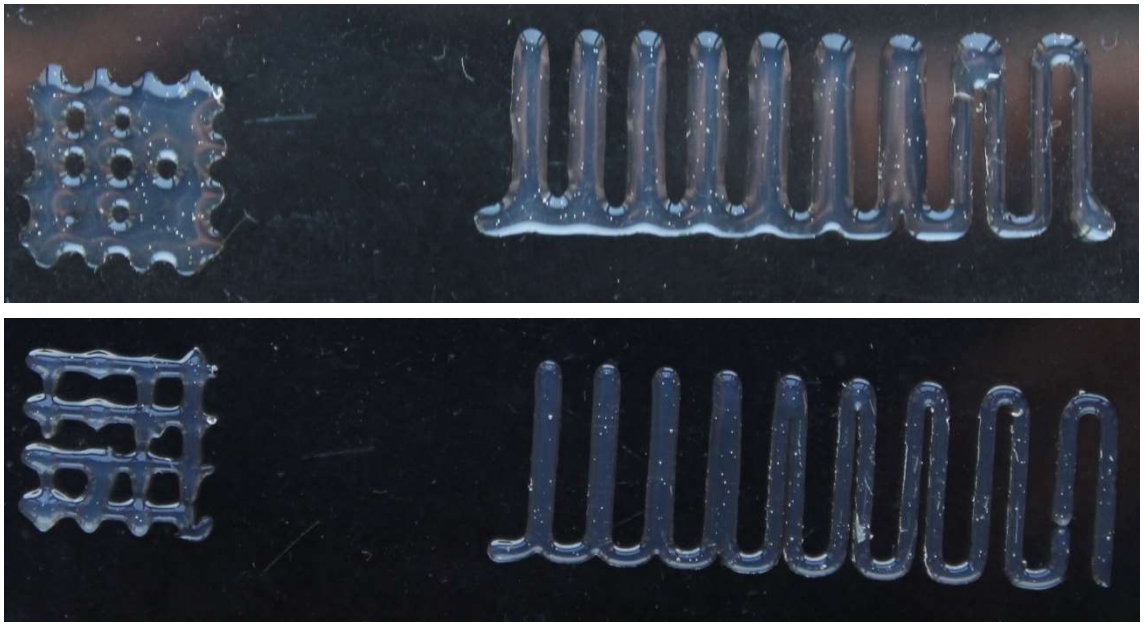

In the following figure SRC10 (left), SRC15 (middle), and SRC20 (right) cast are shown.

Printed PVAC20 (left), PVAC25 (middle), and PVAC30 (right) are illustrated in the following image.

List of Figures

List if Tables